Title

Untangling Tau Aggregation: Extensional Fluid Flow in Neurobiological Applications

ISBN

9798291564653

Author

Hollister, John C.P.

Publication Date

2025-08-26

Peer reviewed|Thesis/dissertation

UNIVERSITY OF CALIFORNIA

Los Angeles

Untangling Tau Aggregation: Extensional Fluid Flow in Neurobiological Applications

A dissertation submitted in partial satisfaction of the requirements for the degree of Doctor of Philosophy in Mechanical Engineering

John C.P. Hollister

2025

ABSTRACT OF THE DISSERTATION

Untangling Tau Aggregation: Extensional Fluid Flow in Neurobiological Applications

By

John C.P. Hollister

Doctor of Philosophy in Mechanical Engineering

University of California, Los Angeles, 2025

Professor Hossein Pirouz Kavehpour, Chair

Neurodegenerative diseases are a class of disease affecting millions worldwide and are often linked to the abnormal folding and aggregation of proteins (proteinopathies). One protein whose abnormal aggregation is of particular interest is tau, due to its occurrence in brains suffering from Chronic Traumatic Encephalopathy (CTE), a disease closely linked to traumatic brain injury. While tau aggregation is the subject of much biomedical research, that this phenomenon is so closely associated with a mechanical head injury highlights a significant gap in the current knowledge. In this dissertation, work done to narrow this gap is presented. Using extensional fluid flow, novel research is presented here to characterize biological fluid properties and induce aggregation of biologically and pathologically relevant proteins. Additionally, a non-dimensional

framework is presented in which future research can be conducted to develop tools to analyze and predict the aggregation of different protein species.

This dissertation is organized into two parts. In the first, rheological analysis is performed to characterize the mechanical properties of biological fluids. Demonstrating a recently developed micro-extensional rheology technique, the properties of surgically extracted vitreous humor are characterized, showing that ultrasonic surgical tools are capable of effectively liquefying the tissue, reducing the risk of complications during surgery and improving patient safety. Then, using a state-of-the-art shear rheometer, the non-Newtonian behavior of cerebrospinal fluid (CSF) is characterized, showing that injury and disease can have a significant impact on the shear-thinning flow properties of CSF.

In the second part, effort to induce protein aggregation using a custom built reciprocal extensional flow device is presented. Using this device, a controllable extensional flow field is generated, and aggregation of bovine serum albumin (BSA) protein solutions is achieved, showing characteristics pathological protein aggregation. With these results, non-dimensional analysis is presented, suggesting a new framework that could be used to analyze and predict protein aggregation. Finally, experiments in which two tau protein isoforms are treated using the reciprocal extensor are presented, resulting in robust and pathologically relevant aggregation of dGAE truncated tau as well as phosphorylated sf-GFP tau.

The dissertation of John C.P. Hollister is approved.

Mayumi L. Prins

Christopher C. Giza

Jeffrey D. Eldredge

Yen-Chih Lin

Hossein Pirouz Kavehpour, Committee Chair

University of California, Los Angeles

2025

To my parents, my wife, and my son.

Table of Contents

List of Figures

List of Tables

Acknowledgements

None of the following would have been possible had it not been for the incalculable help, encouragement, and support of my family, friends, mentors, and colleagues. I would like to thank everyone who has supported me through these past five years. From transitioning back to life as a student, to a global pandemic, to steadily bringing this work to completion, there are too many of you to name individually. For now, suffice it to say that if you are reading this, I am sincerely grateful to you for your support and all you've done for me.

I am especially indebted to Professor H. Pirouz Kavehpour, my advisor and mentor. I will be forever grateful that he saw something in my application (maybe my Bostonian roots) that compelled him to give me this opportunity. His encouragement and confidence in both me and my work was a much-needed lifeline when I was neck-deep in self-doubt. Under his guidance, I discovered my own love for teaching, a gift that will continue to shape my career and life. And of course, it's always nice to have someone around to chat about chowder and the Pats with.

I would like to thank Dr. Mayumi Prins and Dr. Christopher Giza for serving on my committee and the entire Brain Injury Research Center for offering invaluable insights into the clinical aspects of this research. I am especially grateful to Dr. Prins for her support through summer sessions, and to Dr. Giza for his effort in connecting me with fascinating researchers through the BrainSPORT group. I also thank my other committee members, Dr. Neil Lin and Dr. Jeff Eldredge for sharing their expertise and supporting me by serving on my committee. I am particularly thankful to Dr. Eldredge for his mentorship, research advice, and for the professional referrals and references he has provided over the years.

To my lab mates, Peiwen Yan, Parnian Hemmati, and Edo Leone, I thank you all for being inspiring researchers and great friends. I will always cherish the time we spent together in lab, from intense scientific discussions to supporting one another through life's changes. Entering this project with no background in neuroscience or neuroanatomy, I especially thank Parnian, my closest collaborator, for her generosity in brainstorming and exchange of ideas. Having a partner in this new research made it even more interesting and fun. I am proud to call each of you a colleague and friend, and I wish you the very best in your careers!

I owe the deepest gratitude to my family, who have encouraged and inspired me throughout my life. I especially want to thank my parents, Sheila and Gerry, from whom I inherited a love for learning, curiosity, and grit that I credit for bringing me here. I love you both, and there are not words enough to express my thanks for all you've done for me.

Finally, my greatest thanks go to my wife, Ariella. Her constant, persistent, and tenacious belief in me buoyed me at my lowest and propelled me forward at my highest. It is no exaggeration to say that without her love and support, I would not be writing this. Thank you for being on my team, for challenging me when I faltered, and for your flexibility and patience in allowing me to focus on this dissertation, even at 28+ weeks! As this chapter ends, I thank you for everything, my love. I can't wait for this next chapter in our lives to begin!

VITA

Education

Master of Science in Mechanical Engineering

University of California Los Angeles (June 2022)

Bachelor of Science in Mechanical Engineering

University of Massachusetts Amherst (June 2014)

Professional Experience

Teaching Fellow, Graduate Student Researcher

UCLA Complex Fluids and Interfacial Physics Laboratory (September 2020-Present)

Mechanical Engineer

Cepheid, Sunnyvale CA (August 2018-August 2020)

Engineer I/II

Terumo Cardiovascular Group, Ashland MA (March 2015-August 2018)

Test Engineer

Brookfield Engineering Laboratories, Middleborough MA (June 2014-February 2015)

Peer Reviewed Publications

Hollister, J.C.P., Wang, A.C., Kim, W., Giza, C.C., Prins, M.L., Kavehpour, H.P. Shear thinning behavior of cerebrospinal fluid with elevated protein or cellular concentration. *Frontiers in Physics* 11. (2023).

Hollister, J.C.P., Rodriguez, M., Hosseini, H., Papour, A., Hubschman, J., Kavehpour, H.P. Ultrasonic Vitrectomy Performance Assessment Using Micro-Extensional Rheology.

Translational Vision Science & Technology 12, 24. (2023).

Jafari, S., **Hollister, J.**, Kavehpour, P. & Demer, J. L. Shear viscoelastic properties of human orbital fat. *Journal of Biomechanics* 177, 112416 (2024).

Zhao, X., Zhou, Y., Li, A., Xu, J., Karjagi, S., Hahm, E., Rulloda, L., Li, J., **Hollister, J.**, Kavehpour, P., Chen, J. A Self-Filtering Ultrasensitive Liquid Acoustic Sensor for Voice Recognition. *Nature Electronics* (2024).

Zhao, X., Chang, A., Li, J., **Hollister, J.**, Che, Z., Wan, X., Yin, J., Wang, S., Lee, S., Kavehpour, P., Chen, J.. Air-Permeable Textile Bioelectronics for Wearable Energy Harvesting and Active Sensing. *Advanced Materials Technologies* 8, 2201703 (2023).

Conference Presentations

APS Division of Fluid Dynamics, 2023. "Cerebrospinal Fluid Facilitation of Cerebral Blood Flow: A Windkessel Analysis of Intracranial Hypertension." Oral presentation delivered at the APS DFD Meeting, Washington, DC.

Western Neurotrauma Symposium, 2022. **"**Analysis of Cerebrospinal Fluid Rheology using Shear and Extensional Techniques." Oral presentation delivered at the Western Neurotrauma Symposium, UCLA, Los Angeles, CA.

SoCal Fluids XV, 2022. "Hypersonic Technology Vitreous-Cutting Mechanism of Action Validation using Micro-Extensional Rheology." Oral presentation delivered at the SoCal Fluids meeting, UCLA, Los Angeles, CA.

APS Division of Fluid Dynamics, 2021. "Microextensional Rheology for Small Volume or Expensive Biological Sample Analysis." Oral presentation delivered at the APS DFD Meeting, Phoenix, AZ, 2021.

Chapter 1 : Introduction and Motivation

1.1 Introduction

Neurodegenerative diseases are a class of disease affecting millions worldwide where the cells of the central nervous system die or lose their primary function. Several neurodegenerative diseases are linked to the abnormal folding and aggregation of proteins (proteinopathies). These phenomena can occur inside and outside of brain cells and lead to cell malfunction and eventual cell death in some cases. Many neurodegenerative diseases are diagnosed or confirmed by the discovery of these abnormal aggregation plaques in different parts of the brain. These include Alzheimer's, Parkinson's, Huntington's, Chronic Traumatic Encephalopathy (CTE), as well as prion diseases such as Creutzfeldt-Jakob disease or Bovine Spongiform Encephalopathy (also known as Mad Cow disease)[1]. Despite this wide impact, however, the mechanisms that cause this aggregation are still not well understood.

One protein whose abnormal misfolding and aggregation has been attributed to many diseases is Tau. Tau is a protein that helps stabilize structural microtubules in neurons. However, tau detaching from microtubules and abnormally aggregating both intra- and extracellularly is linked to several neurodegenerative diseases[2] (Figure 1-1). To date, there are at least 26 distinct tauopathies identified, differentiated by the tau isoform involved and the location within the brain that is affected[3]. These tauopathies include Alzheimer's, Pick's Disease, and CTE among many others[4]. The enhanced understanding of tauopathy, therefore, could have a potentially enormous impact on the prediction, diagnosis, and treatment of these diseases.

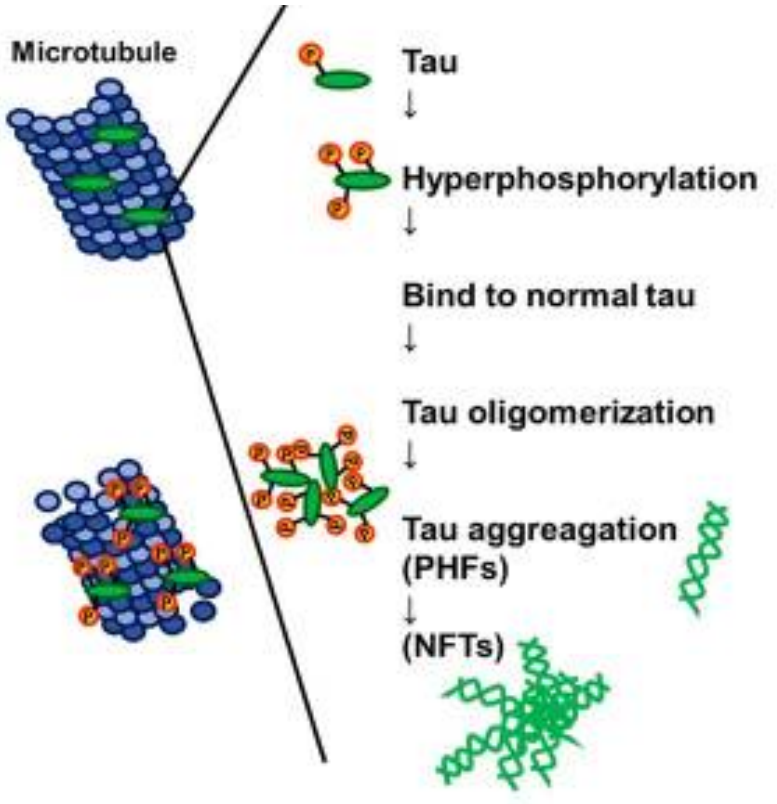

Figure 1-1: Progression of tau aggregation. Tau becomes hyperphosphorylated, loses binding affinity to microtubules, and aggregates into neurofibrillary tangles (NFTs), compromising microtubule stability[5].

CTE is one tauopathy that has gained attention in recent years due to its close link to traumatic brain injury (TBI), repeated TBI (rTBI), and sports related concussions (SRC)[5–8]. In fact, 99% of professional American Football players in one study exhibited tau aggregation symptomatic of CTE[9]. It is becoming abundantly clear that there is a strong correlation between head injury and neurodegenerative diseases like CTE[10]. That these mechanical processes, such as an impact to the head, can eventually lead to a physiological response such as tau aggregation highlights a significant gap in the understanding of these proteinopathies – that a mechanical approach to the characterization of these protein aggregations is necessary to fully understand the initiation and progression of these diseases (Figure 1-2).

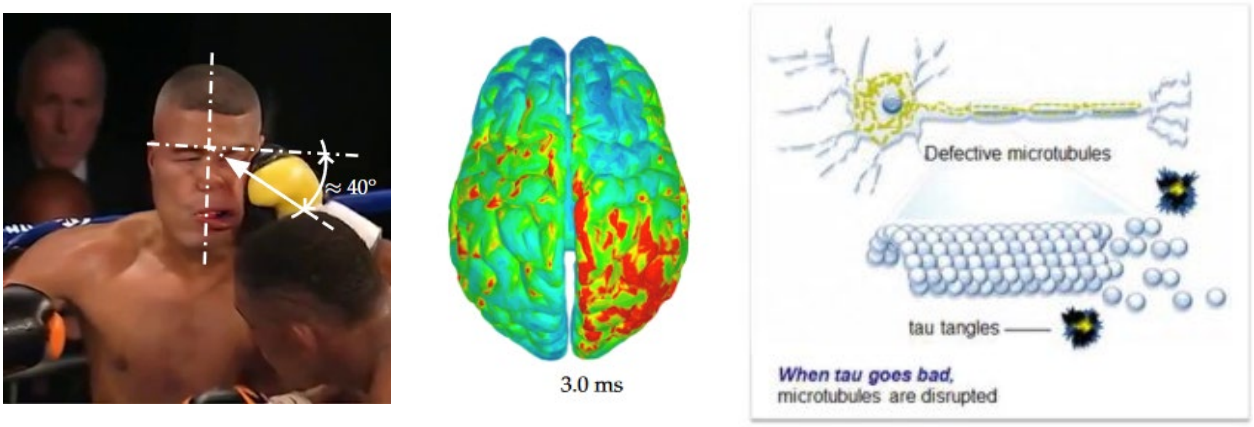

Figure 1-2: Illustration of current understanding of neurodegenerative tau aggregation. Traumatic impact to the head leads to tissue deformation in the brain[11]. This injury is linked to tau aggregation[12] in diseases such as CTE.

In this dissertation, novel research to investigate the mechanical contribution to protein aggregation is presented. Specifically, we have investigated how the mechanical strain on protein molecules during extensional fluidic flow contributes to the aggregation behavior of proteins of physiological importance. Using a combination of simulation and experimental analysis, we built upon principles of fluid mechanics to induce and enhance protein aggregation and characterize the influence that mechanical stimulus has on aggregation behavior.

1.2 Basic Fluid Mechanics

Fluid mechanics is the study of flow and seeks to explore what makes fluids move and how fluids behave while moving. This behavior can range from relatively simple to very complex, depending on the constituents of the fluid being observed. Generally, a fluid is a substance that deforms continuously when acted upon by any stress of any magnitude. How quickly a fluid deforms is proportional to its viscosity and the stress applied. A fluid whose strain rate is linearly proportional to its applied stress is called a Newtonian fluid, a category which includes water, air,

and most simple oils. If a fluid is more complex, comprising multiple heterogeneous components, the strain rate may be non-linearly proportional to the applied stress as the constituents of the fluid may have a significant influence on the flow behavior. This much larger category of complex substances are aptly called *non*-Newtonian fluids. Examples of non-Newtonian fluids include blood, which is a shear-thinning fluid that reduces viscosity at higher shear rates, and mud, which is a shear thickening fluid that increases viscosity at high shear rates.

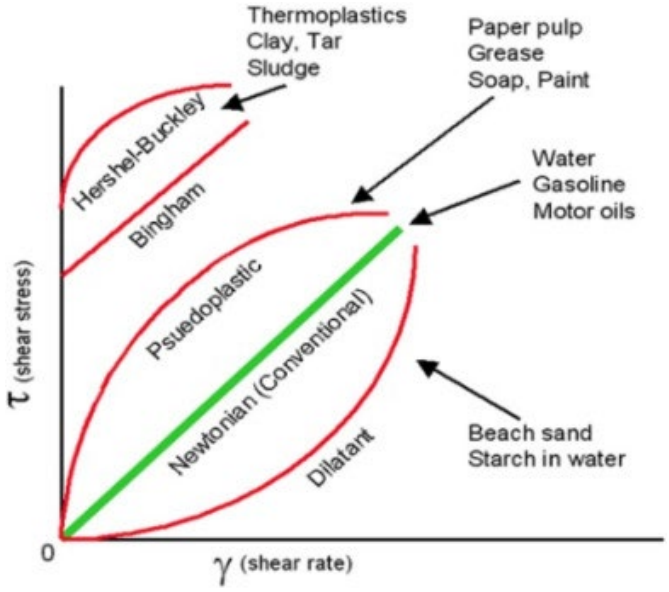

Figure 1-3: Examples of non-Newtonian fluids and how their shear stress varies with shear rate[13].

Non-Newtonian fluids also often exhibit viscoelastic behavior, as with polymer or proteinaceous solutions, where elastic components of the fluids may dominate the viscous behavior of the solvent depending on the flow regime (Figure 1-3). Viscoelastic fluids are of particular interest for biological fluid flows, as the comprised viscoelastic biomolecules have been shown to be important considerations in normal homeostatic functions of the human body as well as in the

genesis and progression of disease[14]. Additionally, the flow of viscoelastic fluids in biological applications may also play a critical role in tissue generation and chemical reaction, as the fluid flow of the solvent may enhance the reactivity and interaction between elastic molecules therein[15,16].

1.2.1 Shear Flow

In basic fluid flow applications, a fluid is said to be in *shear* as it passes through a vessel or past a wall or barrier. Assuming no-slip at the boundary of these channels, the fluid at different layers moves with different velocities, so that relative to itself, the fluid is being sheared across these infinitesimal layers. This shearing deformation is a critical consideration for non-Newtonian viscoelastic fluids, since the relative change in velocities may differentially affect the components of the fluid. For example, higher shear rates at the wall of blood vessels cause red blood cells to align and separate, allowing for relatively Newtonian behavior, where lower shear rates at the center of the vessel cause blood to flow as a plug, with cells clumped together (Figure 1-4).

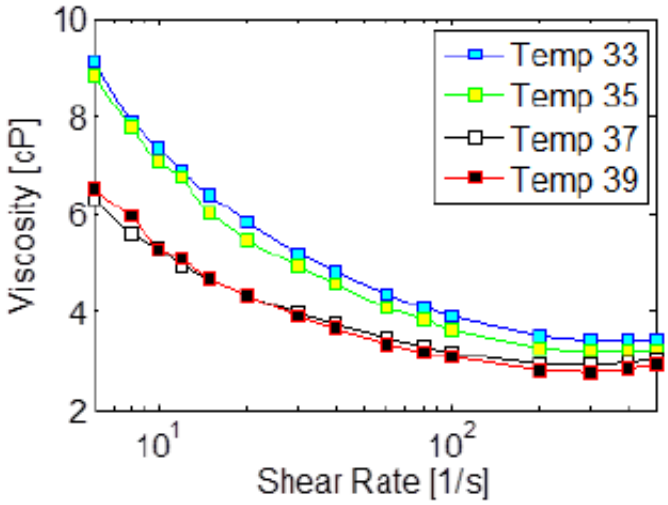

Figure 1-4: Blood viscosity as a function of shear rate and temperature[17]. Example of shear thinning fluid. Note that as shear rate increases, the viscosity of this fluid decreases at each test temperature.

1.2.2 Extensional Flow

A growing field of fluid mechanics research is extensional flow, in which the behavior of fluid is investigated when exposed to a flow field that stretches the fluid (Figure 1-5). Where shear flow has a velocity gradient perpendicular to the direction of the flow, extensional flow imposes a velocity gradient parallel to the direction of the flow. While extensional fields are rarer and harder to control, there is mounting evidence that this type of flow field is potentially immensely influential on the alignment and interaction of elastic or reactive elements of non-Newtonian fluids[15,16,18–22].

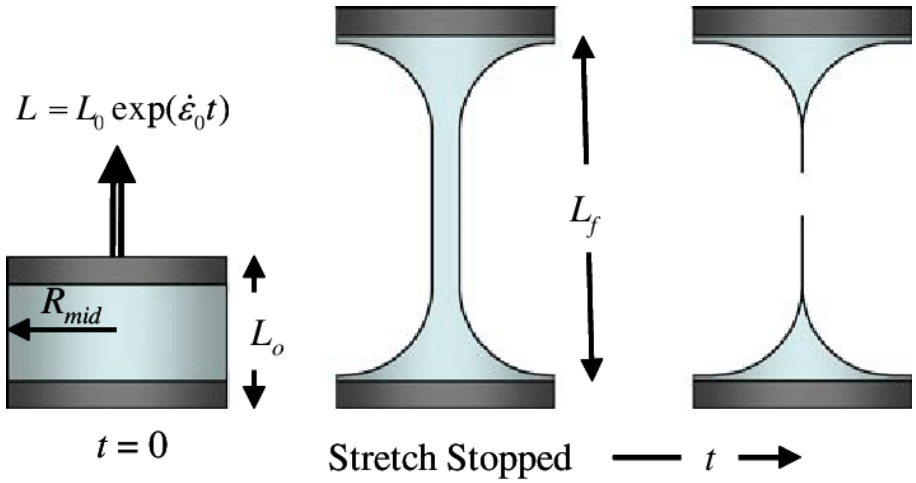

Figure 1-5: Illustration of extensional fluid flow and technique to measure extensional rheology[23].

1.3 Biological Fluid Mechanics

Fluid mechanics plays a crucial role in understanding biological systems, particularly in physiological processes involving blood flow, mucus transport, cellular mechanics, and cerebrospinal fluid (CSF) flow. Biofluids such as blood, synovial fluid, saliva, and mucus exhibit

complex rheological properties that deviate from classical Newtonian behavior, necessitating specialized fluid dynamics approaches to quantify and ultimately understand how these fluids behave and how they may contribute to and influence other biological processes (Figure 1-6).

Unlike Newtonian fluids, whose viscosity remains constant regardless of applied shear stress, biofluids often exhibit non-Newtonian characteristics, including shear-thinning and viscoelasticity. The non-Newtonian behavior of biofluids is largely governed by the presence of biopolymers and proteins, which impact viscosity, elasticity, and structural properties of fluids.

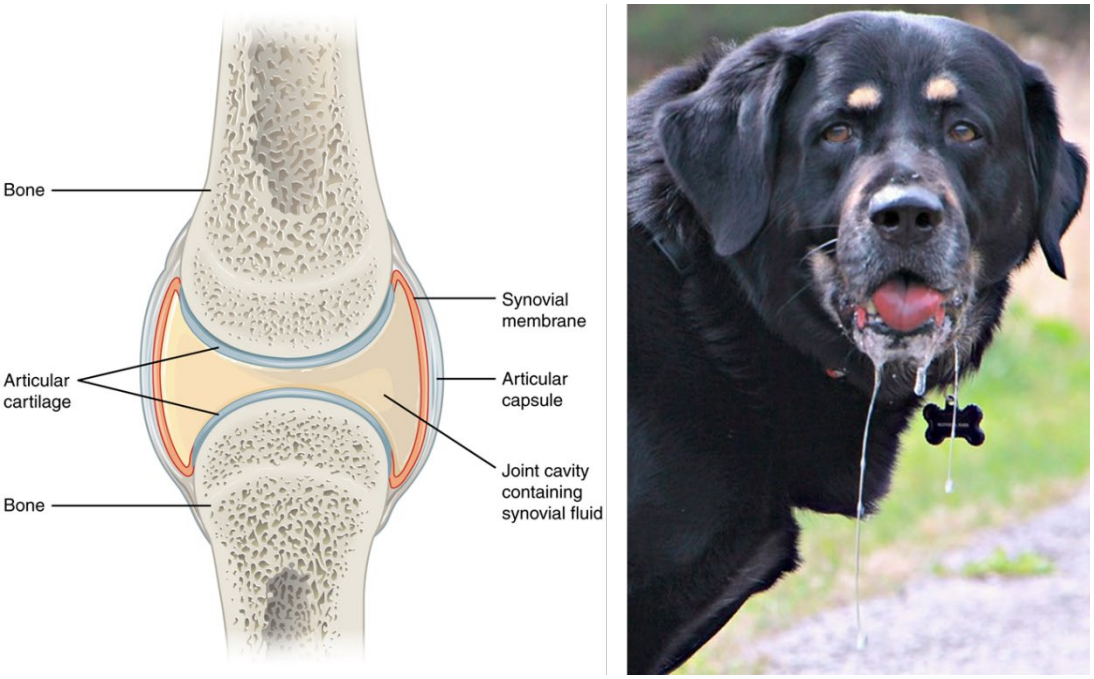

Figure 1-6: More examples of non-Newtonian biological fluids, synovial fluid[24] and saliva[25].

The study of biological fluid mechanics, particularly non-Newtonian biofluid behavior, is essential for medical applications such as blood flow modeling, drug delivery, and biomaterial design. Understanding the role of biopolymers and proteins in biofluid rheology aids in designing

better therapeutic approaches for conditions like blood disorders, cystic fibrosis (thick mucus), and osteoarthritis (synovial fluid degradation).

1.4 Brain Anatomy 101

The mammalian brain and central nervous system are immersed in a fluid environment, which serves to protect against injury and provide a pathway for nutrient delivery and waste removal from this sensitive tissue[26]. Understanding the brain's fluid mechanics is therefore essential for the characterization of many of its processes including its progression of injury and disease. The primary fluids involved in brain physiology include blood, cerebrospinal fluid (CSF), and interstitial fluid (ISF). These fluids interact dynamically to support brain function, regulate pressure, and facilitate biochemical exchange[27–29].

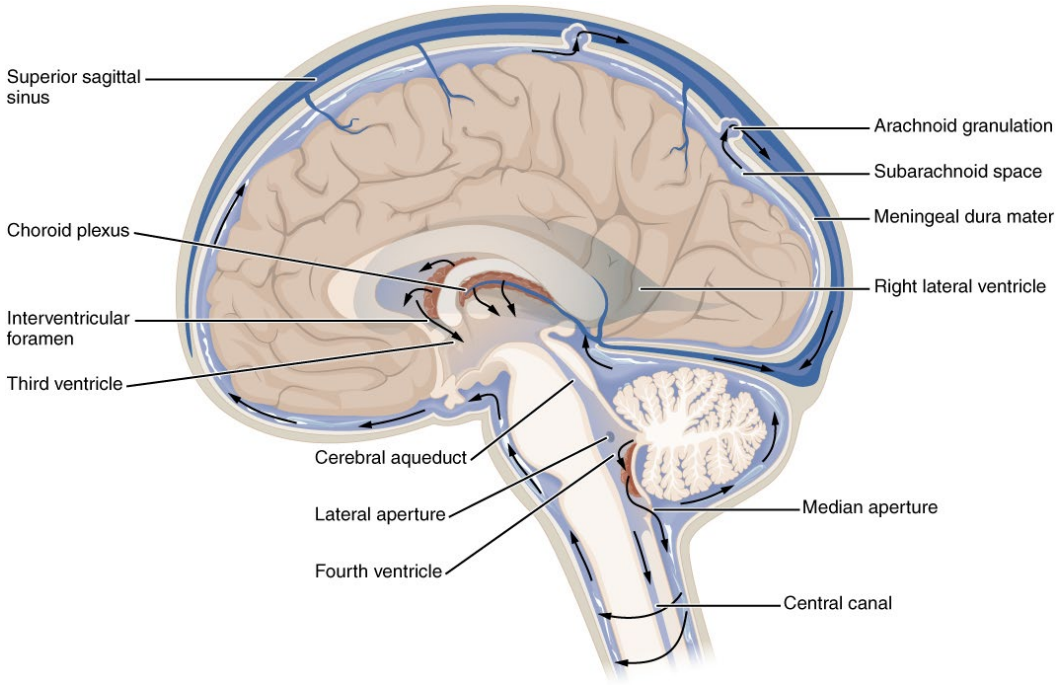

Figure 1-7: Illustration of CSF flow through the brain cavity[30].

1.4.1 Cerebrospinal Fluid and Interstitial Fluid

CSF is contained in the brain ventricles and subarachnoid spaces (Figure 1-7). In a typical adult, the volume of CSF is approximately 150ml, most of which resides in the subarachnoid spaces[26]. It is secreted into the lateral ventricles through the choroid plexus, where it travels to the third and fourth ventricles and subarachnoid spaces. CSF is then drained into the venous system via arachnoid granulations into the superior sagittal sinus[31,32]. By surrounding the brain, CSF provides buoyancy and protection against injury to the tissue, while also facilitating the exchange of nutrients and waste from the brain cells.

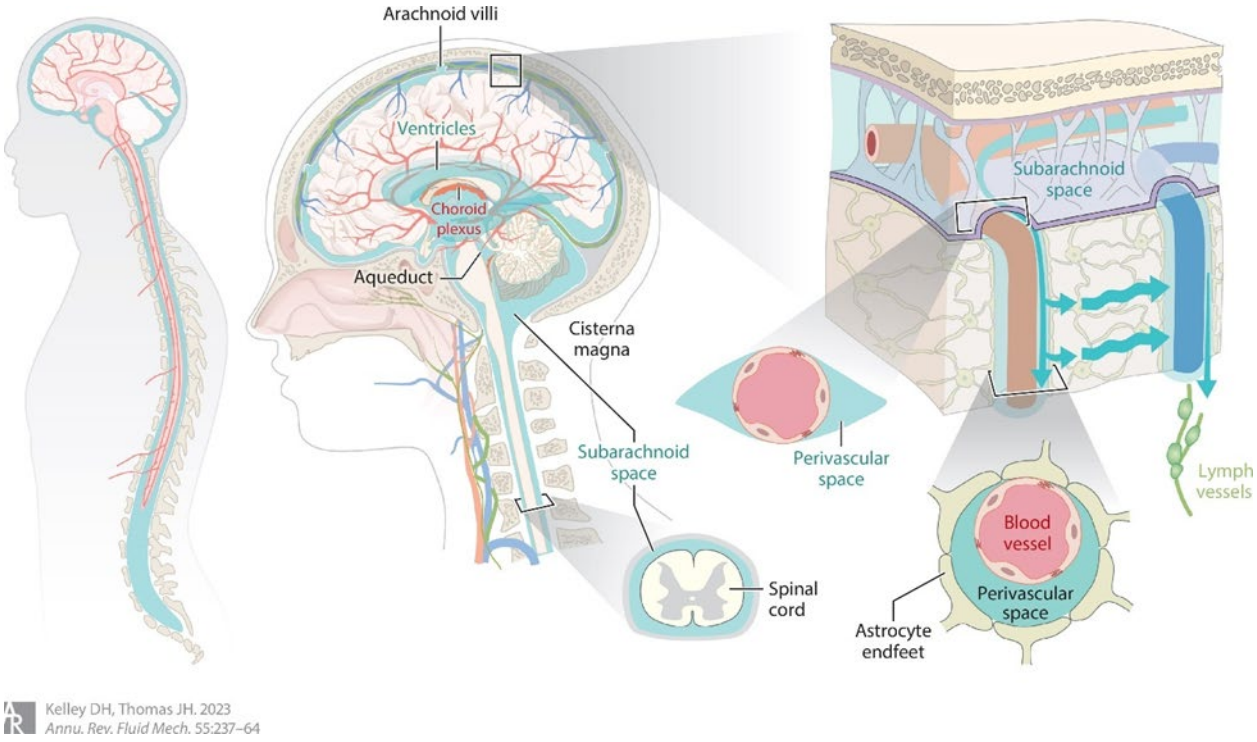

Figure 1-8: Detailed illustration of CSF flow around and through brain tissue[27].

While similar in composition and physical properties to CSF, interstitial fluid (ISF) is defined specifically as the fluid that is found in perivascular spaces of the brain (i.e. in the spaces between

the brain vasculature and brain cells), and in the extracellular spaces of brain parenchyma. It is in ISF in which the biochemical exchanges between CSF and brain cells take place, and so the nutrients and waste it carries can result in significant differences in its local composition.

Understanding the interplay between blood, CSF, and ISF flow aids in diagnosing and treating neurological disorders such as stroke, hydrocephalus, and neurodegenerative diseases. For example, because the skull is a relatively rigid structure, evolutionarily designed to protect the brain from injury, the cranium cannot grow or shrink to accommodate increased or decreased blood volume, as other bodily tissues can. Without a mechanism to accommodate the change in blood volume, the pressure of the system could dangerously vary, and is associated with many neurological deficits and headache symptoms. Fortunately, the CSF flows from the rigid vessel of the cranium to the more flexible spinal column to accommodate increases in cerebral blood volume while mitigating its adverse pressure effects[29].

The interplay between CSF and ISF as well as the nutrient, waste, and other particle exchange these fluids facilitate are also the subject of much interdisciplinary research (Figure 1-8). It has long been suggested that these fluids, which surround the entire brain tissue, may provide a pathway for waste clearance as it permeates the extracellular space and flows towards eventual drainage in the arachnoid granulations[33]. Not unlike the lymphatic system of the rest of the body, this pathway has been hypothesized to be facilitated by glial cells which transport water through brain tissue utilizing the aquaporin-4 protein (AQP-4). This system has been dubbed the *glymphatic* system, a portmanteau of glial cells and lymphatic[28,34,35].

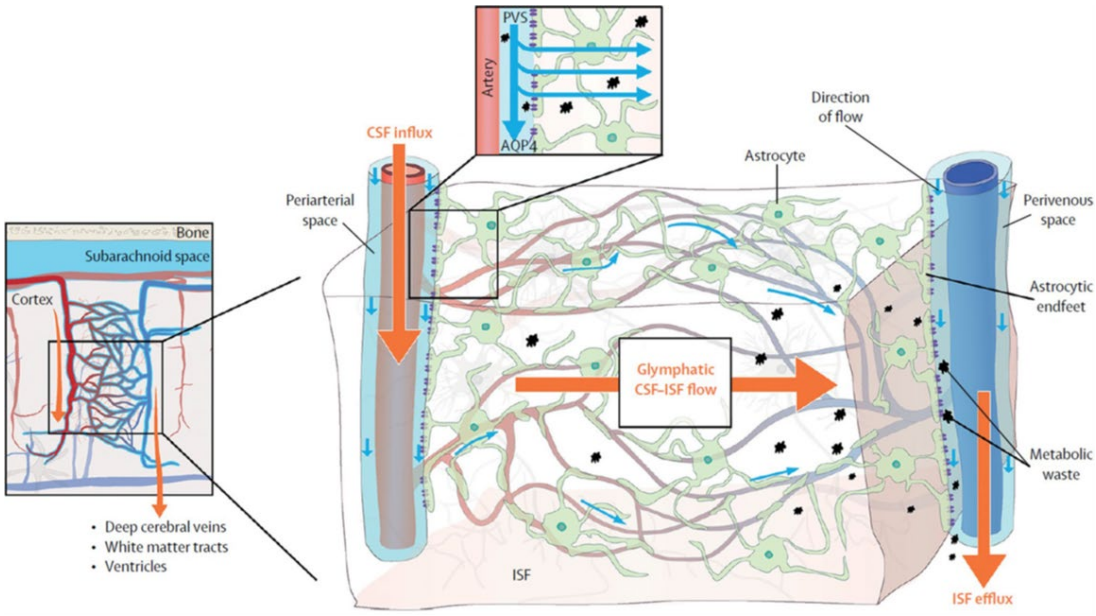

Figure 1-9: Illustration of proposed glymphatic system[14].

In the proposed glymphatic system (Figure 1-9), CSF flows from the ventricles deeper into the brain tissue through the perivascular spaces immediately surrounding arteries and arterioles. This flow has been shown to be enhanced by the pulsations of the cardiovascular system, driving fluid deep into tissue where it is exchanged into the parenchyma through the semipermeable membrane of the glial cell and astrocytic end-feet[34]. Once inside the tissue, the fluid, now called interstitial fluid (ISF), flows within the extracellular space, picking up cellular waste on its way to the perivenous spaces where it eventually flows back to the subarachnoid spaces and deposited in the arachnoid granulations and lymphatic system. This system is enhanced during sleep, as perivascular spaces and extracellular spaces are increased, thus allowing for more fluid flow[36]. If this system can be confirmed, it will be an impactful contribution to our understanding of critical brain processes, neurodegenerative diseases, and even an answer to an age-old question: why do we *need* to sleep?

Though there has been compelling evidence that this proposed mechanism indeed drives flow deep into brain tissue, the assumption that the flow enters the tissue, advects waste material, and is ultimately deposited into the lymphatic system is currently only speculative, and very little evidence exists confirming the latter stages of the system. The fluid environment and flow conditions of the brain are still poorly understood, and much can be learned from taking a mechanical perspective of these fluidic systems. From basic biological functions to the progression and propagation of disease, understanding the fluid mechanics of the brain has enormous potential to greatly enhance the simulation, diagnosis, and treatment of the human body.

1.5 Protein Structure and Mechanical Behavior

Proteins are essential biological macromolecules that perform a wide variety of functions within living organisms. They act as enzymes, catalyzing biochemical reactions; as structural elements, giving cells shape and mechanical strength; as transporters, carrying molecules across membranes and through fluids; and as signaling molecules, regulating communication between cells. Additionally, proteins contribute to immune defense, energy storage, and the mechanical movement of muscle and cytoskeletal components.

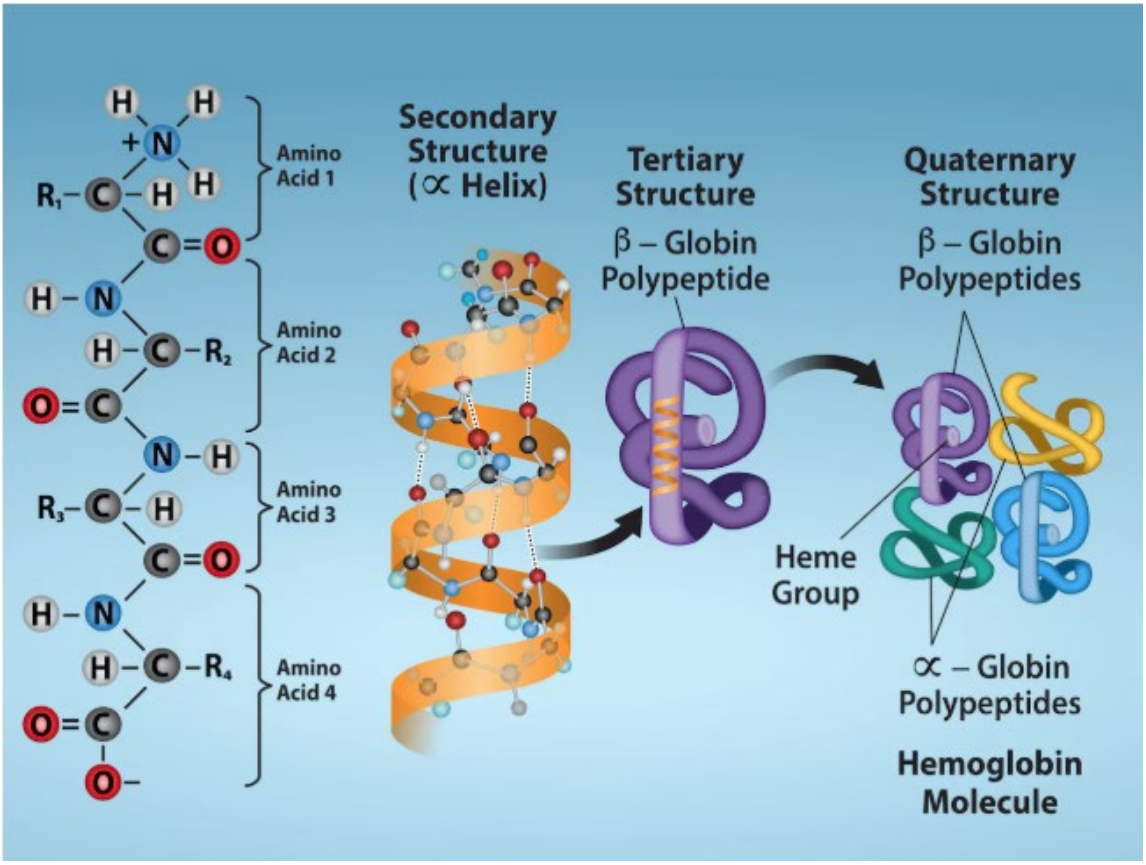

Figure 1-10: Illustration of protein primary, secondary, tertiary, and quaternary structures[37].

Mechanically, proteins are composed of long chains of amino acids linked by peptide bonds, which fold into complex three-dimensional structures (Figure 1-10). This structure is organized into four hierarchical levels:

1) Primary structure — the linear sequence of amino acids.

2) Secondary structure — local folding patterns such as alpha helices and beta sheets, stabilized by hydrogen bonds.

3) Tertiary structure — the overall three-dimensional shape of a single polypeptide, driven by hydrophobic interactions, disulfide bonds, and other forces.

4) Quaternary structure — the assembly of multiple protein subunits into larger complexes.

From a mechanical perspective, proteins behave like nanoscale machines or scaffolds. Some, like titin in muscle fibers, are capable of stretching and recoiling under load, exhibiting elasticity[38]. Others, such as collagen, form strong, fibrous structures that resist tensile forces[39]. Globular proteins can undergo conformational changes that act like switches or levers, allowing them to perform dynamic tasks such as binding, transporting, and mechanical force generation within cells and tissues[40].

1.5.1 Intrinsically Disordered Proteins (IDPs)

One classification of proteins that are the focus of many of these neurodegenerative diseases is intrinsically disordered proteins (IDPs). IDPs are proteins that do not form uniquely defined 3-dimensional structures, even under non-denaturing conditions[41,42]. The existence of IDPs and the fact that they facilitate essential biological functions is significant because it breaks a commonly held belief that only 3-D structured proteins served essential functions in addition to their association with several neurological diseases such as Alzheimer's, Parkinson's, CTE, and prion diseases such as Cruetzfeldt-Jakob disease or Bovine spongiform encephalopathy (Mad Cow disease)[42].

It has been suggested that IDPs, unlike more stably structured proteins, have more than one ground energy state, the thresholds for which are relatively low at normal temperatures[43] (Figure 1-11). Therefore, normal mechanical processes may provide sufficient free energy to induce conformational changes in these proteins, leading to abnormal aggregation. Since Tau and Tau aggregates are found in the brain or produced in labs in fluidic environments, we also hypothesize that fluidic stresses and strains may be an appropriate catalyst for these conformational changes.

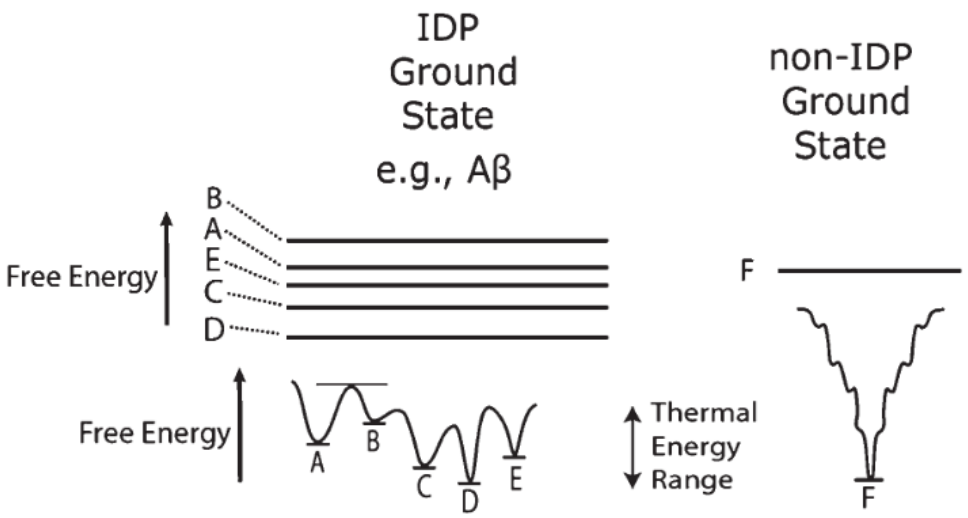

Figure 1-11: Illustration of a distinction between IDPs and non-IDPs. IDPs have several ground states, between which they can move relatively easily. Non-IDPs have fewer, and the activation energy to conformationally change these proteins is relatively high[43]

1.6 Fluid Mechanics of Protein Aggregation

The interaction between polymers and biological fluid flow is a complex, but critical process to understand, as it significantly contributes to a cascade of many important biological functions[44]. Not only does the presence of proteins within biofluids impact the fluids' rheology and flow behavior, the fluid flow has been shown to reciprocally influence the protein behavior[45].

Rheology is the study of the flow properties of complex fluids and the influence a fluid's constituents have on its flow behavior. In the words of Dr. Ewoldt, rheology seeks to answer the question: what happens when I poke it[46]? The unique structure of proteins cause a unique interaction with a fluid, resulting in interesting non-Newtonian behavior. The crosslinking, aggregation, and folding of protein molecules within fluids can have a significant influence on flow behavior and have myriad applications in biological fluids, industrial processes, and even food and drug industries[20].

Proteins significantly influence fluid flow by altering the rheological properties of biological and engineered fluids. In biofluids such as blood, synovial fluid, and mucus, proteins contribute to non-Newtonian behavior, affecting viscosity, elasticity, and shear-thinning characteristics[44]. For example, plasma proteins like fibrinogen enhance blood viscosity at low shear rates by promoting red blood cell aggregation, while mucins in mucus form polymeric networks that increase viscoelasticity, impacting flow resistance and transport properties. In cerebrospinal and interstitial fluids, proteins influence colloidal stability and diffusion, affecting the clearance of metabolic waste through the glymphatic system[33]. In industrial applications, protein aggregation and denaturation in biopharmaceuticals can alter flow behavior, leading to clogging or instability in drug formulations[47]. Thus, proteins play a crucial role in modulating fluid dynamics across biological and synthetic systems, necessitating careful consideration in both medical and engineering applications.

Fluid flow fields can also have significant impacts on the behavior of proteins. It has been shown that inducing certain fluid flow fields can induce protein aggregation and enhance the interaction of proteins with other molecules[20,48]. Again, shear flow and extensional flow may play a big role in flow induced protein interaction, as the gradient of velocities may cause a stretching phenomenon leading to conformational changes in protein structures.

1.6.1 Shear flow

Fluidic shear and extension have been shown to facilitate and even accelerate protein aggregation as well as other chemical reactions and processes[20,49]. The mechanism for facilitating this aggregation is believed to be the changing of the protein structure, allowing for solvent accessibility and the exposure of interlinking sites between adjacent proteins, thus accelerating reaction and aggregation[21,22].

When a fluid passes by a surface, the velocity of the fluid very close to the boundary moves much slower than the fluid far away. This discrepancy is called shearing, and potentially has significant impact on IDPs such as Tau[48,50,51]. If a protein is caught in a region where each end is experiencing a different velocity of flow, the applied shear stress may be sufficient to cause conformational changes and potentially break the hydrogen bonding keeping the protein structure compact[48,50,52] (Figure 1-12). Recent studies have observed shear stress being a possible cause of aggregation, adsorption to capillary walls, and potentially prion-like behavior "seeding" larger aggregates[43,53].

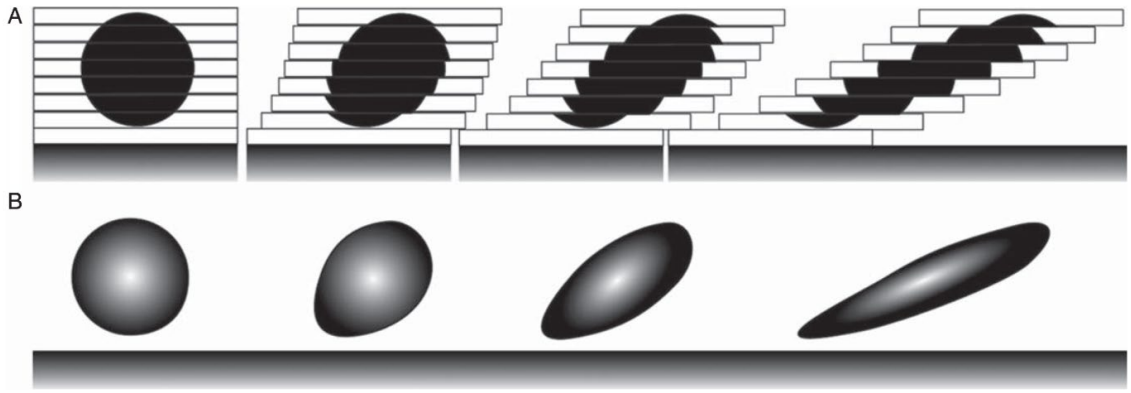

Figure 1-12: Illustration of how a flexible particle near a wall may be sheared into a conformational change[43,54].

1.6.2 Extensional flow

In addition to shear motion, a fluid can also be subjected to an extensional field, where a fluid element is stretched, for example due to a constriction of flow causing acceleration. Extensional Aggregation is a mechanism not well understood, but that has the potential to explain many biological and industrial phenomena involving proteinaceous or polymer solutions[20,22]. While it is

difficult to separate extensional and shear flows, there is mounting evidence that extensional flow may have a more significant impact on the seeding and abnormal aggregation of proteins[15,16,18,22].

For example, Calabrese et al. showed that colloidal rods have a tendency to align with one another along the direction of flow much more frequently in extensional flow than in shear flow (Figure 1-13)[18]. Furthermore, their results showed that as the intensity of the flow field increased, this effect was more pronounced, showing more aligned rods in strong extensional flows than in shear flows.

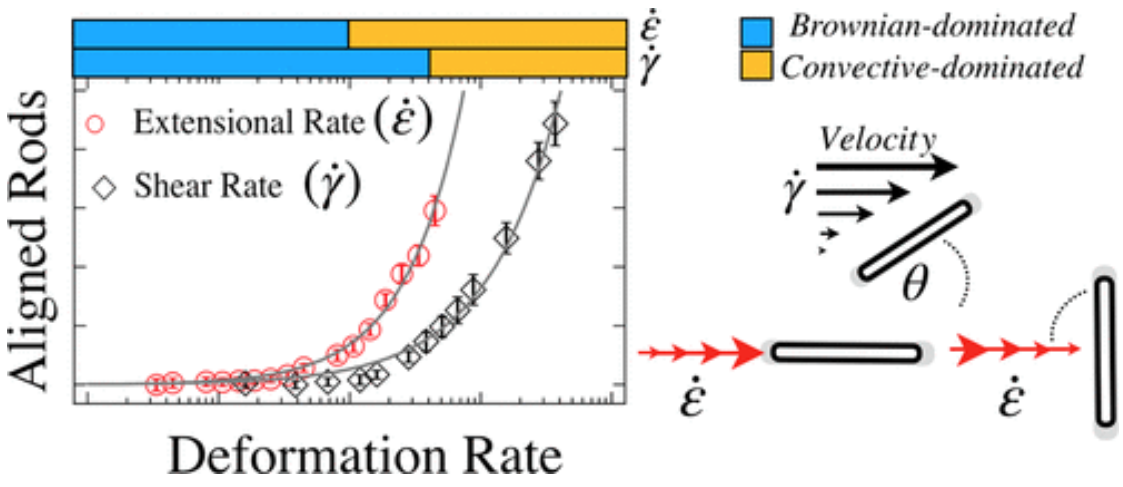

Figure 1-13: Results of Calabrese et al. In extensional flow fields, more colloidal rods aligned in either parallel or perpendicular orientation to the flow. In shear flow, the rods were dominated by Brownian motion[18].

Since many proteins can be approximated as long, string-like molecules, it is hypothesized that extensional flows may also cause these molecules to align which may potentially lead to interaction and thus aggregation. In fact, Paten et al. showed a similar behavior, that when a collagen solution is subjected to an extensional flow, the molecules align and crystallize into fibers (Figure 1-14)[15].

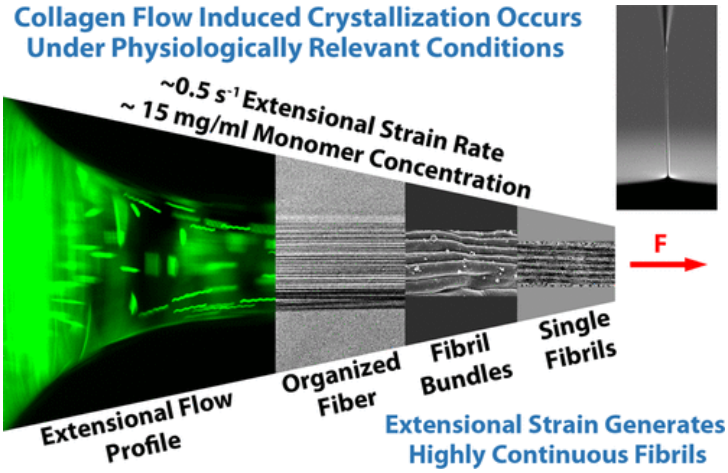

Figure 1-14: Flow induced crystallization of fibers from a droplet of collagen solution. Paten showed that it is possible to induce crystallization of collagen fibers under extensional flow fields of physiological relevance[15].

Extensional flow fields can be generated in several ways, including a four-mill roller, opposing jets, or cross-slot flow (Figure 1-15). Each of these could also be adapted to microfluidic devices. A limitation of these types of devices is simultaneous application of shear and extensional strain in different parts of the device. Avoiding shear stress, however, often requires experiments to be conducted in such a way that would convolute the extensional affects with interfacial phenomena[55]. Dobson et al devised a simple mechanism to create repeated extensional strains, which they showed could induce protein aggregation as well as deconvolute the effect of extensional strain from shear strain[20]. A similar mechanism can be built and optimized for the study of Tau. For example, as this experiment is designed to simulate life-like environments, the intensity of the flow field must more closely resemble physiologically relevant flows.

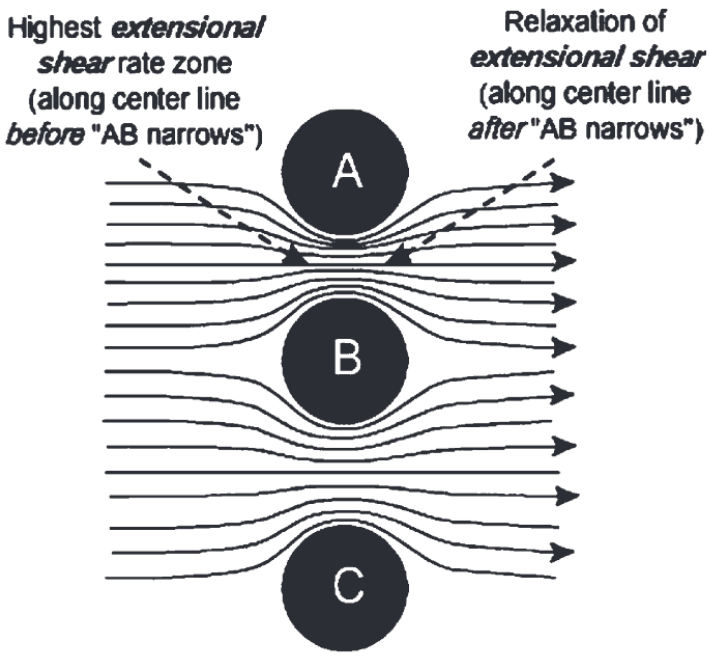

Figure 1-15: Example of extensional flow field created by the constriction of flow from a larger channel into a smaller channel[48,54].

1.7 Brain Disease Pathology

Proteinopathies are neurodegenerative conditions caused by the misfolding, aggregation, and accumulation of specific proteins that become toxic to neurons and disrupt normal brain function[56]. These pathological protein aggregates interfere with cellular processes, induce oxidative stress, and trigger chronic inflammation, ultimately leading to progressive neuronal death and brain atrophy. Common to all proteinopathies is the body's failure to properly clear or degrade these misfolded proteins, leading to their buildup in specific brain regions and the disruption of both neural signaling and fluid transport systems that are critical for brain homeostasis[57].

Alzheimer's disease (AD) is the most prevalent proteinopathy and is marked by the accumulation of extracellular amyloid-beta plaques and intracellular tau neurofibrillary tangles.

These protein deposits damage synaptic function, disrupt neuronal communication, and impair cerebrospinal and interstitial fluid clearance through the glymphatic system, contributing to the spread of pathological proteins throughout the brain. In chronic traumatic encephalopathy (CTE), often linked to repeated head injuries, the primary protein involved is hyperphosphorylated tau, which accumulates in the depths of brain sulci and around small blood vessels. The mechanical forces from trauma appear to initiate tau misfolding, leading to progressive behavioral, mood, and cognitive symptoms that worsen over time[57].

Prion diseases, such as Creutzfeldt–Jakob disease (CJD), represent a unique and highly aggressive class of proteinopathies where misfolded prion proteins (PrP^Sc) propagate by inducing normal prion proteins (PrP^C) to misfold in a chain reaction. This leads to widespread neuronal loss, spongiform changes in brain tissue, and rapid neurological decline. Unlike other proteinopathies, prion diseases are transmissible and highlight the extreme consequences of unchecked protein misfolding and aggregation. Across all these disorders, proteinopathy pathology not only damages neurons but also impairs brain fluid dynamics and clearance mechanisms, creating feedback loops that exacerbate protein accumulation and neurodegeneration[1].

1.8 Hypothesis

We hypothesize that fluid flow, and especially extensional fluid flow will play a significant role in the initiation, propagation, and progression of tauopathies such as chronic traumatic encephalopathy, which is causally linked to mechanical head injuries. To demonstrate this, extensional fluid flow will be utilized to develop a novel rheological technique and characterize the extensional flow properties of biofluids. Using this technique, protein aggregation behavior

can be further characterized by subjecting protein solutions to variable extensional strain rates and durations to elucidate information about how extensional flow contributes to protein aggregation and can be used to analyze, predict, and diagnose clinically relevant protein aggregation.

1.9 Dissertation Summary

In this dissertation, I will present a study of extensional fluid flow and rheology with implications for neurological applications in three parts. In the first part, demonstration of a novel microextensional rheological method will be presented in which the efficacy of ocular surgical tools is compared. In the second, an updated characterization of cerebrospinal fluid rheology is presented using state-of-the-art rheological techniques. Finally, the aggregating behavior of protein is characterized, and a phase diagram is presented, representing a novel framework for understanding protein aggregation in response to extensional strain rates of varying magnitude and duration.

Chapter 2 : Rheological Methods

2.1 Introduction

Evidence of some of the earliest bio-rheologists can be traced back to at least the 1850's[58]. Using cervical mucus, fertility practitioners developed a method to predict ovulation by observing the liquid quality of the fluid. In fact, this method is still commonly practiced by lay people today and is used as one of an arsenal of techniques to analyze and diagnose different conditions (Figure 2-1). This and traditional techniques like it are necessarily subjective and qualitative, but indicate that much can be learned from the careful and thoughtful application of rheology in biomedical applications.

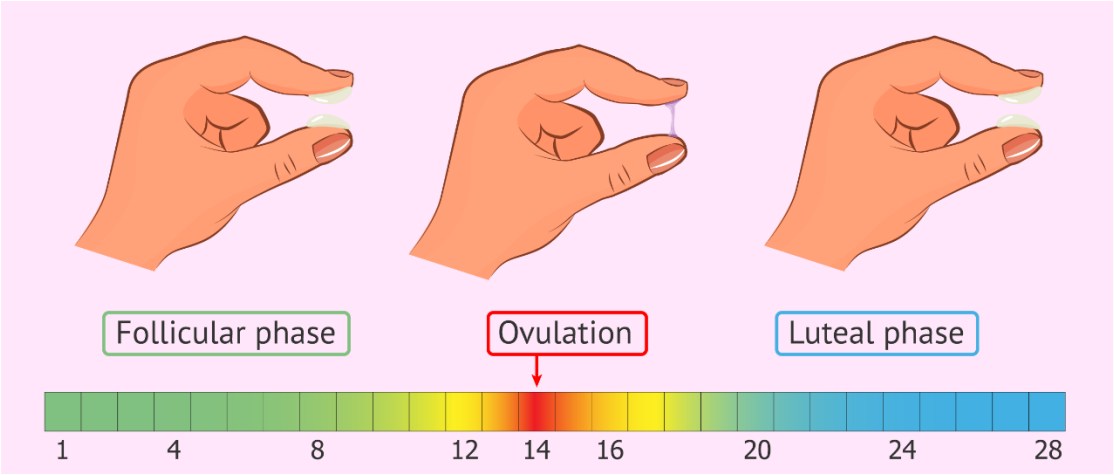

Figure 2-1: Manual extensional rheology of cervical mucus used to predict ovulation[59].

The history of modern and quantifiable rheological techniques dates to the early 20th century, emerging from the need to understand and quantify the flow and deformation behavior of complex materials beyond simple Newtonian fluids. Early work by pioneers such as Eugene Bingham and

Markus Reiner laid the foundation for defining key rheological concepts like viscosity, elasticity, and plasticity. The first instruments, such as capillary viscometers and simple rotational viscometers, allowed scientists to measure fluid resistance under steady flow conditions. Over time, technological advancements led to the development of more sophisticated tools, including oscillatory rheometers, cone-and-plate devices, and extensional rheometers, enabling precise characterization of viscoelastic, time-dependent, and shear-dependent behaviors.

In this chapter, the methods used to quantify and analyze rheological properties of biological fluids are presented. Using a state-of-the-art shear rheometer, we are able to quantify many rheological properties of many complex fluids, capturing non-Newtonian behavior resulting from the viscoelastic constituents of the fluids. Furthermore, using a recently developed microextensional rheometric technique, significant non-Newtonian behavior can be measured on samples of volumes of less than 100uL, and as low as 10 uL[19]. This allows important mechanical properties to be discerned from biological samples which may be prohibitively expensive to produce or invasive to extract.

As mentioned in chapter 1, the human brain and central nervous system is a complex and dynamic fluid system, composed of several different fluids each with important physiological and mechanical functions. Therefore, any study of the mechanical dynamics of the brain environment will require the fluids within to be adequately characterized. Using the methods described in the following sections, we have demonstrated the ability to characterize different biological fluids and tissues, many for the first time. In so doing, we can reveal new information about these fluids which could potentially lead to new insights about how their characteristics contribute to the generation and propagation of neurodegenerative disorders and other diseases.

2.2 Shear Rheology

Shear rheology utilizes basic Couette flow in order to measure the viscosity of fluids. For Newtonian fluids, the shear stress is linearly proportional to the shear rate applied to the fluid. The relationship between shear rate and shear stress is the viscosity. Therefore, a viscosity measurement is dependent on the rate of movement between two bounding surfaces (shear rate), the geometry of the surfaces (area and gap size), and the force required to move the surface through the fluid (shear stress). For torsional rheometers (Figure 2-2), measurement of viscosity is achieved by placing a fluid between two rotating surfaces and measuring the torque required to maintain a level of shear rate.

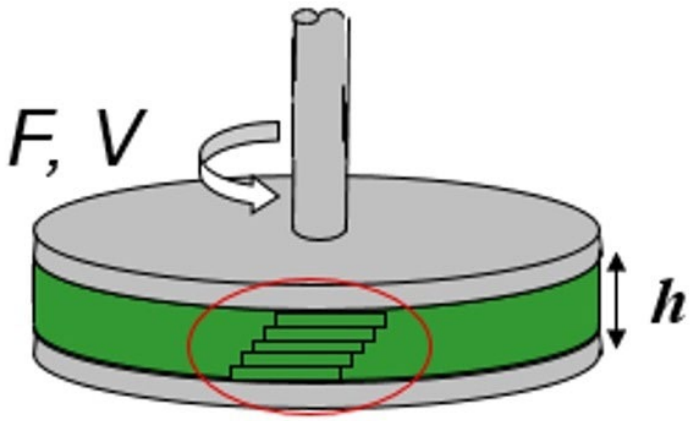

Figure 2-2: Basic shear rheology using a rotating parallel plate geometry[60]

2.2.1 Cone and Plate

For relatively small sample volumes, a cone and plate rheometer can be used to measure a wide range of viscous fluids. The formula for the viscosity measurement for a given torque reading is below. Thus, by manipulating the rotational speed and cone diameter, the viscosity of a fluid can be measured very accurately. The greatest benefit for cone and plate rheometer geometries is that

a constant shear rate can be applied to the fluid sample, thus reducing secondary flow effects within the sample. One drawback, however, is that at higher shear rates, the secondary flow effects become significant.

$$\mu(T) = \frac{3T\alpha}{2\pi R^3 \omega} \tag{2.1}$$

2.2.2 Concentric Cylinders

For low viscosity fluids, a concentric cylinder rheometer is ideal. Due to the large surface area between the rotating surfaces, the torque applied to the rheometer is high, thus amplifying the viscous effect of low viscosity fluids. Additionally, due to the low interface between the fluid and air, secondary effects from instabilities, turbulence, or interfacial phenomena are also minimized. Due to the large gap, concentric cylinder rheometers are also often a good choice for heterogeneous fluids, where a large gap is needed to accommodate finite particles. A drawback of concentric cylinder rheometers, however, is that a relatively large sample volume is needed, often greater than 10mL.

$$\mu(T) = \frac{2T d_{gap}\pi}{4\pi^2 h(R+r)^3 \omega} \tag{2.2}$$

2.2.3 Parallel Plate

For heterogeneous fluids and even viscoelastic solids, parallel plate rheometer geometries is often a good choice. Although the shear rate throughout the sample is not constant, the simplicity of the parallel plate geometry allows for flexibility to measure irregular fluids viscoelastic solids. The gap between the plates can be adjusted to accommodate samples without inducing structural changes, even allowing for relatively large biological particles like tissue or fat to be analyzed.

Parallel plates are often used for oscillatory tests, in which the loss and storage moduli can be measured, indicating the relative viscous and elastic characteristics of a sample.

$$G' = \frac{\sigma_0}{\gamma_0}\cos(\delta) \tag{2.3}$$

$$G'' = \frac{\sigma_0}{\gamma_0}\sin(\delta) \tag{2.4}$$

$$\tan(\delta) = \frac{G'}{G''} \tag{2.5}$$

With these methods, myriad simple and complex fluids can be characterized. Recently, we have used these methods in new applications such as liquid metals[61], permanent magnetic fluids[62], and human orbital fat tissue[63]. From Newtonian fluids like water and oils, to non-Newtonian viscoelastic fluids and gels such as blood and foams, shear rheology has been proven time and again to be a powerful tool in understanding the mechanical characteristics of fluids.

2.3 Extensional Rheology

Extensional rheology is a growing field where the properties of fluids are analyzed as they are subjected to extensional strain rather than the more typical shear strain (Figure 2-3). There are many applications where extensional strains are important, especially with biological materials. The cross-linking and molecular interaction of polymers and proteins in solution cause fluids to exhibit non-Newtonian behaviors in extensional flow[64]. These effects, however, cannot be fully characterized with shear rheology alone.

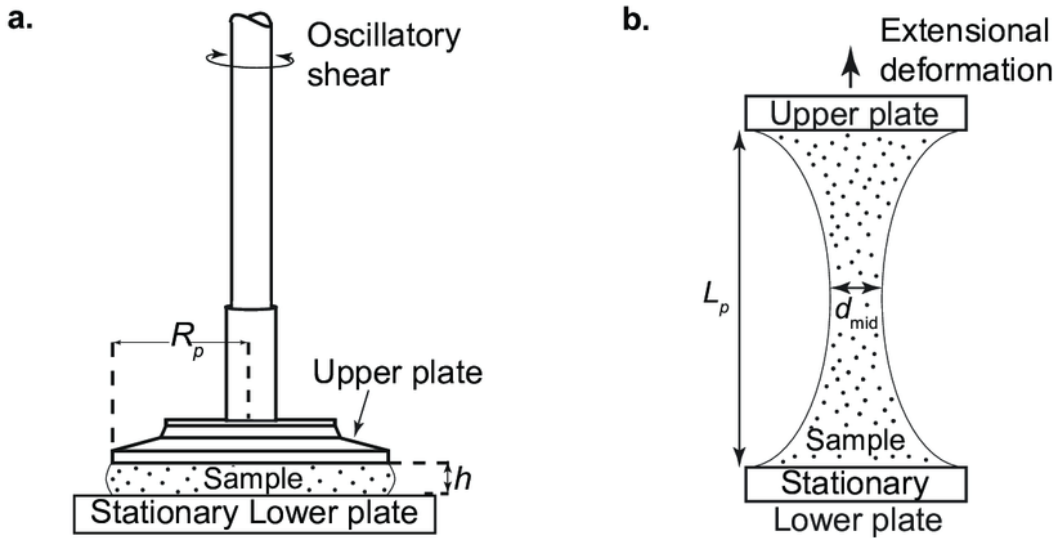

Figure 2-3: Illustrated comparison of shear and extensional rheology[65]

Extensional behavior of protein and polymer solutions is characterized by the formation of fluid structures where elastic protein interactions dominate the fluid flow. Lower molecular weight solutions exhibit relatively weak protein interaction, and purely Newtonian solutions such as water and basic saline solution show no interaction at all[66]. Recently, a method for measuring extensional flow characteristics was developed that uses a highspeed camera to capture dripping behavior of fluids[19]. As a droplet of fluid drips onto a substrate, the fluidic structures that emerge change over time, influenced by the proteins or polymers within. A strongly polymeric or proteinaceous fluid will exhibit two distinct regimes, an inertia-capillary regime that is dominated by the gravitational flow of the fluid followed by an elasto-capillary regime that is dominated by the interaction of the elastic molecules, creating a thread-like liquid bridge between the dropped droplet and the fluid source[67] (Figure 2-4).

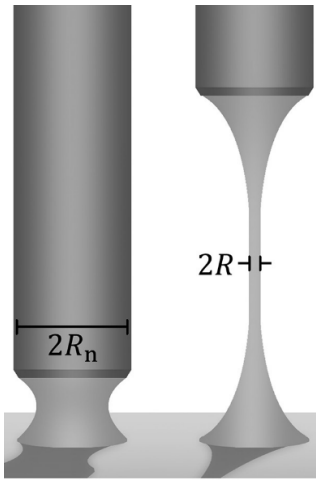

Figure 2-4: Liquid bridge that emerges during extensional rheology[68].

2.4 Rheology Methods

In Chapters 4 and 5, the specific procedures and results of our rheological testing will be presented. The following describes the general methods used to characterize the different fluids.

2.4.1 Shear Flow

To investigate the shear-rate dependence of the rheology of the fluids tested, a Discovery HR-3 rheometer (TA Instruments, New Castle DE, USA) was employed. The rheometer was used with either a parallel plate, cone and plate, or concentric cylinder attachment, depending on the fluid. The rheometer operates by dispensing a fluid between a rotating probe geometry and a stationary geometry. The sample fills the gap and a motor within the instrument rotates the probe at a prescribed angular velocity while simultaneously measuring the amount of torque required to maintain that velocity. Given the known geometry of the probe attachments, this torque reading can be analyzed to measure a host of rheological properties.

2.4.2 Extensional Flow

To analyze the extensional rheological properties of our biological fluids, we adapted a simple rheometric method to apply a large strain rate to the samples (Figure 2-5). A droplet, typically between 50-100 uL, was dispensed onto a hydrophobically treated substrate to create a domed droplet. Using a KRUSS tensiometer (K-100, KRUSS GmbH, Hamburg, Germany) in the Surface Tension setting, the droplet was penetrated with a 1 mm diameter platinum rod. The probe penetrated 0.5 mm into each sample and was quickly removed so that the surface of the sample was perturbed upward. Each sample was separated into three droplets, and each droplet was tested independently three times. Testing was performed at room temperature.

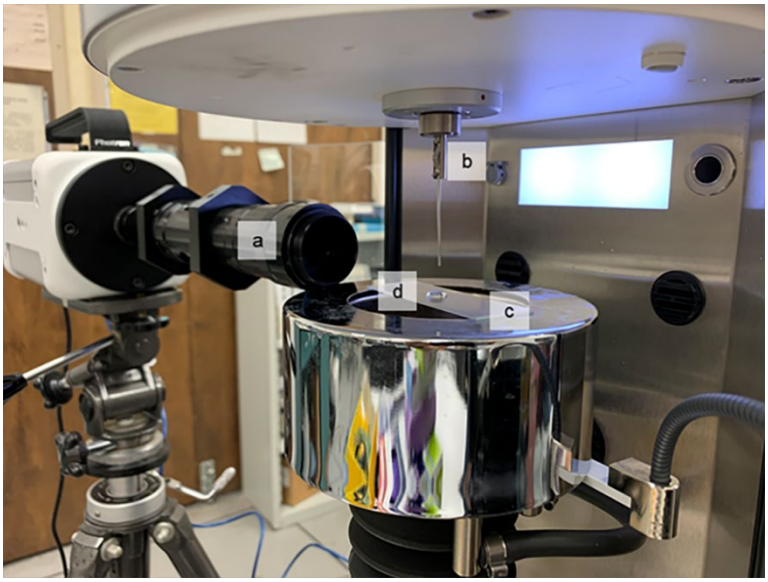

Figure 2-5: Micro-Extensional rheology test apparatus (a) Photron High Speed camera, (b) Kruss K-100 tensiometer with 1mm platinum probe, (c) hydrophobically treated surface, (d) liquid sample.

As the sample dripped from the probe, an elasto-capillary liquid bridge formed between the probe and the droplet. A high-speed camera (NOVA R2, PHOTRON USA INC., San Diego, USA) set to 20,000 frames per second and 1/25,000 s-1shutter speed captured the evolution of the liquid

bridge. The high-speed images were processed to analyze the evolution of the liquid bridge over time using a method adapted from Dinic et al[67]. The exponentially decaying portion of these data were fit to the following relationship (Equation 2) developed by Entov and Hinch[69], which describes the decay of the elastocapillary bridge that occurs during pinch-off of protein solutions. R0, GE, and σ are initial radius, elastic modulus, and surface tension of the fluid sample, respectively.

$$\frac{R(t)}{R_0} = \left(\frac{G_E R_0}{2\sigma}\right)^{1/3} exp\left(\frac{-t}{3\lambda_\varepsilon}\right) \tag{2.6}$$

From this model, the extensional relaxation time (λ_ε) of the elasto-capillary regime was calculated for each trial. Longer λ_ε values correlate to higher protein concentration and greater cross-linking in the sample. Shorter relaxation times correlate to lower protein concentration[64].

2.5 Summary

Rheology is a critical field to consider when seeking to understand the mechanical behavior of the human body, as so much of biological processes occur in a tangible fluid environment. Together, these shear and extensional techniques form the experimental backbone for the analyses performed in the following chapters. They enable detailed characterization of fluid mechanical properties, essential for elucidating the physiological and pathological roles of biofluids in health and disease. By integrating these rheological approaches, we can establish a comprehensive framework to investigate how the complex mechanical behaviors of biological fluids contribute to the dynamic fluidic environment and functions of the human body, with emphasis on brain physiology and pathology.

Chapter 3 : Protein Aggregation Materials and Methods

3.1 Introduction

The study of protein aggregation has evolved significantly over the past century, driven by advancements in biochemistry, molecular biology, and biophysics. Early observations of protein aggregation date back to the late 19th and early 20th centuries[70], when scientists studying protein solubility and denaturation noticed that certain conditions—such as heat, pH changes, and mechanical stress—could cause proteins to clump together irreversibly. In the mid-20th century, research into diseases like Alzheimer's, Parkinson's, and prion disorders revealed that protein aggregation played a central role in neurodegeneration[71]. Studies on amyloid fibrils, pioneered by Astbury in the 1930s and 1940s, provided some of the first structural insights into misfolded protein assemblies[72–74].

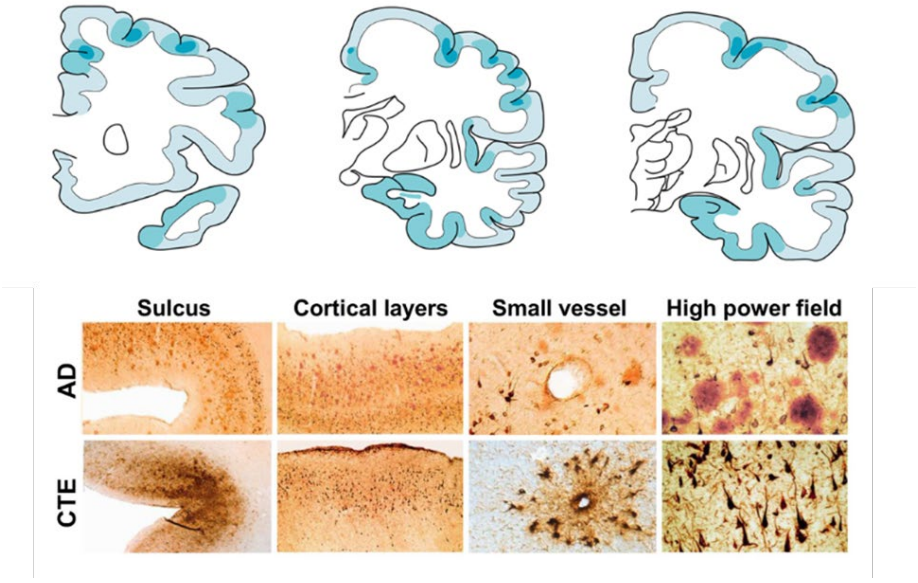

Figure 3-1: (Top) Progression of CTE[4]. Hyperphosphorylated tau plaques are found initially in the dark blue zones. As the disease progresses, the plaques are found in more disperse areas of the cerebral cortex. (Bottom) Characteristic pathology of AD and CTE[5].

By the 1980s and 1990s, breakthroughs in molecular genetics and structural biology allowed researchers to identify disease-associated aggregation-prone proteins, such as amyloid-beta, tau, alpha-synuclein, and prions. The discovery of prion diseases by Stanley Prusiner in 1982, and the realization that misfolded proteins could self-propagate, revolutionized our understanding of protein aggregation mechanisms[75]. During this time, advancements in electron microscopy and X-ray crystallography provided detailed structural models of amyloid fibrils and their pathological roles (Figure 3-1).

In the 21st century, the field has expanded rapidly with the development of single-molecule techniques, cryo-electron microscopy (cryo-EM), and computational modeling, offering unprecedented insights into aggregation kinetics and protein misfolding pathways. Research has also extended into biopharmaceuticals, where protein aggregation is a major challenge in the formulation of therapeutic antibodies and protein-based drugs[76]. Today, protein aggregation remains a key area of study, bridging fundamental molecular science with biomedical applications in neurodegenerative diseases, aging, and drug development.

Despite this wealth and history of research, the contribution that mechanical stimuli have on protein aggregation remains poorly understood. Methods to study protein aggregation under controlled strains, therefore, are needed to better understand its link to mechanical events like head injury or TBI. In this chapter, the methods and materials used to induce protein aggregation are presented. Using a combination of CFD simulation and bespoke experimental apparatuses, we were able to cause protein to aggregate by inducing extensional flow fields. These aggregates were confirmed using a variety of light scattering techniques, as well as fluorescent microscopy to confirm the molecular structures of the apparent aggregates.

3.2 Protein Properties

3.2.1 BSA

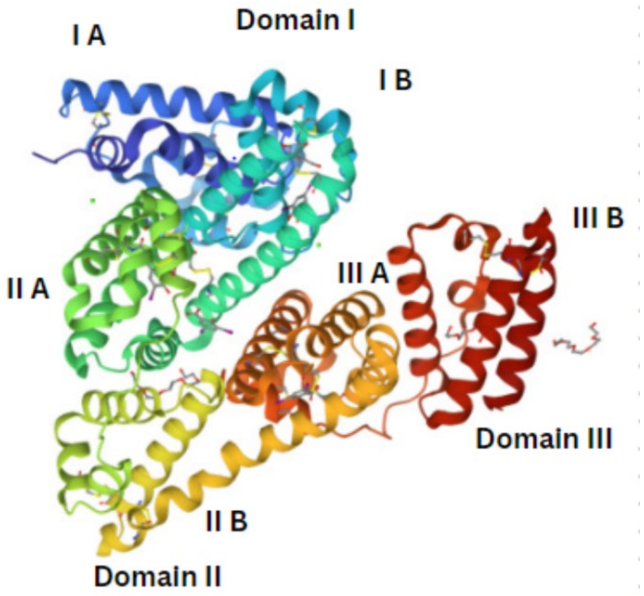

Figure 3-2: BSA molecule conformation. Secondary structures are primarily helices, and tertiary structures contain hydrophobic and hydrophilic cavities and binding sites[77].

Bovine Serum Albumin (BSA) is a globular protein commonly used in biochemical and biomedical applications due to its stability, solubility, and binding capacity. BSA is a soft, flexible protein with a dynamic structure that can undergo conformational changes in response to pH, temperature, and ionic strength. Its globular shape allows it to deform under mechanical forces while maintaining structural integrity[78] (Figure 3-2).

BSA is a single polypeptide chain of 583 amino acids and has a three-domain 3dimensional structure. These main domains are themselves divided into two subdomains, which contain hydrophobic cavities and binding sites for various molecules. The secondary structure of BSA is primarily alpha-helices, and there are no beta-sheets in the native structure (Figure 3-2)[77].

BSA and other serum albumins, often called blood albumins, bind to other molecules allowing them to be more efficiently transported in the blood and across lipid bilayers through conformational changes. This property of BSA makes it a useful molecule for transport of endogenous insoluble molecules and additionally demonstrates its potential for aiding in drug delivery. Its inherent flexibility in shape and structure therefore makes it susceptible to aggregation and gelation when exposed binding sites interact with like molecules nearby[79].

3.2.2 Tau

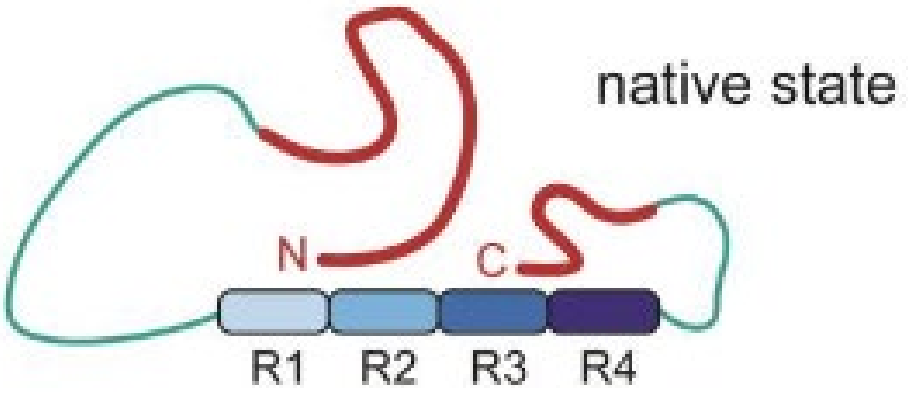

Figure 3-3:Potential native state of tau. Though tau is an IDP, it exhibits this transient "paper-clip" state[80].

Tau is a microtubule associated protein (MAP), which stabilizes microtubules within the cytoskeleton of neurons. In a healthy brain, binding tau to microtubules promotes the structure and assembly of the neuronal axon, allowing for nutrient and organelle transport along the length of the cell. When tau becomes hyper-phosphorylated, its binding affinity to the microtubule is decreased, and the structure of the neuronal cell becomes compromised (Figure 3-4).

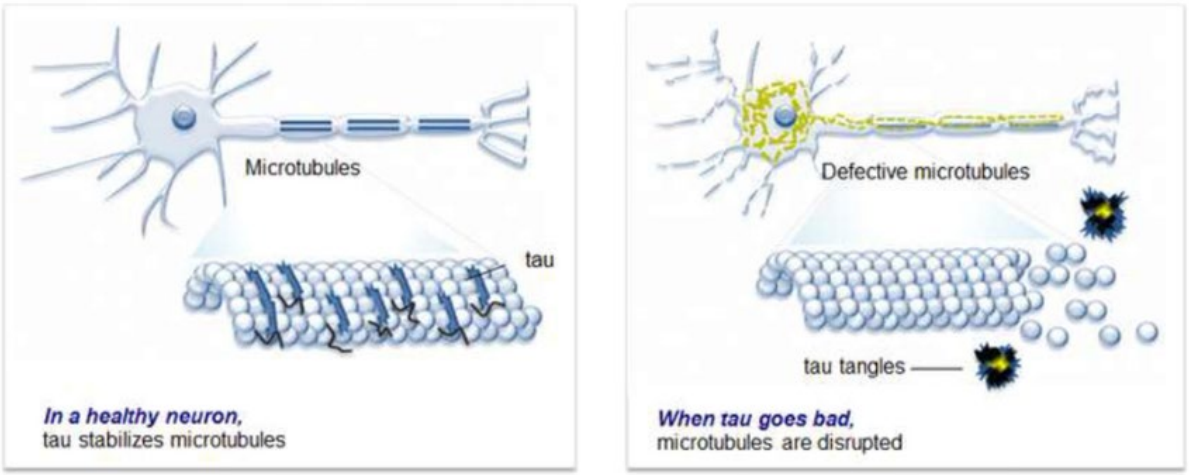

Figure 3-4: Illustration of how tau protein is observed in a healthy neuron (left), and when it becomes defective neurofibrillary tangles[12].

Tau is organized into four distinct regions, an N-terminal, a proline-rich region, a microtubule binding region (MBTR), and a C-terminal tail (Figure 3-3). The N-terminal is often called the "projection domain," which extends outward from the microtubule like an antenna, and is therefore well suited to perform communication functions like interacting with other proteins and ensuring proper spacing between microtubules[80]. The proline-rich region is involved in modulating phosphorylation, which can increase or decrease the protein's binding affinity to the microtubule[81]. The MTBR, aptly named, is the region that primarily binds to microtubules, promoting stability and proper assembly. In the MBTR can also be found aggregation-prone regions that are key in tau aggregation. The final region, the C-terminus, lacks a defined structure, but its function is not clear. However, it may further modulate microtubule and aggregation affinity[80].

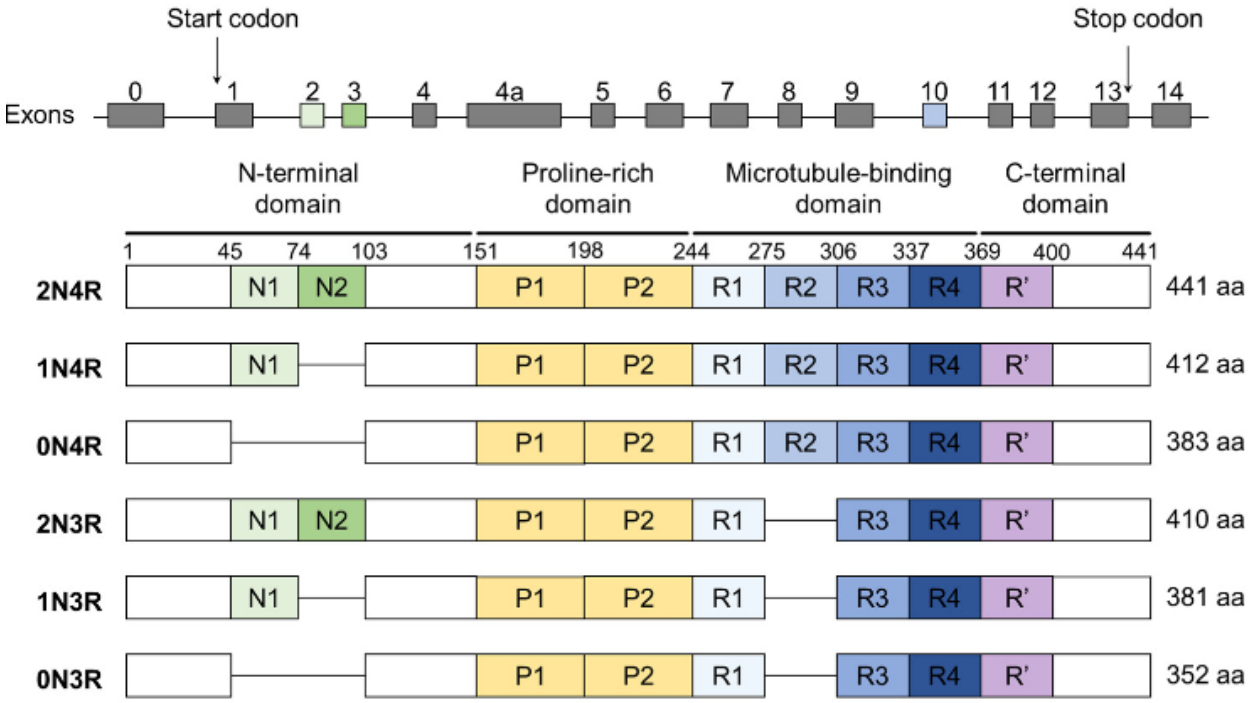

Figure 3-5: Primary structure of tau. There are 6 isoforms of tau, differentiated by the number of repeats in the N-terminal domain and microtubule binding domain[80].

There are six known isomers of tau (Figure 3-5), differentiated by the presence of 0, 1, or 2 N-terminal domains and the presence of three or four binding domains (R-domains) in the MBTR. Different isomers are associated with different diseases. For example, Pick's disease is associated with 3R tau isomers, while 4R tau isomers are associated with progressive supranuclear palsy, among others. Meanwhile, tauopathies such as Alzheimer's disease and CTE are associated with both 3R and 4R tau isomers[80].

3.3 How Do Proteins Aggregate?

The precursor to aggregation is denaturation of proteins, or when a protein unfolds from its native 3-dimensional structure. Denaturing can be achieved in several ways, most commonly by the application of heat, and can also be influenced by changes in pH balance, addition of salts, or by adding a solvent to the environment[82]. In each scenario, the additives break hydrogen bonds that keep the proteins in their characteristic form, allowing for different parts of the protein chain to be exposed to the environment and potentially interact with adjacent molecules.

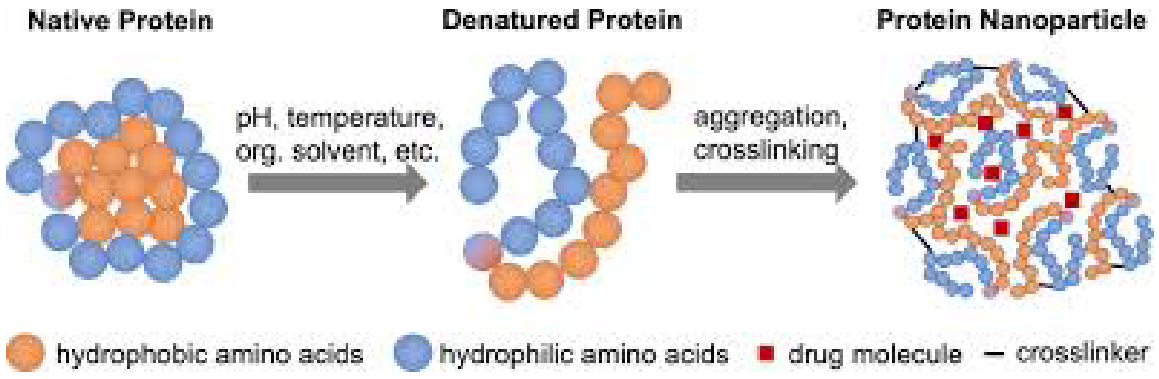

Figure 3-6: Illustration of how a protein with hydrophilic shell and hydrophobic interior may become denatured and aggregate via crosslinking[83].

Some proteins, like BSA, have a flexible globular structure. These globular proteins are water soluble, with a hydrophilic outer layer protecting the inner hydrophobic core from water[79]. These folded structures are held together by hydrogen bonds, which can become destabilized by adding heat or changing pH of the solvent. If the protein misfolds or becomes unstable, the hydrophobic regions of the protein become exposed which increases their likelihood of interacting with adjacent molecules (Figure 3-6). When this happens, hydrophobic regions of neighboring protein strands may collapse together to shield both from surrounding water[83].

While BSA aggregation is influenced by these hydrophobic-hydrophilic interactions, it is not likely that the same applies to tau protein[80]. Tau is a remarkably hydrophilic protein, lacking significant hydrophobic regions, and therefore not having a distinct 3-dimensional structure. Thus it is classified as an intrinsically disordered protein (IDP), and as such, its aggregation is not thought to be driven by these hydrophobic-hydrophilic conformational changes. The initiating event of tau aggregation remains a mystery, as aqueous tau is highly soluble and heat stable, and thus not obviously susceptible to denaturation or aggregation[80].

Due to the MTBR being immediately adjacent to the proline-rich region, the former's binding ability can be impacted by the phosphorylation of the latter. Thus, when the proline-rich region becomes excessively phosphorylated, the MBTR may lose binding ability all together, initiating potentially pathological aggregation. These microtubule-binding domains on the protein are also the sites which are most likely to interact and aggregate to other tau molecules.

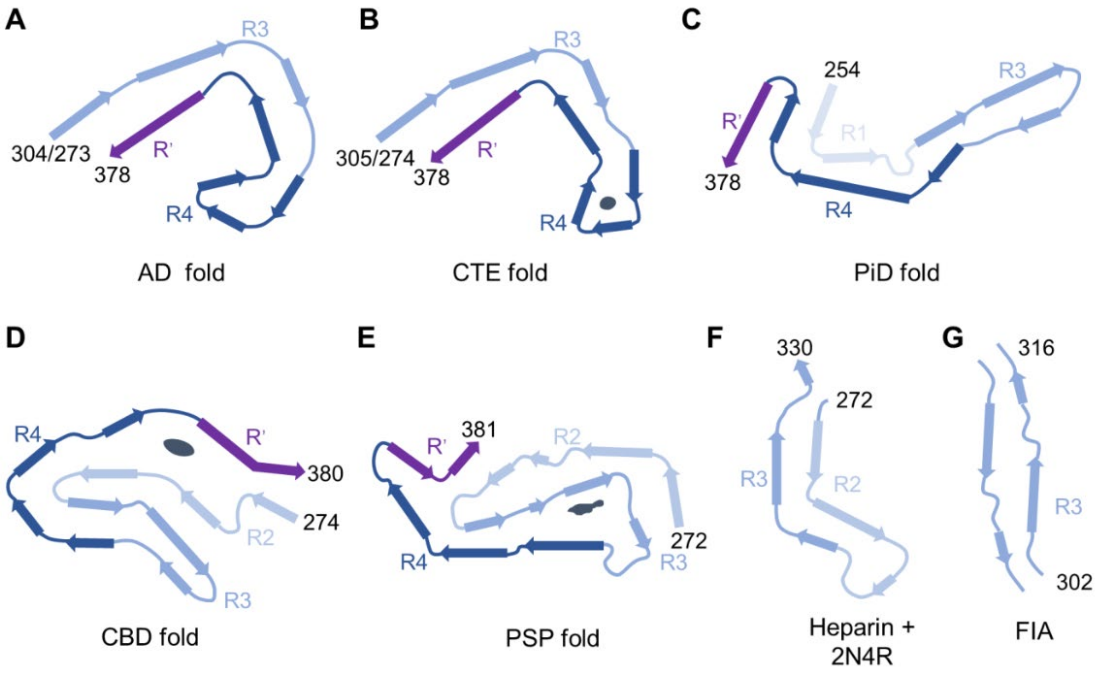

Figure 3-7: Characteristic misfolding conformations of tau associated with different diseases[80].

While tau does not have a clearly defined 3-dimensional structure, it can sometimes be found to assume a transient "paper-clip" conformation when not attached to microtubules (Figure 3-3). In diseased brains, tau assumes many different conformations, depending on the specific tau isomer and associated disease (Figure 3-7). Tau aggregation occurs in a cascade, where single molecules first join together into dimers, which then grow into oligomers, finally forming protofibrils and fibrils as the aggregation continues (Figure 3-8).

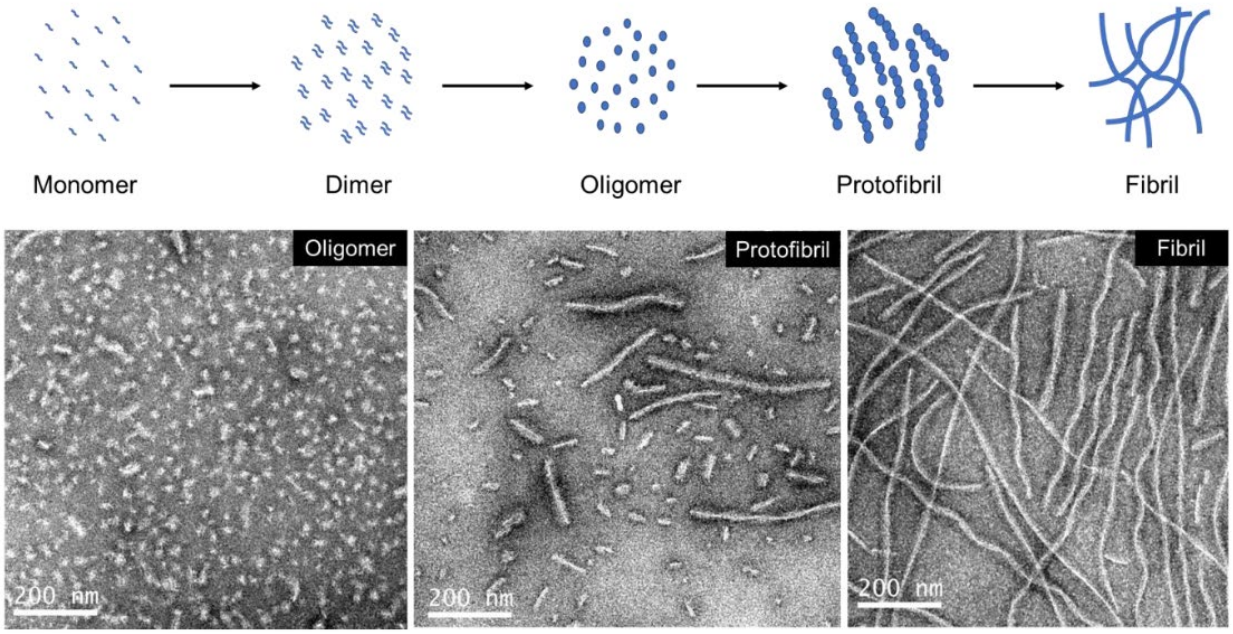

Figure 3-8: Progression of tau oligomerization and fibrillization[80].

3.4 CFD Simulations

Computational Fluid Dynamics (CFD) simulations were conducted using Comsol Multiphysics software. In this section, the methods used to simulate the experimental extensional flow fields are presented.

3.4.1 CFD Extensional Flow

As mentioned in previous chapters, extensional flow is characterized by a fluid field where a velocity gradient exists parallel to the direction of the flow. The simplest method to induce an extensional flow field, therefore is to simply change the in-line cross-sectional area of the flow channel in the flow direction. Thus, by the conservation of mass principle, the velocity of the fluid flow will change along with the cross-sectional area, creating the flow-wise velocity gradient that is desired. A gradual change in cross-sectional area will create a similarly gradual change in

velocity, while a sudden change will results in an abrupt change in velocity. Thus, the extensional flow field strength can also be determined by the rate of change of cross sectional area.

3.4.2 Analytical Solution

To measure the extensional rate analytically, a simple flow can be analyzed using basic control volume analysis of a channel comprising two cylindrical sections of different diameters.

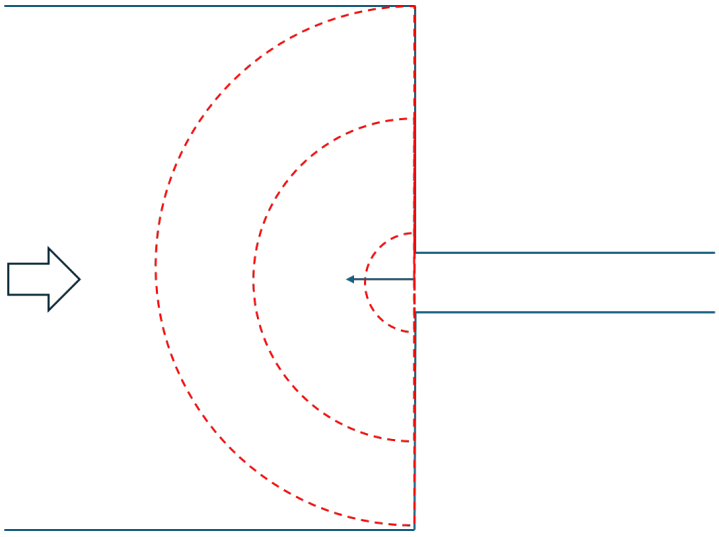

Figure 3-9: 2-dimensional axisymmetric control volume analysis. The control surfaces are modeled as hemispherical inlets on the left and a circular cross-sectional area outlet on the right.

By establishing a hemispherical control volume around the entrance to the smaller channel, mass flow can be measured into and out of this CV (Figure 3-9), and an analytical solution for extensional strain rate can be derived. Varying the radius of the hemispherical CV, the resultant midline velocity increases as the radius decreases, i.e. as the CV boundaries approach the small channel entrance. Thus, a relationship between mid-line velocity and distance from entrance can

be derived. By taking the derivative of this relationship with respect to the distance from the entrance, the location and magnitude of maximum extensional strainrate can also be determined.

$$V_{avg} = V_{cap}\frac{r_{cap}^2}{2r^2} \tag{3.1}$$

$$\frac{dV}{dr} = -V_{cap}\frac{r_{cap}^2}{r^3} \tag{3.2}$$

$$V_{cap} = V_{in}\frac{r_{in}^2}{r_{cap}^2} \tag{3.3}$$

For the locations very near the entrance of the smaller channel, a CV can be established in which the inlet surface is a spherical cap instead of a hemisphere (Figure 3-10). A similar analysis can be performed to find the magnitude and location of the extensional rates in this section.

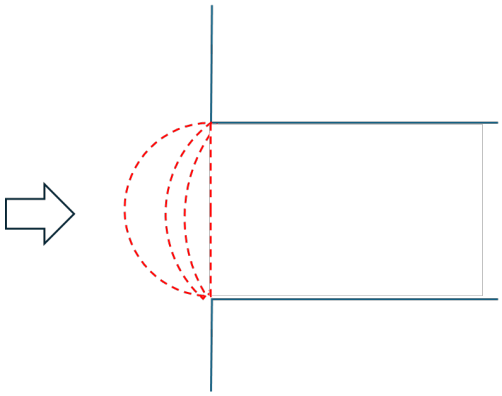

Figure 3-10: Control volume analysis close to the entrance of the capillary. Here, a hemispherical control surface is replaced by a spherical cap inlet control surface, while the outlet circular cross section remains the same.

$$V = V_{cap}\frac{r_{cap}^2}{r_{cap}^2 + r^2} \tag{3.4}$$

$$\frac{dV}{dr} = -2V_{cap}\frac{r_{cap}^2}{\left(r_{cap}^2 + r^2\right)^2} \tag{3.5}$$

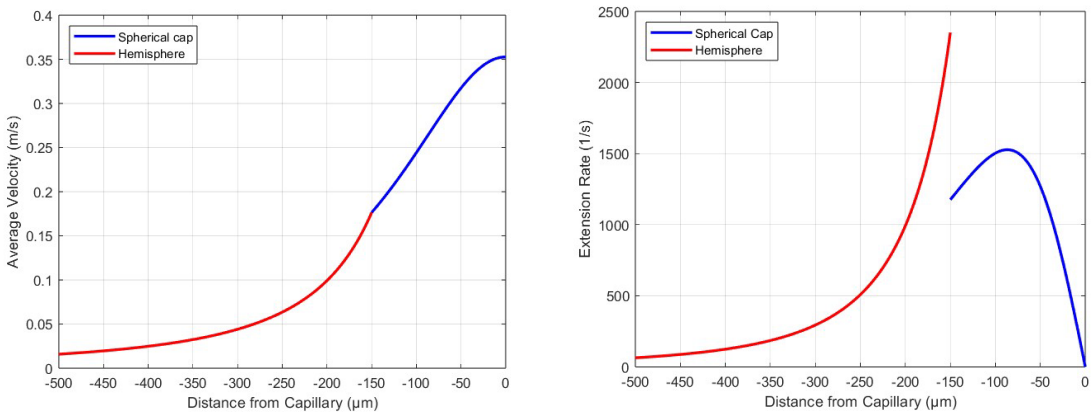

Figure 3-11: (Left) Calculation of average velocity as a function of distance from the capillary for the hemispherical CV (red) and the spherical cap CV (blue). (Right) Calculation of the derivative of velocity with respect to distance from capillary for the hemispherical and spherical cap CVs.

Comparing these CV analyses (Figure 3-11), it can be estimated that the maximum extensional rate occurs one radius away from the entrance to the smaller channel, and thus the magnitude of the maximum extensional rate can be defined.

$$\dot{\varepsilon}_{max} = \frac{dV}{dr}_{max} \tag{3.6}$$

$$\dot{\varepsilon}_{max} = V_{in}\frac{r_{in}^2}{r_{cap}^3} \tag{3.7}$$

3.4.3 Comparison to CFD

To simulate the reciprocal syringe drive, CFD simulations were created as 2D axisymmetric stationary systems (Figure 3-12). The inlet was set as a velocity boundary condition, to simulate the plunger moving inward towards the capillary. Upon solving the CFD simulation, the spatial

derivative of the midline velocity was calculated, measuring the extensional strainrate along the midline.

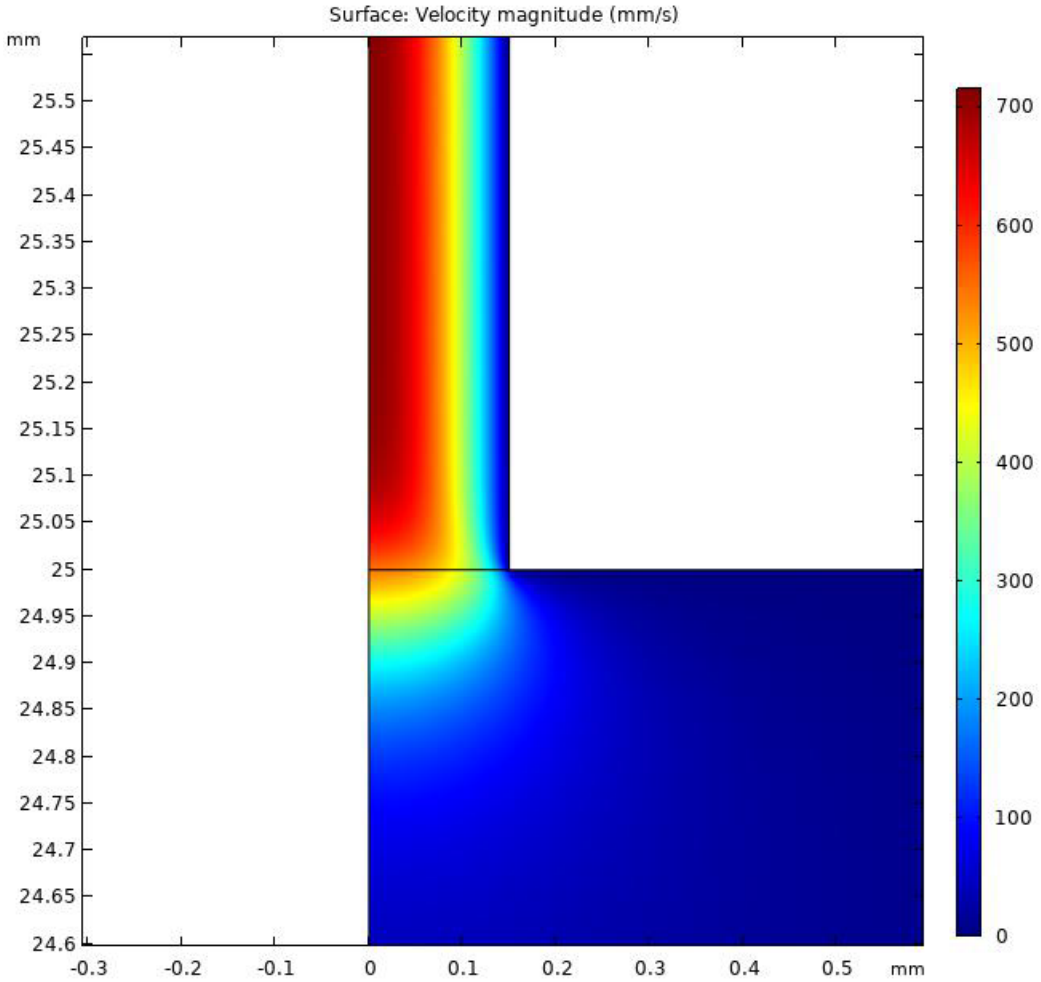

Figure 3-12: CFD results of a 2D axisymmetric simulation of a large diameter channel flowing into a small capillary. Note that the exit field of the flow accelerates within one radius away from the capillary, as calculated in the analytical CV analysis.

The analytical solution and the CFD simulation matched quite well, with a similar order of magnitude maximum strainrate which occurs approximately one capillary radius (0.15mm) away from the entrance (Figure 3-12). Analytically, an input velocity of 1.5 mm/s flowing from a 4.6 mm diameter syringe into a 0.3 mm diameter capillary results in a maximum extensional rate of

2351 s^{-1}. An input velocity of 1.5 mm/s results in an extensional strain rate of 2880 s^{-1} in the CFD simulation (Figure 3-13). The analytical solution underestimates the real maximum extensional rate, based on the assumption that a hemispherical control-volume would have a uniform inlet and outlet control volume. In reality, due to boundary effects at the inlet and outlet, the midline velocity would be higher than the average, and thus the extensional rate would be higher here as well.

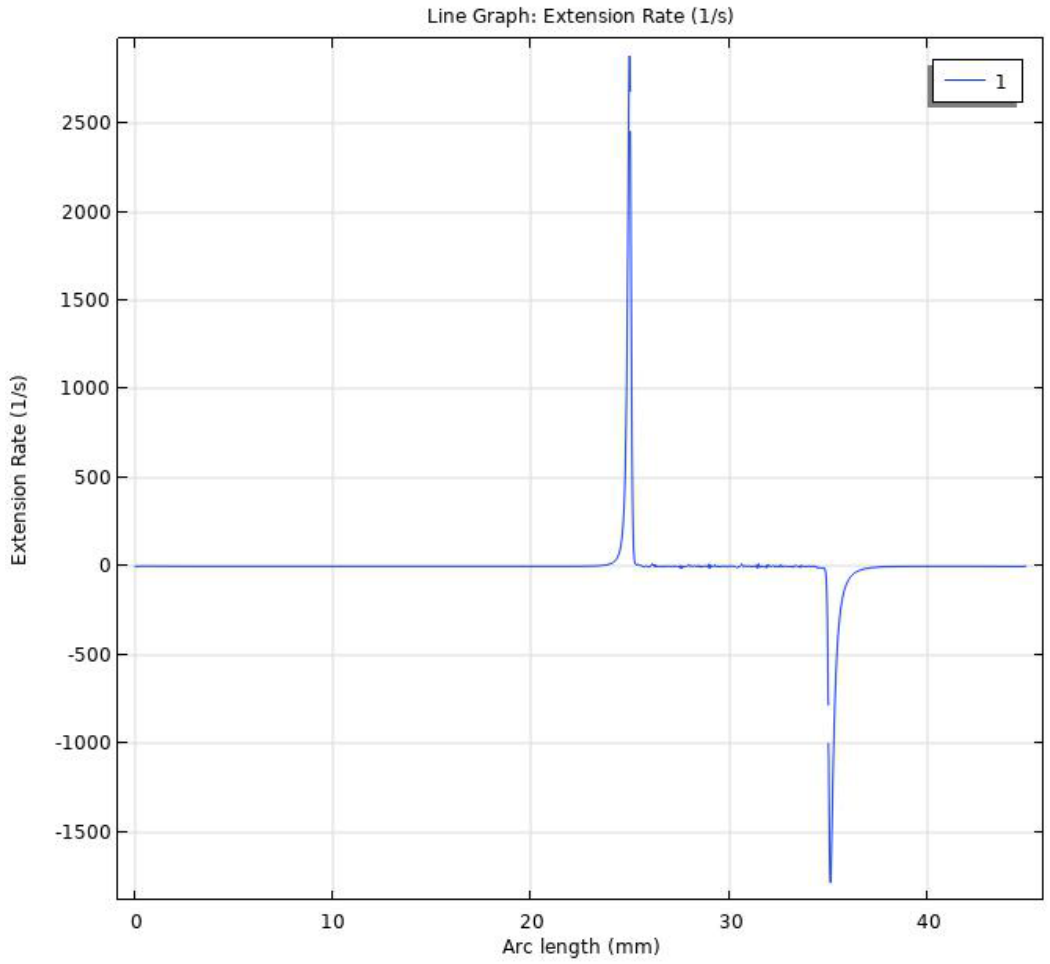

Figure 3-13: Extensional rate calculation along midline of syringe and capillary. As the fluid flows from left to right, the maximum extensional rate occurs one radius away from the capillary and matches well with the analytical solution.

3.5 Reciprocal Extensor

To achieve variable and controlled extensional rates, a reciprocal syringe drive was built (Figure 3-14). This syringe drive achieved extensional rates by flowing the sample back and forth between a relatively large channel in the syringe body and a small glass capillary. On each pass, the sample is subjected to an extensional rate as it flows from the larger bore to the smaller diameter capillary. By varying the capillary size, plunger speed, and iteration of passes, we achieve different extensional rates to study its impact on aggregation behavior.

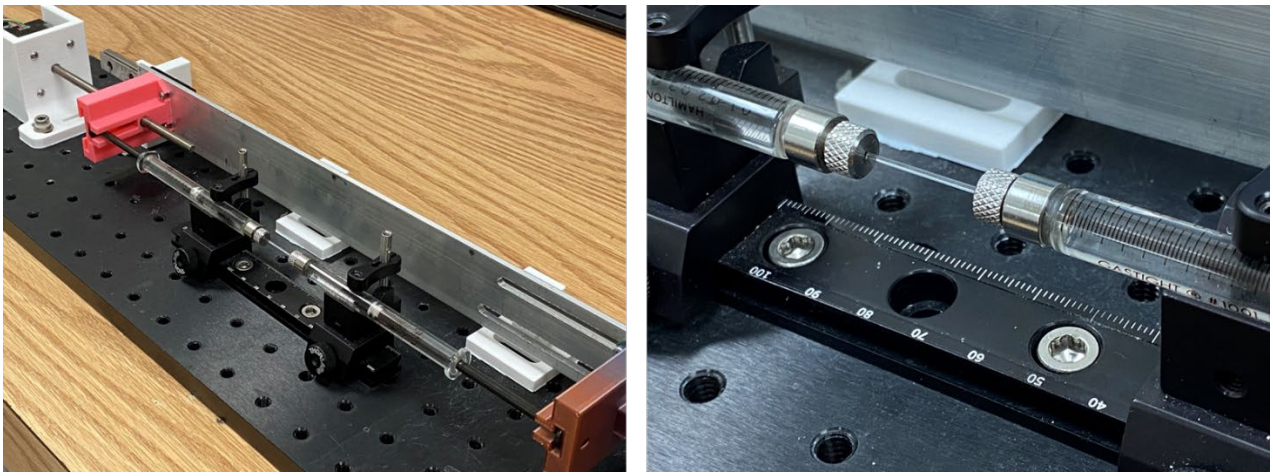

Figure 3-14: Reciprocal Extensor. Two syringes with inner diameters of 4.6mm (left) are connected by capillary of inner diameter of 0.3mm (right). Stepper motor drives plungers back and forth, which are rigidly connected by an aluminum plate on a linear track.

3.5.1 Dobson

The extensor built for this experiment was modeled after the one built by Dobson et al (2017). In their work, the team built an extensor that achieved extensional rates exceeding 11,000 1/s. Using these elevated extensional rates, they were able to produce robust and repeatable aggregates with a variety of proteins[20]. These extensional rates, however, far exceed physiological values, and so an apparatus that was optimized for slower plunger velocities, and thus lower extensional rates,

was desired to more closely mimic protein aggregation that may result from pathologically relevant stimuli.

3.5.2 Stepper Motors

To operate the reciprocal extensor, we chose to use a stepper motor linear actuator (Haydon Kerk Pittman, Waterbury, Connecticut, USA). This was chosen for its ability to provide precise stroke lengths and velocities. However, stepper motors are only able to provide a limited amount of torque, depending on the stroke speed. They are also limited in velocity, as lower velocities become less smooth. Thus, we built an extensor in which a linear actuator made of a stepper motor could be easily swapped out in order to provide consistent and smooth operation over a range of plunger velocities.

3.5.3 Syringes

As vessels for the protein solution, we chose Hamilton 1ml gas-tight syringes (1000 Series, Hamilton Company, Reno, Nevada, USA). These have an inner bore of 4.6mm and can accommodate capillaries with outer diameters of 1mm. Thus the chosen capillaries, having an inner diameter of 0.3mm represent an approximately 15x diameter reduction and 225x area reduction, resulting in a velocity increase of 225x within the capillary.

3.5.4 Driving Program

To control the reciprocal extensor, we used an Arduino Uno and developed a script to run the apparatus at a specified speed, stroke length, and number of iterations. This recipe could be altered to accurately produce desired extensional rates and durations for this test.

3.6 Measurement Methods

3.6.1 Light Scattering

To measure the aggregates that form during these processes, methods are needed to measure the effective hydrodynamic diameter of the aggregates and to count the number of aggregates that form during the process. To do so, a variety of light scattering techniques can be used. In this section, two light scattering techniques that were used in this study will be presented. Light scattering techniques are performed by measuring the amount of light from a source is scattered by a particle. The particles will move due to Brownian motion, thus causing a disturbance in the light over a finite time. This fluctuation frequency is proportional to the size of the particle, since, by the Stokes-Einstein equation, smaller particles have faster Brownian motion than larger particles[84].

$$D(r) = \frac{k_B T}{6\pi\eta r} \tag{3.8}$$

Dynamic Light Scattering (DLS)

DLS is a method in which a laser is shone through a solution with suspended particles (Figure 3-15). Each particle scatters light in all directions, which in turn either constructively or destructively interferes with the scattered light from neighboring particles. This creates a speckled pattern of varied intensity in space, downfield of the laser. Measurements of intensity of the speckled pattern are taken at precise intervals and correlated together over time[85].

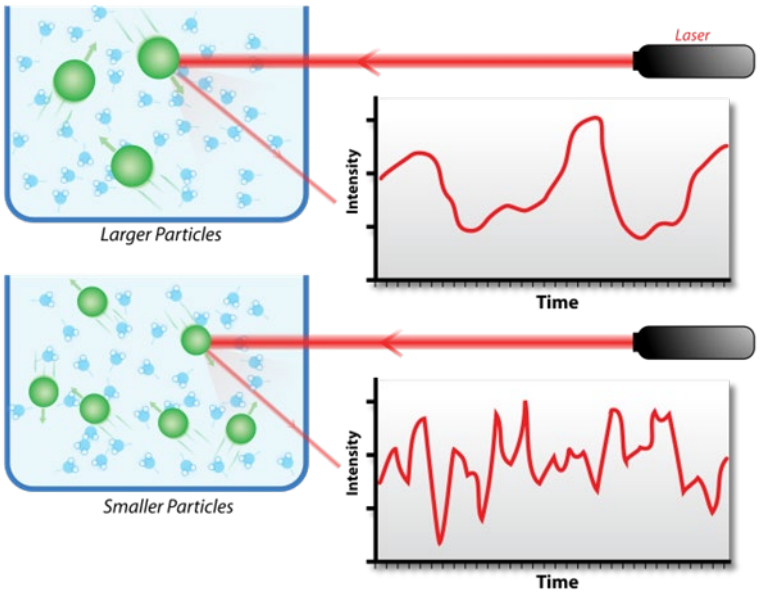

Figure 3-15: Schematic of operation of DLS and how the measurements differ between large particles and small particles. Fluctuations in readings occur at higher frequency when the measured particles are smaller, due to Brownian motion[86].

Over time, these measurements produce a correlation curve, measuring how similar speckle patterns are to each other over a time interval. At very short time intervals, particles do not have much time to move, and thus the correlation between these patterns is relatively high. At longer intervals, the correlation decreases, as particles have time to move and thus change the scattered light speckle pattern (Figure 3-16).

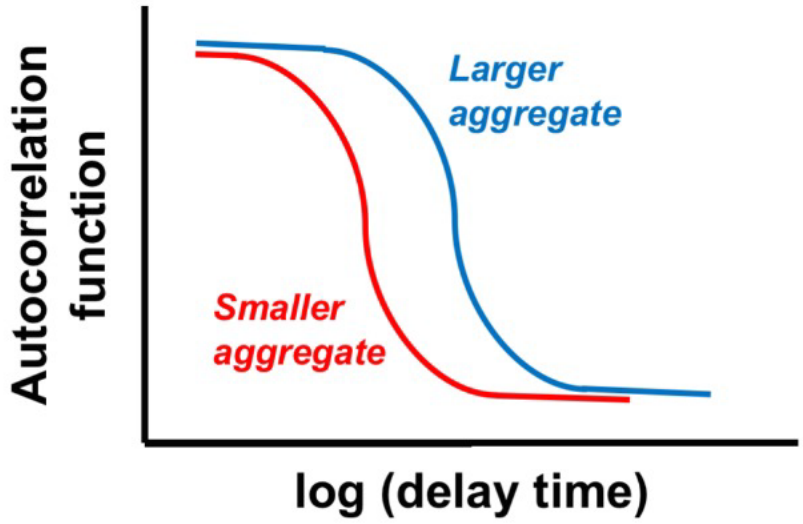

Figure 3-16: Illustration of how DLS differentiates between smaller and larger aggregates using an autocorrelation function. For larger aggregates, the decay is slower than for smaller aggregates[87].

Information about the size of the particles is captured in the exponential decay of the correlation curve. The correlation curve can be indirectly interpreted as the time a particle needs to move away from its particular position. If a particle is moving quickly, then the time needed is short and the decay of the correlation curve is correspondingly quick. If a particle moves more slowly, the decay of the correlation curve is relatively long. Thus, smaller particles, which exhibit faster Brownian motion, will exhibit correlation curves with fast exponential decays, while larger particles will have correlation curves with slower decays[87].

Nanoparticle Tracking Analysis (NTA)

NTA uses a similar method as DLS to measure the size of particles in a suspension (Figure 3-17). Light scattering is similarly measured using a laser and the Brownian motion of the particles reveal their hydrodynamic diameters with the Stokes-Einstein equation. Where NTA differs, however, is that using a microscope camera lens, individual particles can be captured and counted.

Thus, precise information not only of size but also distribution of particles of varying size can be measured[88].

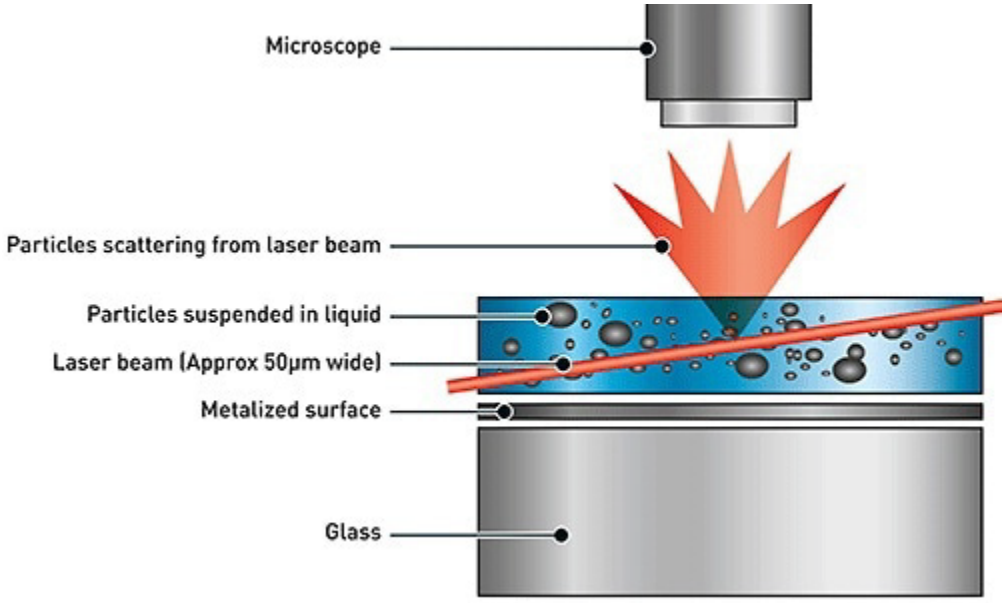

Figure 3-17: NTA schematic showing the combination of light scattering techniques used in DLS in addition to the visual measurement performed using the microscope lens[89].

In NTA, the laser is used to illuminate particles, whose movement is captured over multiple frames of video recording. NTA programs identify individual particles and track their movement across the video frames, measuring their Brownian motion, thus determining their size. NTA systems will often mix the solution throughout testing to measure particles in different locations within the suspension (Figure 3-18). Several of these videos are captured and the size and number of particles captured in the videos is analyzed and presented as a distribution[90].

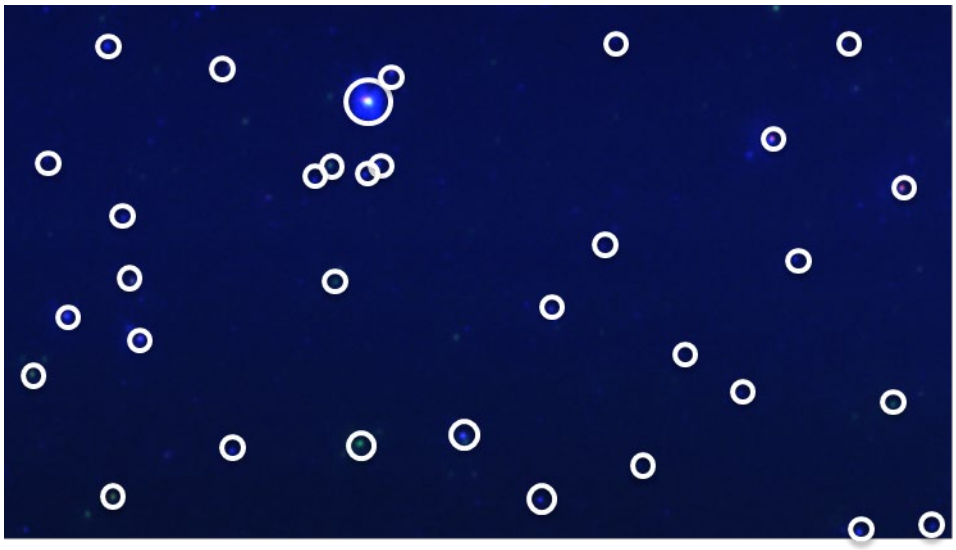

Figure 3-18: Representative NTA result. Particles are identified by the software, counted, measured, and tracked.

3.6.2 Fluorescent Microscopy

One weakness for light scattering techniques is the limit of hydrodynamic diameters that can be measured. For particles that are much greater than 500 nm, sedimentary motion, driven by gravity, dominates Brownian motion, and thus cannot be measured using DLS nor NTA. Therefore, a technique is required to analyze aggregate particles that exceed the limitations of DLS and NTA. In this study, we used fluorescent microscopy to analyze particles that were too formed during testing but are too large to capture in DLS or NTA.

Amyloid Fibrils

Amyloid formations are highly ordered protein aggregates characterized by their fibrillar morphology, cross-β sheet structure, and resistance to degradation (Figure 3-19). They arise when normally soluble proteins misfold and self-assemble into long, insoluble fibrils. The process of amyloid formation typically begins with nucleation, where misfolded monomeric proteins form

small, unstable oligomers. Once a stable nucleus forms, fibril elongation proceeds rapidly as additional protein monomers add to the growing fibril ends. These fibrils are stabilized by extensive hydrogen bonding along the backbone, giving rise to a cross-β sheet architecture, where β-strands run perpendicular to the fibril axis. This unique structure is detectable by Congo red staining, Thioflavin T fluorescence, and electron microscopy[91,92].

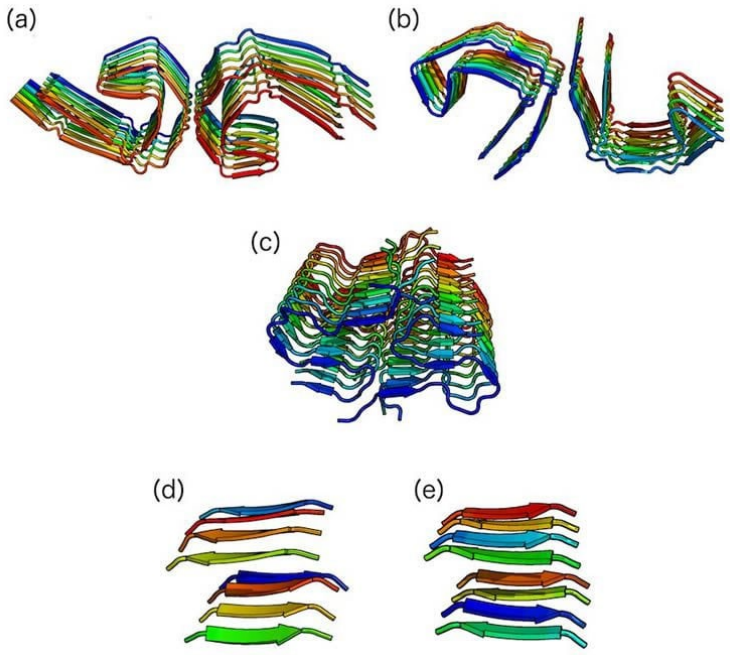

Figure 3-19: Illustration of tau aggregation and beta sheet formation [93]. (a and b) Misfolded tau proteins align and binding domains across molecules interact. (c) Aggregated proteins continue to misfold, and other parts of molecule become entangled. (d and e) Portions of overlapping proteins align into beta-sheets.

Thioflavin T (ThT)

Fluorescent microscopy works by staining a fluid with a fluorescent dye. When excited by a photon of a certain wavelength, the photon is reemitted by the dye at a different wavelength. All other wavelengths are absorbed. ThT is a dye that is used to detect amyloid structures in aggregated proteins. Normally in solution, ThT exhibits minimal fluorescence. Amyloid fibrils have grooves along their surfaces that have high affinity for ThT binding. When the dye binds to the surfaces of

the β-sheet structures of amyloid fibrils, its fluorescence is enhanced, which allows for the presence of these sheets to be detected using fluorescent microscopy[94,95]. When excited with a wavelength between 450-460nm, ThT emits a photon which peaks in intensity at approximately 480nm. Using a Nikon eCFP filter cube (Figure 3-20), ThT stained amyloid fibrils can be observed with the Nikon microscope. With the reduced intensity from the fluorescent filter, a longer exposure time is needed, but amyloids can be observed clearly with this method.

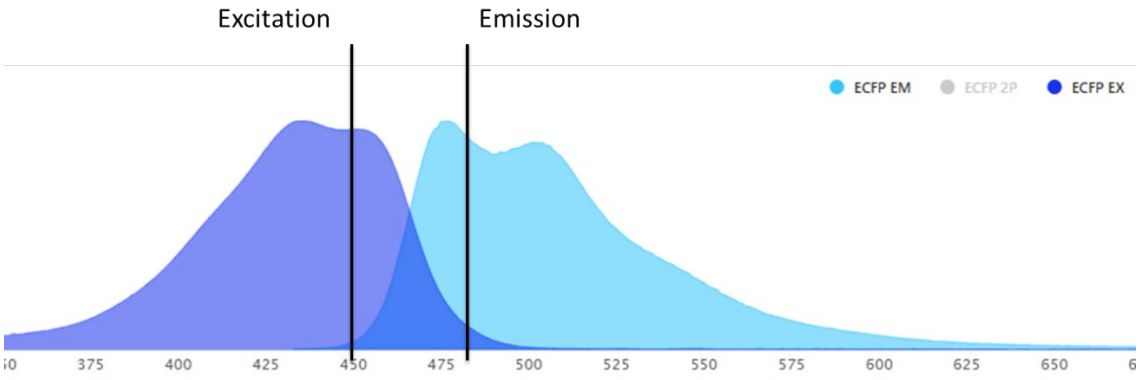

Figure 3-20: Excitation and emission of ECFP protein, as reference for the Nikon ECFP filter cube[96].

3.7 Summary

Protein aggregation remains an important topic of research due to its impact on industrial as well as biological processes. However, considering protein aggregation as a mechanical process remains an understudied field but has the potential to reveal important characteristics of neurodegenerative diseases. In this chapter, the methods used to induce and measure protein aggregation were presented. Through CFD simulation, in-vitro experiments, and light scattering analysis, we can further define a framework in which the aggregation behavior of proteins as a result of mechanical stimulus can be characterized. Thus we can begin to quantify how the magnitude and duration of flow fields contribute to protein aggregation. While the full picture of

protein aggregation in the brain remains a mystery, the experimental framework presented here and in chapter 2 may offer a starting point to more fundamentally understand the physiological processes that lead to the generation and progression of neurodegenerative diseases like CTE and Alzheimer's.

Chapter 4 : Vitreous Extensional Rheology – Demonstration of Extensional Rheology Technique on small volume Biological Fluid

4.1 Introduction

As discussed in Chapter 2, there is a rich history of extensional rheology, both practically and academically. However, its application to biomedical processes remains an underexplored field, yet has the potential to have enormous impact on the health outcomes of medical procedures. In this chapter, a demonstration of an extensional rheological technique is presented, where the efficacy of different surgical tools are assessed using novel microextensional rheology. This work was conducted in collaboration with the UCLA Jules Stein Institute Ophthalmology Department.

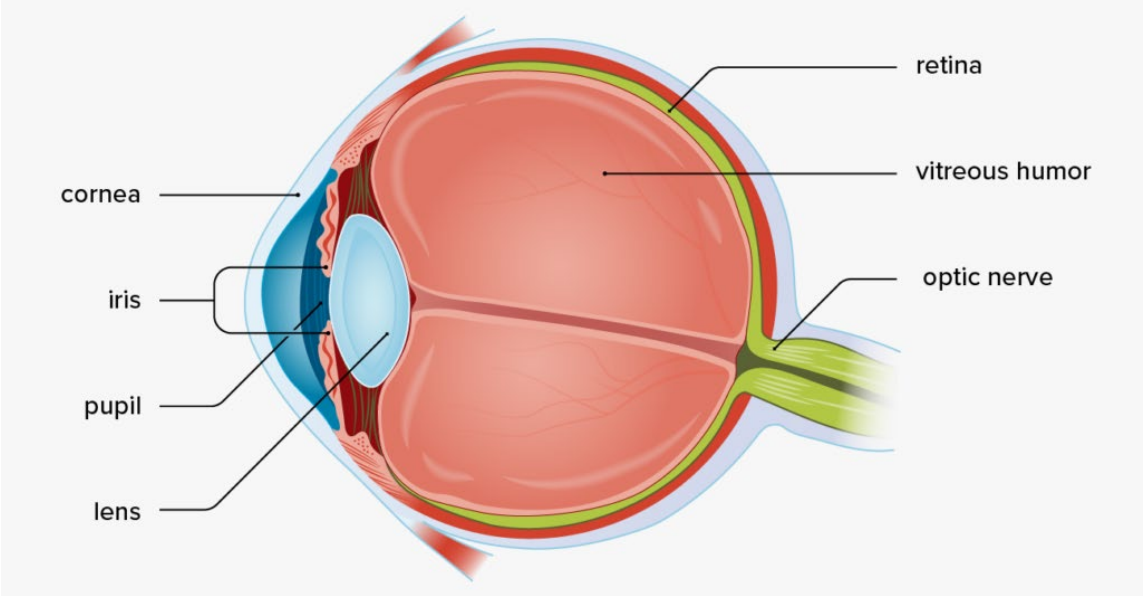

Figure 4-1: Anatomy of human eye[97]

Vitreous humor is a clear, gel-like substance that fills the space between the lens and the retina in the posterior chamber of the eye (Figure 4-1). It composes approximately 80% of the total eye volume, helping to maintain it's spherical shape and internal pressure. Because of its location in the eye, it must be optically clear, being composed of 98-99% water as well as a matrix of type-II collagen fibers and hyaluronic acid. Healthy vitreous behaves as a viscoelastic gel, which serves to maintain stability and provide shock absorption. Overtime and in unique circumstances, however, vitreous can liquify and behave as a viscoelastic fluid, either due to aging, disease, or in instances of surgery.

4.2 Motivation

Vitrectomy, or the surgical removal of vitreous, is a required step in most vitreo-retinal surgical procedures. Vitreous is a transparent gel-like substance found between the lens capsule and retina. It is composed of an inflated and highly hydrated collagen matrix with 99 wt.% water, 0.9 wt.% salts, and less than 0.1 wt.% collagen and hyaluronic acid[98,99]. Vitreous is related to various functions including maintaining transparency, protecting the retina from trauma, and other metabolic requirements[100]. Due to the highly connected matrix of collagen fibers, vitreous removal can cause traction in areas of localized retinal adhesion[101]. Thus, vitrectomy must temper extraction speed with the cutting action to maintain retina safety[102].

Conventional pneumatic blade (PB) cutters use a "guillotine-style" cutter to aspirate vitreous out of the eye (Figure 4-2). These cutters aspirate vitreous into the needle and then cut. This action creates traction where the retina may be pulled due to the aspiration forces[101]. Ultrasonic (HS) cutters, on the other hand, employ a 100% open port design that continuously shears and aspirates

the vitreous. Ultrasonic energy is transmitted from the device's transducer to the needle probe. The port, located at the side of the needle near the distal end, vibrates at ultrasonic frequencies enabling focused tissue cutting capabilities by the port walls[103–105]. The two cutting technologies change the mechanical properties of the vitreous by breaking down the long collagen fibrils responsible for the mechanical properties of the gel-like vitreous[106]. The PB cutter mechanism employs a series of discrete cutting steps where intact vitreous is aspirated and sheared at low relative speeds. Because the US mechanism allows for continuous, smooth aspiration of vitreous, less vitreous traction occurs with US cutters than PB cutters[107].

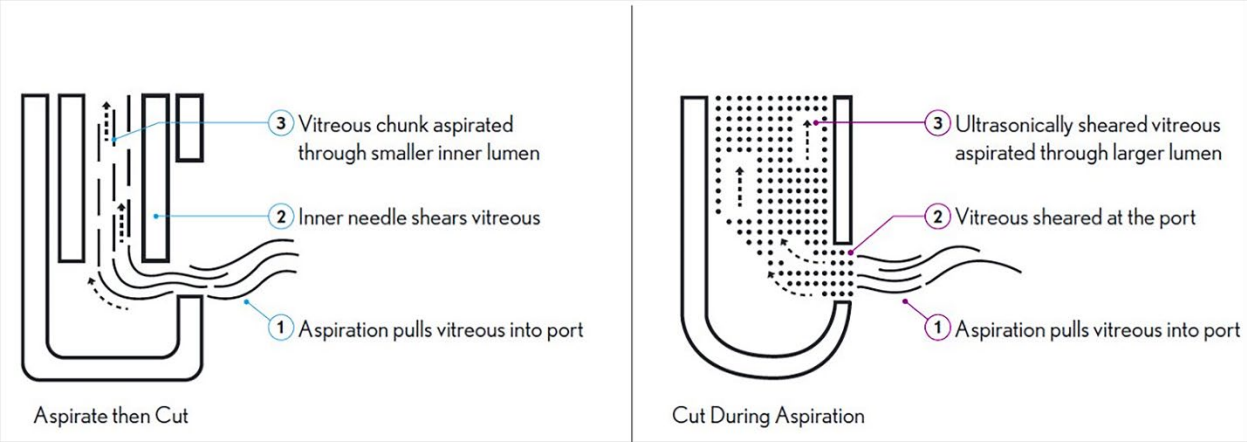

Figure 4-2: Comparison of pneumatic and ultrasonic mechanisms of action. (Left) Conventional pneumatic mechanisms aspirate intact vitreous and use inner needle blade to shear the tissue inside the needle lumen. (Right) Ultrasonic mechanisms shear the vitreous at port entrance, aspirating only ultrasonically sheared tissue. Figure courtesy of Bausch & Lomb.

Rheological study of the vitreous dates back to Lee and colleagues in 1992[108–110]. Extensional rheology is a growing field where the properties of fluids are analyzed as they are subjected to extensional strain rather than the more typical shear strain[111]. There are many applications where extensional strains are important, especially with biological materials like surgically extracted vitreous[112–115]. The cross-linking and molecular interaction of polymers and proteins in solution

cause fluids to exhibit non-Newtonian behaviors in extensional flow[20,116]. These effects, however, cannot be identified with shear rheology[66]. Therefore, performance assessment of vitrectomy technology using extensional rheology is ideal since extracted vitreous can be considered a non-Newtonian fluid containing dispersed collagen fibrils.

Extensional behavior of protein solutions is characterized by the formation of fluid structures where elastic protein interactions dominate the fluid flow[117]. Lower molecular weight solutions exhibit relatively weak protein interaction, and purely Newtonian solutions such as water and saline solution show no interaction at all[66]. It is hypothesized and observed that the US mechanism of action breaks collagen fibrils into much smaller fragments compared to the PB cutters[118]. The purpose of this study is to quantify the extensional behavior of chopped vitreous and assess the mechanism of action of US vitreous cutters by comparing their performance to conventional PB cutters. To our knowledge, this is a first attempt at quantifying surgically extracted vitreous properties using extensional rheology technology.

4.3 Methods

4.3.1 Vitreous Extraction

Pig vitreous was used as a tissue analog for human vitreous, extracted from eyes using two different vitreous cutters: a PB cutter (BiBlade, Bausch & Lomb, St. Louis, USA) and a US cutter (Vitesse, Bausch & Lomb, St. Louis, USA). Freshly harvested, unscalded, enucleated pig eyes were purchased from Sierra Medical Supplies (Whittier, CA). Preparation of each eye was performed under a surgical microscope (M840, Leica Microsystems, GmbH, Wetzlar, Germany). Eyes were acquired within 24 hours postmortem, and the tests were performed within 8 hours of

receipt and 4 hours post-vitrectomy to ensure consistency in results. All eyes were stored at 4°C prior to the experiments.

The eyes underwent an open-sky pars plana vitrectomy while secured to a custom polystyrene holder. The procedures were conducted using the Bausch & Lomb (B&L) Stellaris PC Vision Enhancement System with hardware and software modifications to provide ultrasonic vitrectomy drive capability (Bausch & Lomb, St. Louis, USA). A trocar was placed temporally 4 mm behind the limbus followed by a temporal corneal incision created with a 2.8 mm keratome blade. Surgical ophthalmic scissors were then used to remove the cornea by cutting through the corneal incision and following the edge of the corneoscleral limbus. Then the lens was squeezed out of the eye in one whole piece and the capsule was removed. Minimal iris manipulation was attempted to avoid contaminating the subsequent vitreous samples with pigment or other tissue fragments. Each probe was introduced via the pre-placed trocar to perform the vitrectomy and collect the undiluted chopped vitreous samples into sterile 'BD Vacutainer Glass Serum' Tubes (16 x 100 mm, 10.0 mL- no additives- Becton Dickson and Company, Franklin Lakes NJ) using a vitreous trap technique[119]. This technique was first described by Dr. Susan M. Malinowski in 2010, and it allows the surgeon to obtain an undiluted vitreous sample with aspiration in a controlled way, as well as diminishing the risk of contamination and providing a safe means to transfer[119]. Special attention was paid to avoid contaminating the samples with pigment from the retina or the iris, and to avoid touching areas of detached mobile retina with the cutters. For this purpose, the vitrectomy was focused on the central vitreous rather than vitreous close to the retina or iris. Two samples were taken from each pig eye.

The dual-action 23- and 25-gauge PB probes were tested at 100, 300, and 600 mmHg and at 15,000 cuts per minute (cpm). 23- and 25-gauge US probes were tested at 60 μm stroke and at 100

and 300 mmHg vacuum setting. Flowrate is the factor that determines the vitreous fragment size at a given cut rate. Due to the US cutter's open smaller port design and larger inner needle lumen, the flowrate at 300 mmHg is comparable to the upper limit of the PB cutter achieved at 600 mmHg (internal communication). Furthermore, the US cutter is not used in surgeries above 250 mmHg. Therefore, conducting this experiment with US probes at usable vacuum ranges and comparable port flowrates was found to be adequate. The US cut rate is nominally 38 kHz and 41 kHz for the 23- and 25-gauge needles, respectively. Considering one cycle to be equivalent to one cut, these cutter frequencies correspond to cut rates of more than 2 million cpm for the US cutters.

4.3.2 Micro-Extensional Rheology

To analyze the extensional rheological properties of small samples, we adapted a simple rheometric method (described in Chapter 2) to apply a large strain rate to very small sample volumes[120]. Sample volumes were typically between 50-100 microliters. Each was dispensed onto a hydrophobically treated substrate to create a domed droplet. Using a KRUSS tensiometer (K-100, KRUSS GmbH, Hamburg, Germany) in the Surface Tension setting, each sample droplet was penetrated with a 1mm diameter platinum rod. The probe penetrated 0.5mm into each sample. The probe was then quickly removed, so that the surface of the sample was perturbed upward. Each sample was tested independently three times. Testing was performed at room temperature, but each sample was kept at 4°C prior to testing.

4.4 Results

36 vitreous samples were successfully extracted from 20 pig eyes (2 samples per eye). 12 samples were tested after extraction with the US cutter. 24 samples were tested after extraction with the PB cutter (Table 4-1).

Table 4-1: Summary of cutter configuration and resultant extensional relaxation times in milliseconds

Vitrectomy Method				λ_E (ms)	
	Number of samples	Cutter Size (gauge)	Vacuum Pressure (mmHg)	Mean	Stdev
Ultrasonic	3	23	100	0.17	0.10
	3	23	300	0.39	0.10
	3	25	100	0.13	0.06
	3	25	300	2.34	2.46
(Total)	(12)			(0.37)	(1.50)
Pneumatic Blade	4	23	100	25.79	12.95
	4	23	300	24.17	15.33
	4	23	600	37.63	21.17
	4	25	100	19.11	8.47
	4	25	300	23.47	12.41
	4	25	600	33.33	11.56
(Total)	(24)			(27.25)	(15.08)

The extensional rheology behavior varied dramatically between the US and PB cutter vitreous samples (Figure 4-3, Figure 4-4). The liquid bridge that forms between the two surfaces devolved in a few milliseconds with the US samples (Figure 4-3b). Qualitatively, this behavior is similar to balanced saline solution (BSS), a Newtonian fluid which contains no protein, and therefore does not exhibit elasto-capillary behavior[121] (Figure 4-3a). The liquid bridge of the PB samples, on the other hand, persisted for more than 100 ms (Figure 4-3c).

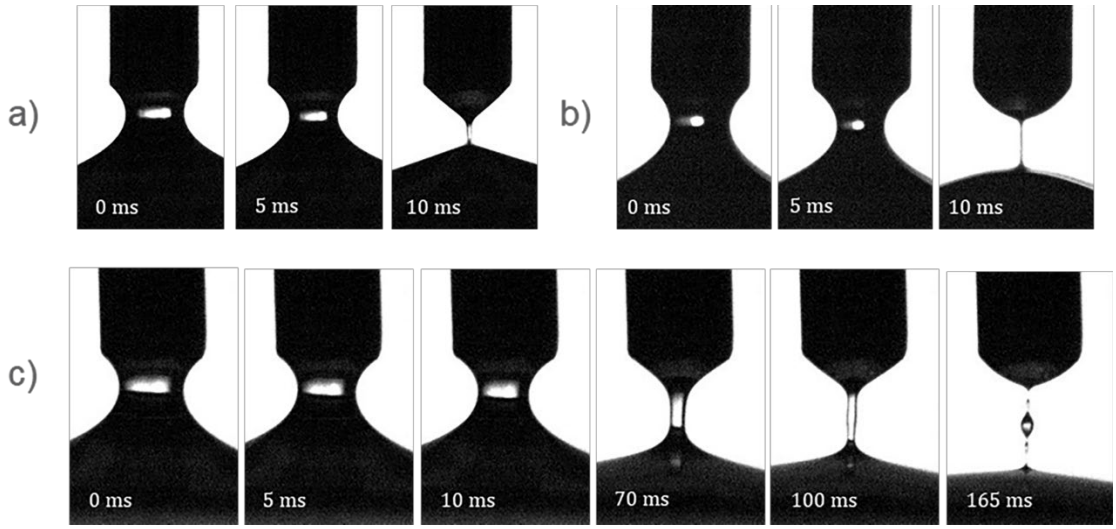

Figure 4-3: Radius evolution images starting at approximately 60% radius, taken 5 ms apart. (a) Balanced saline solution, containing no polymer or protein and showing no extensional relaxation behavior. (b) Vitesse ultrasonic cutter vitreous. (c) BiBlade pneumatic

Another characteristic difference between the PB and US samples was the beads-on-a-string structures that were only observed with the PB samples (Figure 4-3c, 165ms). These structures were observed on each of the 24 PB samples but were not observed on any US sample. This phenomenon is an indication of large protein fragments being present in the sample[122]. As the liquid bridge devolves, the fluid surrounding the protein structures evacuates the liquid bridge, leaving only a tangled mass of proteins. In several trials of this experiment, the beads-on-a-string structures persisted even after the fluid reached equilibrium. In these cases, the fluid bridge had to be manually removed before testing could resume.

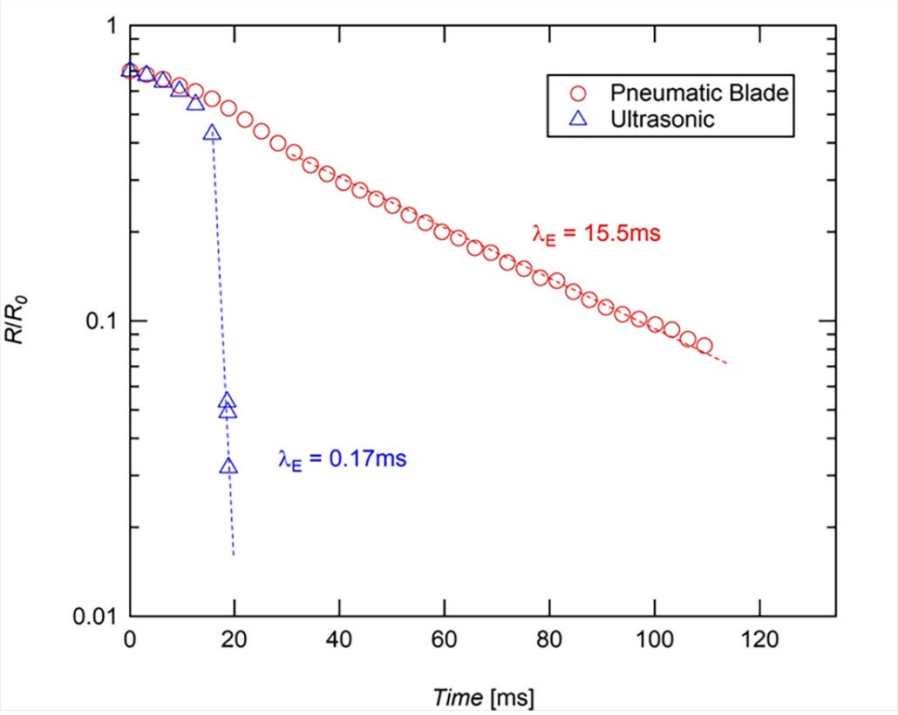

Figure 4-4: Radius evolution plots of representative US and PB samples. The elasto-capillary regime is identified with dotted lines. The first data points in the graphs represent the inertia-capillary regime governed by a power-law decay. Extensional relaxation time, λ_E, is calculated by fitting Eq. 1 to elasto-capillary regime.

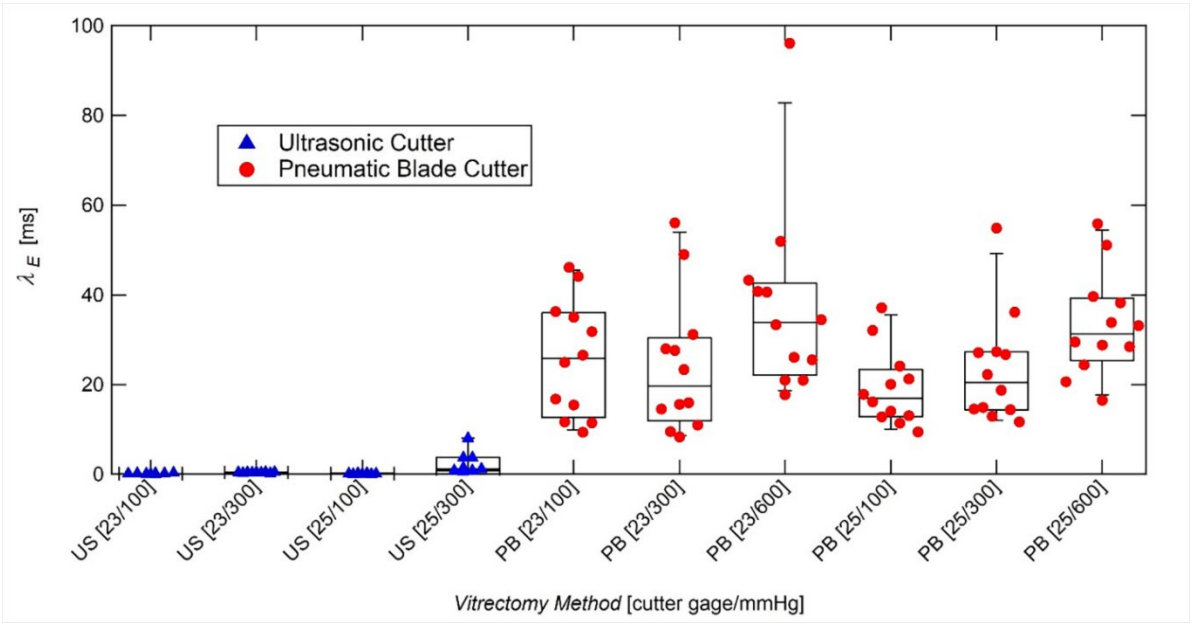

Figure 4-5: Box plots of sample relaxation times extracted using ultrasonic and pneumatic blade cutters. The average extensional relaxation time for US and PB samples were 0.37 ms and 27.25 ms, respectively.

4.4.1 Analysis

Extensional relaxation times (Figure 4-5) averaged 27.25 ms for the PB samples, and 0.37 ms for the US samples, a reduction of approximately 99%. The average extensional relaxation time for the US samples was significantly lower than the PB samples ($p<0.001$) with up to two orders of magnitude in difference. The inertia-capillary regime of the US samples dominated the flow, and the elasto-capillary liquid bridge existed for only a few image frames in each trial, indicating the protein interactions had little effect on the flow in these samples. The relatively high extensional relaxation time for PB samples culminating in beads-on-a-string structures indicate the elasto-capillary effects of the protein interactions were significant. This is an indication of relatively large protein fragments and high cross-linking of the proteins within the samples.

Higher vacuum pressure resulted in significantly higher average extensional relaxation time in US 23- and 25-gauge samples ($p=0.004$ and $p=0.018$, respectively) and PB 25-gauge samples ($p=0.002$). The vacuum pressure did not have a significant impact on the average relaxation time of the PB 23-gauge samples ($p=0.112$).

Smaller needle gauges exhibited higher average extensional relaxation times for US samples at 300 mmHg ($p=0.032$), but not at 100 mmHg ($p=0.548$). For PB samples, the needle gauge did not significantly impact the average extensional relaxation time at any of the three vacuum pressures (100 mmHg: $p=0.149$, 300 mmHg: $p=0.903$, 600 mmHg: $p=0.543$).

4.5 Discussion:

The macromolecular structure of the vitreous is dominated by a collagen fiber network inflated by hyaluronan and water. Pastor-Idoate et al (2017) evaluated the US vitrector by qualitatively examining the histopathological changes in the vitreous after vitrectomy with US and PB vitrectors in pig cadaveric eyes, live swine, and human cadaveric eyes[118]. Similar surgical outcomes were recorded with the two technologies. With US vitrectomy, however, finer fragmentation of the collagen and fewer long collagen fibrils from the residual collagen network was observed. Using this micro-extensional rheology technique, we have confirmed that the US cutting action results in much lower extensional relaxation times and therefore smaller protein fragments of the extracted vitreous can be inferred.

The effects of vacuum pressure and probe gauge on extensional relaxation time were outweighed by the effect of cutting method (US vs PB). Generally, it is expected that higher pressures, which correspond to higher flow rates[104], would result in coarser fragmentation of the vitreous and therefore higher extensional relaxation times. Our results are in partial agreement with this expectation, but in the case of the 23-gauge PB probe, the statistical significance was not strong. Similarly, it is expected that larger probe gauges would result in larger vitreous fragments and therefore higher extensional relaxation times. Our results showed the extensional relaxation times of the extracted vitreous were not strongly dependent on the probe gauge.

The results of this study support the findings of Pastor-Idoate et al (2017), that the use of US cutters results in high fragmentation of the vitreous[118], which may allow for smaller needle gauges to be used during vitrectomy. PB cutters require a non-trivial amount of intact material to be aspirated by the needle, which requires needles to be relatively large[104]. US cutters, however, fragment the vitreous prior to aspiration into small enough particles as to behave like water.

Therefore, smaller needles may be used, which reduces the size of the entry wound during vitrectomy procedures with US cutters.

These results also indicate that many of the limitations identified by Stanga et al (2017)[104] can potentially be overcome by US cutting action. These limitations include undesirable turbulence at the cutter port and increased traction on the retina. The finer and continuous fragmentation of the US samples leading to lower extensional relaxation time may reduce the required vacuum pressure of these vitrectors. This has the potential to reduce risk of damage to the retina caused by the vacuum force during extraction.

Finally, the US action may show potential for the development of new tools and techniques. It can be utilized in a variety of geometries to improve ergonomics and promote safety. Since US cutters can effectively liquify the material around it, the results of this study also show promise that the technology can be applied to stiffer biological materials.

4.5.1 Limitations:

The goal of this paper was to quantify and assess the effect cutting method has on the rheological properties of extracted vitreous. To do so, we measured the extensional relaxation time, which is an indicator of the relative length of protein polymer fragments contained in a sample. The results presented here indicate that the US cutter chops vitreous into a much smaller fragments, as expected. However, this conclusion was not directly confirmed. If desired, the relative size of the proteins in samples of vitreous extracted using PB and US vitrectors can be directly confirmed using microscopy techniques like those used by Pastor-Idoate et al (2017)[118].

4.6 Summary

In summary, we have assessed ultrasonic vitrectomy technology and its performance compared to conventional pneumatic blade vitrectors. By using extensional rheology, we were able to show significant differences in the vitreous samples extracted using the two cutter styles, where typical shear rheology was not likely to do so. When extracted using an ultrasonic cutter, the extensional relaxation times of the vitreous samples were orders of magnitude shorter compared to samples extracted using the pneumatic blade cutter (US sample mean: 0.37ms, PB sample mean: 27.25ms). These results confirm that the ultrasonic cutter breaks the vitreous collagen into very small fragments compared to pneumatic cutters. This has broad implications for improved ergonomics and safety of the ultrasonic cutter, as well as for the development and improvement of vitrectomy devices and techniques using ultrasonic technology.

Chapter 5 : Enhanced Understanding of CSF Properties and the Influence of Cellular and Protein Constituents

5.1 Introduction

To understand neuropathological protein aggregation, it is necessary to also understand the mechanical characteristics of the fluid in which it occurs. While tau aggregation in diseased brains is often observed within cells, there is also evidence to suggest that tau aggregates are found extracellularly, within the fluids surrounding and penetrating the brain tissue. Furthermore, the healthy clearance of waste such as these tau aggregates, flowing through the tortuous path of intracellular space, may also inadvertently contribute to the progression and propagation of these pathological features. Therefore, to more fully understand the mechanical contribution of physiological fluid flow through and around brain tissue to disease, we must first characterize the fluid itself, cerebrospinal fluid.

Cerebrospinal fluid (CSF) is key to the protection and normal physiological function of the central nervous system. In a typical adult, the volume of CSF is approximately 150ml, most of which is produced in the ventricles of the brain, and flows into and through these ventricles, the subarachnoid spaces, and the brain parenchyma[26]. CSF is then re-absorbed into the venous system via arachnoid granulations, primarily through the superior sagittal sinus[31,32]. CSF supplies nutrients and maintains homeostasis of the interstitial fluid environment of the brain. This function helps maintain normal neuronal function and removes metabolic by-products and interstitial waste like carbon dioxide and proteins such as amyloid-β and tau that could interfere with normal brain function[27,123].

Conventionally, CSF is considered to be water-like, or is often simplified and approximated to have the properties of water[124]. However, due to the presence of proteins like albumin and tau, as well as cellular content including blood and immune cells[125], it is hypothesized that CSF actually exhibits significant non-Newtonian behavior, particularly at lower shear rates[126]. CSF from typical healthy humans contains 5,000-20,000 cells/mL and approximately 15-60 mg/dL of protein[125,127]. However, the concentration of cells and protein can vary significantly with the condition of the patient[128]. Therefore, in order to fully describe CSF behavior, it is critically important to understand the impact of the various CSF constituents on its rheology.

In this chapter, novel research performed to more fully characterize CSF is presented, with emphasis on the impact elevated blood and proteinaceous contents have on the rheological behavior of the fluid. The rheological techniques and results presented in this chapter are an indirect measurement of the interactions of molecules within CSF leading to non-Newtonian behavior. The more the constituents of CSF interact with one another, the more pronounced the non-Newtonian rheology will be, thus revealing critical characteristics that may influence physiological and pathological functions. Therefore, this research is a key step in understanding the CSF flow of injured and diseased brains and may contribute to the understanding of pathological protein aggregation as observed in CTE or Alzheimer's disease.

5.2 Motivation

With modern updated rheological techniques, a more accurate quantification of CSF rheology is possible. To our knowledge, the most comprehensive characterization of CSF rheology was performed by Bloomfield, et. al., who, using a concentric cylinder rheometer, found that CSF is

practically Newtonian with a viscosity similar to water[124]. They also found that the viscosity was independent of the contents of the CSF, and showed little-to-no correlation between cellular or protein concentration and viscosity. One significant gap, however, is that this paper only reported the CSF viscosity at shear rates between 150 s-1 and 1500 s-1 and neglected lower shear rates. Shear rates within CSF are not always high[129], however, and low shear-rate behavior may be overlooked with the current knowledge.

The stress response of a Newtonian fluid such as water will vary linearly with shear rate, and therefore its viscosity will remain constant. A non-Newtonian fluid's stress response will vary non-linearly, and its viscosity may instead be a variable function of shear rate. Many biological fluids exhibit a shear thinning behavior, meaning that as shear rate increases, the apparent viscosity of the fluid decreases. It is hypothesized that this occurs due to the randomly oriented and dispersed polymeric and cellular contents of the fluid becoming disentangled and flowing more freely at higher shear rates. Blood is an example of a shear thinning biological fluid, in which the red blood cells form ordered aggregates called rouleaux[130]. These three-dimensional cell structures flow more freely than when randomly dispersed, and thus reduce the apparent viscosity of blood as a whole[17]. We hypothesize that a similar phenomenon may occur within CSF, especially when higher than normal protein and cellular content is present within the sample.

Extensional rheology is a growing field where the properties of fluids are analyzed as they are subjected to extensional strain rather than the more typical shear strain described above. In shear flow, the velocity gradient is perpendicular to the direction of the flow. In extensional flow, the velocity gradient is parallel to the flow direction. There are many applications where extensional strains are important, such as dripping phenomena and constricting or accelerating flow fields. In particular, the cross-linking and molecular interaction of polymers and proteins in solution cause

fluids to exhibit non-Newtonian viscoelastic behaviors in extensional flow. Extensional methods have also been shown to be uniquely sensitive in measuring the influence of polymers and proteins within small volume dilute solutions[66,120], making it appropriate for the characterization of biological fluids such as CSF in which cells and proteins may be relatively disperse and which may only be available in small volumes.

Both shear and extensional rheological behavior may contribute to many mechanical phenomena within the brain, especially in abnormal or clinical circumstances. For example, since viscosity is a measurement of a fluid's response to applied stress, the dynamics of the brain and the deformation experienced by brain tissue, especially during TBI or related injuries may be influenced by CSF rheology. Additionally, because the flow through shunts and their associated apparatuses can occur at relatively low shear rates, analysis of shunt function may be enhanced by understanding the shear rate dependent behavior of CSF[131]. Furthermore, CSF rheology may contribute to the mechanisms used to clear and expel waste, such as the hypothesized glymphatic system[27,125,132,133]. Therefore, current and future CSF models may benefit from state-of-the-art rheological analysis. The goal of this research is to update the knowledge base of CSF rheological properties using state-of-the-art rheometry instruments and recently developed extensional rheology techniques, which will have significant implications for the understanding of the fluidic processes of the cranial system such as bulk CSF flow, injury mechanics, extracellular interstitial flow, and glymphatic clearance.

5.3 Materials and Methods

5.3.1 CSF Sample Collection

Institutional Review Board exemption was confirmed prior to specimen collection. CSF was collected from patients at Ronald Reagan UCLA Hospital with in-dwelling external CSF drainage catheters. Indications for CSF diversion in these patients most commonly included trauma, hydrocephalus, hemorrhage, or infection.

5.3.2 Nexcelom Cell Counter

The total cellular concentration of each sample was measured using a Nexcelom Cellometer Auto 2000 (Nexcelom Bioscience, Lawrence MA, USA). Prior to testing, each CSF sample was appropriately diluted and dispensed in 20uL increments to be read by the cellometer. The cellometer was set to the total cell concentration test, which counts all cells without debris and viability greater than 98%. Generally, each sample was diluted 2:1 with phosphate buffer solution. In samples where the overlapping cellular content caused counting errors, however, the samples were further diluted up to 20:1, in order to accurately count the cells on the slide.

5.3.3 Urine Dipstick

Depending on the condition for which CSF drainage was required, CSF samples contained varying amounts of aqueous proteins. To quantify the relative proteinaceous composition of the samples, each was tested using a urine dipstick (LW Scientific, Lawrenceville GA, USA). The results of this test are quantified as Negative (no protein detected), Trace (<30 mg/dL), + (30-100 mg/dL), ++ (100-300 mg/dL), +++ (300-2000mg/dL), and ++++ (>2000 mg/dL). Though this test does not identify the different proteins present within the sample, understanding their general relative effects will enhance the understanding of non-Newtonian behavior of CSF.

5.3.4 Shear Flow

To investigate the shear-rate dependence of CSF rheology, a Discovery HR-3 rheometer with a recessed end concentric cylinder attachment (TA Instruments, New Castle DE, USA) was employed. As the expected viscosity of the CSF samples was estimated to be approximately 1-2 mPa·s (1-2 centipoise), the concentric cylinder attachment was chosen over a cone-and-plate configuration to avoid any confounding effects of surface tension on the sample's resistance to flow[46]. The rheometer operates by submerging a cylindrical probe (28mm diameter) into the sample within a fixed concentric cylinder of known diameter (30mm diameter). The sample fills the gap between the probe and cylinder wall. A motor within the instrument rotates the probe at a prescribed angular velocity and simultaneously measures the amount of torque required to maintain that velocity. Given the known geometry of the probe and concentric cylinder, this torque reading can be analyzed to measure a host of rheological properties.

Using the Discovery HR-3 rheometer with concentric cylinder attachment, a flow sweep was employed to investigate the shear-rate dependent behavior of CSF rheology. In this test, the probe rotates at a progression of prescribed angular velocities and thus produces prescribed shear rates. The stress response of the sample is calculated from the geometry of the rotating probe and the torque generated by the instrument to maintain the angular velocity.

For each CSF sample, 8mL was tested at 37°C at shear rates varying from 0.3 to 300 s-1. These limits were chosen based on the capabilities of the instrument[46], but only the behavior between 1 and 100 s-1 are reported below. For low viscosity fluids, low shear rate rheology may be influenced by interfacial effects such as surface tension, while high shear rate rheology may be influenced by secondary flow effects such as turbulence[46], causing the recorded data to exhibit erroneous behavior. Between 1 and 100 s-1, the influence of these secondary effects is small, and the data

can be considered reliable. Each data point was collected as a five second time average after thirty second equilibration period.

5.3.5 Power Law Model

The shear rate dependent viscosity data was collected and fit to a power law model (Equation 5.1), from which the infinite shear viscosity, μ∞, and the flow behavior index (n-index), n, was calculated. K is the consistency index, which is an indicator of the fluid′s viscosity. An n-index close to unity indicates a Newtonian fluid, while lower n-indices indicate shear thinning behavior.

$$\mu = \mu_\infty + K\dot{\gamma}^{n-1} \tag{5.1}$$

5.3.6 Casson Shear Thinning Model

In addition to the power law model used in the main text, shear thinning fluids such as cerebrospinal fluid (CSF) can also be modeled using Casson's method, where viscosity (μ [mPa·s]) and shear rate ($\dot{\gamma}$ [s-1]) from which a yield stress (τ_y [mPa]) and viscosity constant (K_v [mPa·s]) can be calculated.

$$\sqrt{\mu} = \sqrt{\tau_y/\dot{\gamma}} + \sqrt{K_v} \tag{5.2}$$

5.3.7 Extensional Flow

To analyze the extensional rheological properties of small samples, we adapted a simple rheometric method (described in Chapter 2) to apply a large strain rate to very small sample volumes[120]. Sample volumes were typically between 50-100 microliters. Each was dispensed onto a hydrophobically treated substrate to create a domed droplet. Using a KRUSS tensiometer (K-100, KRUSS GmbH, Hamburg, Germany) in the Surface Tension setting, each sample droplet was

penetrated with a 1mm diameter platinum rod. The probe penetrated 0.5mm into each sample. The probe was then quickly removed, so that the surface of the sample was perturbed upward. Each sample was tested independently three times. Testing was performed at room temperature, but each sample was kept at 4°C prior to testing.

5.4 Results

5.4.1 Sample Characteristics

Thirty-two samples were collected and tested for cellular concentration and protein concentration (Table 5-1). While all samples exhibited some cellular content, half of the samples (16 of 32) showed obvious signs of hemorrhage, with cellular concentration greater than 107 cells/mL. One sample (sample 29) was an outlier and had cellular concentration approaching whole blood, representing an extreme case. Five samples had cellular concentrations low enough to approach that of normal CSF (<1x106 cell/mL), but should still be considered elevated relative to normal CSF. Twenty samples were found to have elevated protein concentration. Eleven had protein content greater than 300 mg/dL, and another nine had samples greater than 100 mg/dL. The assessment of protein concentration using the urine dipstick is somewhat subjective, so great care was taken to record a conservative estimate of protein concentration in each case.

Table 5-1:Summary of test results for each sample per power law model

Sample	Protein	Cells/mL ($x10^6$)	Cell size (µm)	K (mPa·s)	μ_∞ (mPa·s)	n-index	λ_E (ms)
1*	+++	2.2	7.4	--	--	--	0.14
2*	Trace	0.4	11.9	--	--	--	0.13
3*	+++	396.0	10.7	--	--	--	0.13
4*	+	10.1	8.6	--	--	--	0.18
5*	++	408.0	11.2	--	--	--	0.15
6*	++	59.1	11.4	--	--	--	0.17
7	++	10.3	8.7	1.74	0.98	0.23	0.14
8	+	1.3	7.9	0.56	1.00	0.44	0.12
9	+++	5.6	10.7	2.08	0.95	0.48	0.13
10	++	1.9	7.8	1.04	0.91	0.24	0.13
11	Trace	1.5	11.2	0.91	0.90	1.00	0.12
12	+++	28.1	7.6	1.18	1.02	0.11	0.07
13	Trace	0.9	9	0.90	0.91	0.98	0.07
14	Negative	1.0	9.6	0.60	0.87	0.74	0.07
15	Trace	0.8	10.8	0.74	0.95	0.93	0.08
16	Trace	0.4	8.3	0.68	0.99	0.94	0.09
17	+++	12.1	9.2	0.76	0.94	0.34	0.09
18	+++	1.2	10.3	1.87	0.88	0.24	0.09
19	+	2.0	8.2	3.47	0.94	0.10	0.08
20	+++	275.0	11.2	3.44	1.32	0.25	0.35
21	Trace	3.2	9.1	0.66	0.93	0.79	0.11
22	++	3.8	8.1	2.27	0.89	0.14	0.12
23	Negative	3.1	8.6	0.89	0.92	1.01	0.14
24	++	30.9	8.7	1.26	0.93	0.24	0.18
25	++	25.9	10.7	1.14	0.95	0.45	0.19
26	++	10.2	9.4	0.71	0.92	0.64	0.20
27	+++	387.0	9.9	3.33	1.17	-0.16	0.19
28	+++	142.0	10.1	2.27	1.02	0.32	0.16
29**	+++	2300.0	11.2	4.74	2.53	0.67	0.35
30	Negative	1.7	8.6	0.93	0.94	0.53	0.12
31	++	54.1	7.3	0.38	0.85	0.74	0.14
32	+++	346.0	9.8	2.16	0.96	0.00	0.16
Average	**++**	**71.8**	**9.4**	**1.56**	**0.96**	**0.47**	**0.14**

5.4.2 Flow Sweep

Power Law Model:

When significant cellular or protein concentration was present within the sample, the sample exhibited shear thinning behavior, especially at low shear rates below 10 s-1. This shear thinning behavior generally dissipated approaching 100 s-1, at which point all samples behaved as a Newtonian fluid. When both cellular and protein concentration were relatively low, however, the sample behaved comparatively more like a Newtonian Fluid throughout testing. The results of these tests are displayed in Figure 5-1 and Table 5-1.

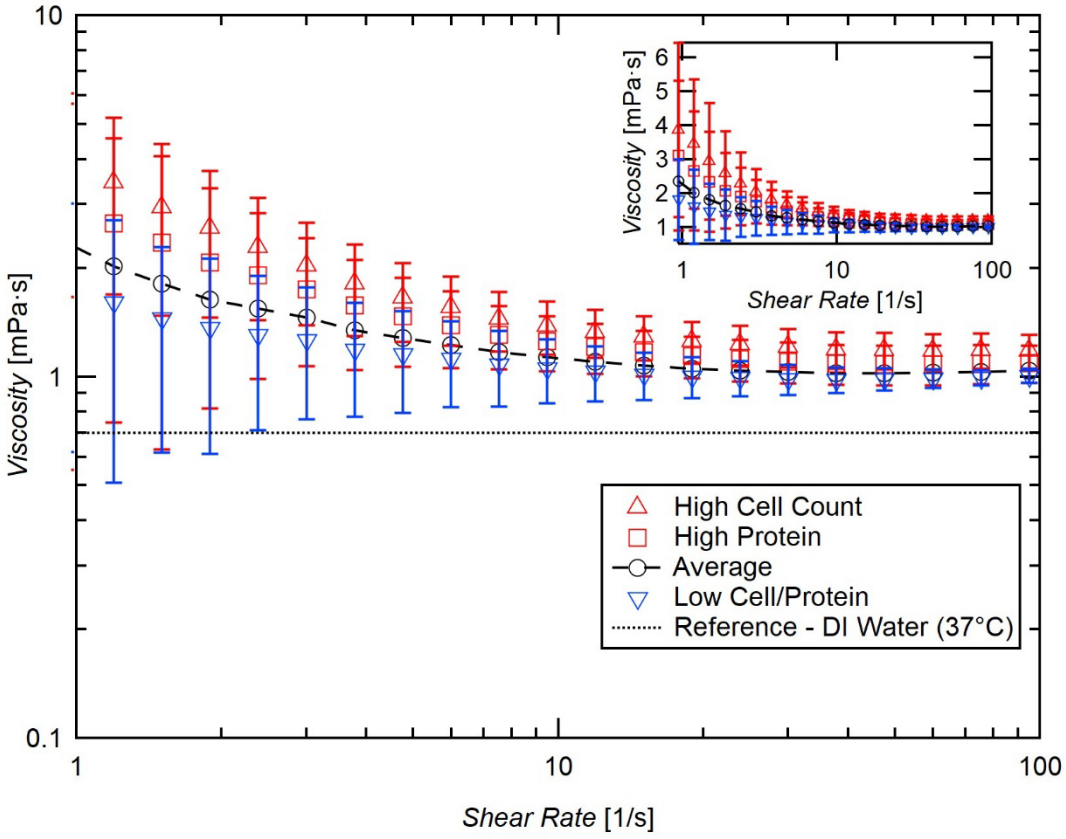

Figure 5-1: Summary of flow sweep test of samples with high cellular concentration (red triangles, >107 cells/mL), high protein (red squares, >30 mg/dL), and relatively low cellular/protein concentration (blue inverted triangles, <106 cells/mL, <30 mg/dL blue inverted triangles, <10^6 cells/mL, <30 mg/dL blue inverted triangles). Inset: semilog plot of data with linear viscosity axis.

Though the samples exhibited shear thinning behavior at low shear rates, the findings of previous studies are confirmed for moderate to higher shear rates. Each sample data set was fit to equation (5.1) and the infinite shear viscosity (μ_∞) was calculated. The average overall μ_∞ for these samples is very close to distilled water, 1.0 mPa·s. Although there is a positive correlation between viscosity and cellular concentration, the effect is small, and a great change in cellular content is necessary to significantly influence the viscosity of CSF (Figure 5-2).

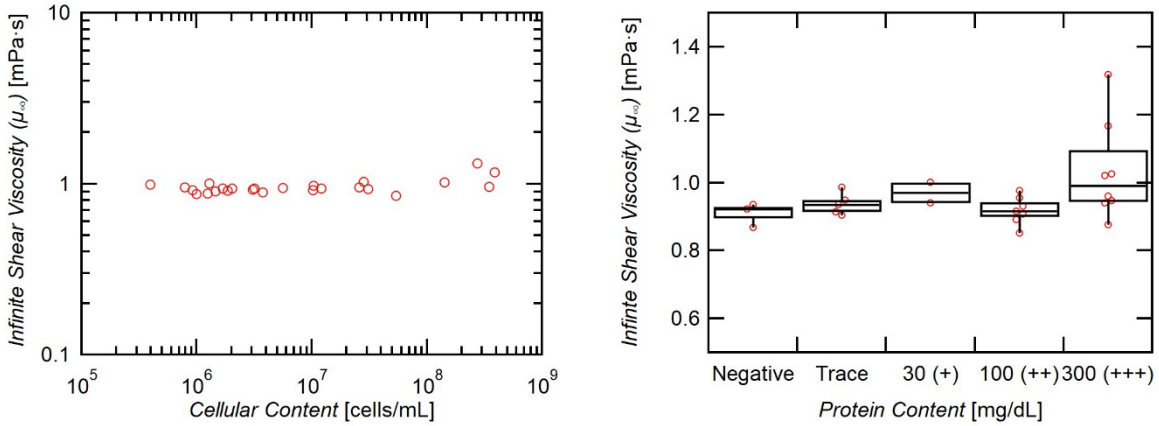

Figure 5-2: Effect of cellular and protein content on infinite shear viscosity. Viscosity increases minimally with increasing cellular content (slope = 6x10-13), and only samples with 300+ mg/dL of protein exhibited a significantly increased viscosity (p = 0.05).

Elevated protein content (>30 mg/dL) similarly shows a weakly significant increase in viscosity (p-value 0.08), and only the group measuring greater than 300 mg/dL individually exhibited a significantly elevated viscosity when compared to the protein-negative group (p = 0.05) (Figure 5-2). Though the measurement was statistically significant, the difference in means is only roughly 0.1mPa·s (0.9 vs 1.0 mPa·s).

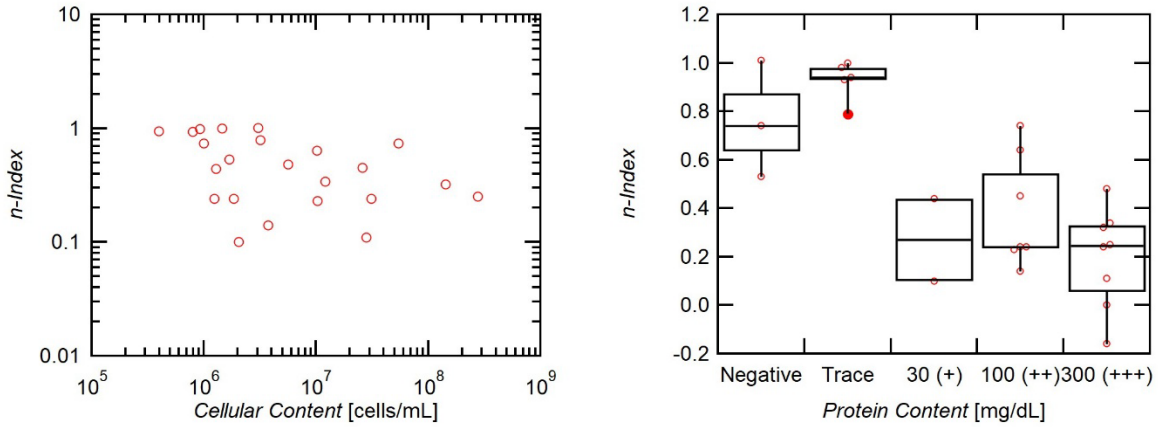

Figure 5-3: Effect of cellular and protein content on n-index. Increased cells indicate a lower n-index and therefore greater non-Newtonian shear thinning behavior. Increased protein has a strong effect on n-index as elevated protein correlates with lower n-indices and greater shear thinning behavior.

The shear thinning behavior was quantified by fitting the viscosity and shear rate data to equation (5.1) and extracting the flow behavior index (n-index), n. n-values close to unity indicate a Newtonian fluid, while lower n-values indicate shear thinning behavior. n-values approaching zero indicate steeper decreases in viscosity at lower shear rates.

A negative correlation between the n-index and cellular content of the CSF is observed, with increasing cellular concentration indicating more significant shear thinning behavior (Figure 5-3). Samples with elevated protein content also exhibited significantly greater shear thinning behavior, as the n-index for these samples was significantly lower than samples with either negative or trace protein ($p < 0.001$) (Figure 5-3).

Casson-Shear Thinning Model:

While the Casson model fit low-shear rate data relatively well, it consistently underestimated the infinite shear viscosity observed in our experimental data. Therefore, the power law model was sufficient for the main text of this article. Using the Casson model, however, one can calculate and

compare the τy necessary to induce flow of non-Newtonian CSF and how it is influenced by its proteinous and cellular constituents. The fitting data from these experiments is collected in Table 5-2.

Table 5-2: Summary of test results for each sample per Casson Shear-Thinning model

Sample	Protein	Cells/mL ($x10^6$)	Cell size (μm)	τ_y (mPa)	K_v (mPa·s)
1*	+++	2.2	7.4	--	--
2*	Trace	0.4	11.9	--	--
3*	+++	396.0	10.7	--	--
4*	+	10.1	8.6	--	--
5*	++	408.0	11.2	--	--
6*	++	59.1	11.4	--	--
7	++	10.3	8.7	0.54	0.82
8	+	1.3	7.9	0.02	0.92
9	+++	5.6	10.7	1.07	0.71
10	++	1.9	7.8	0.35	0.76
11	Trace	1.5	11.2	0.00	0.90
12	+++	28.1	7.6	0.23	0.90
13	Trace	0.9	9	0.02	0.85
14	Negative	1.0	9.6	0.18	0.80
15	Trace	0.8	10.8	0.03	0.85
16	Trace	0.4	8.3	0.01	0.93
17	+++	12.1	9.2	0.14	0.89
18	+++	1.2	10.3	0.63	0.76
19	+	2.0	8.2	1.55	0.71
20	+++	275.0	11.2	1.27	1.06
21	Trace	3.2	9.1	0.01	0.94
22	++	3.8	8.1	0.63	0.77
23	Negative	3.1	8.6	0.00	0.90
24	++	30.9	8.7	0.25	0.78
25	++	25.9	10.7	0.17	0.86
26	++	10.2	9.4	0.06	0.97
27	+++	387.0	9.9	1.35	0.79
28	+++	142.0	10.1	0.92	0.80
29**	+++	2300.0	11.2	0.64	3.63
30	Negative	1.7	8.6	0.45	0.88
31	++	54.1	7.3	0.24	0.83
32	+++	346.0	9.8	0.98	0.94
Average	**++**	**71.8**	**9.4**	**0.45**	**0.96**

Using the Casson model, there was observed a positive relationship between τy and both protein and cellular concentrations (Figure 5-4, Figure 5-5). As concentrations of both increased, the yield stress of the fluid also increased. The viscosity constant, Kv, however, was relatively the same across samples regardless of protein or cellular concentration (Figure 5-5).

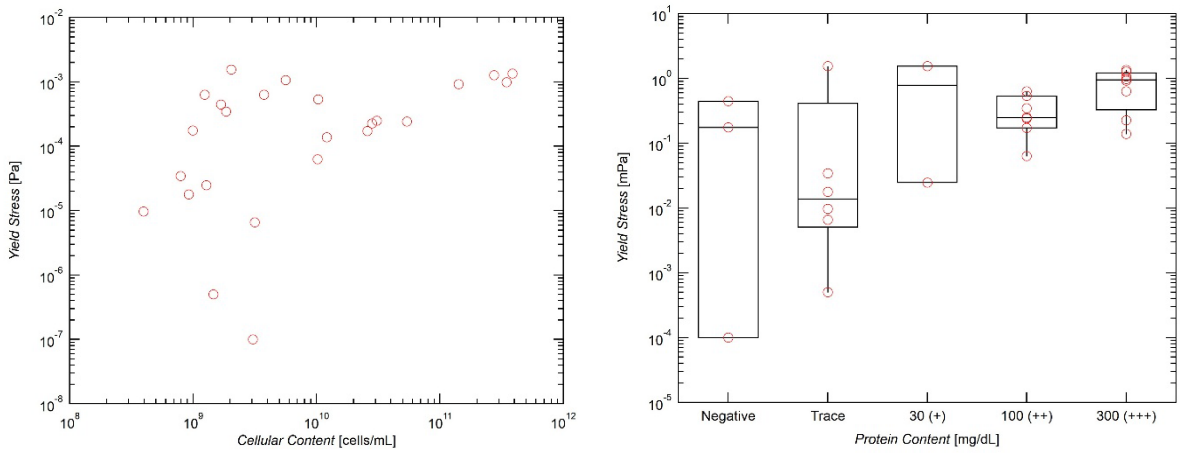

Figure 5-4: Effect of cellular and protein content on yield stress (τ_y). τ_y increases with increasing cellular and protein concentration.

These data further enhance the understanding of non-Newtonian, shear thinning behavior of CSF with elevated protein or cellular concentrations. Particularly at low shear rates, the shear thinning behavior and yield stress of the fluid should be considered, especially when in the presence of elevated protein or cellular concentrations. This is especially true for flows that are unsteady, where a yield stress may be required to induce flow.

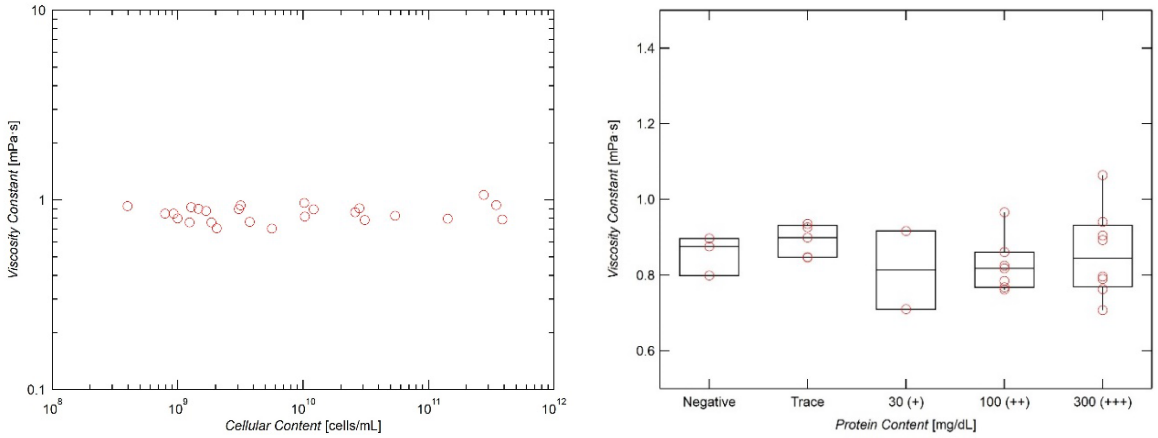

Figure 5-5: Effect of cellular and protein content on viscosity constant, K_v. Protein content has little effect on K_v.

5.4.3 Micro-Extensional Rheology

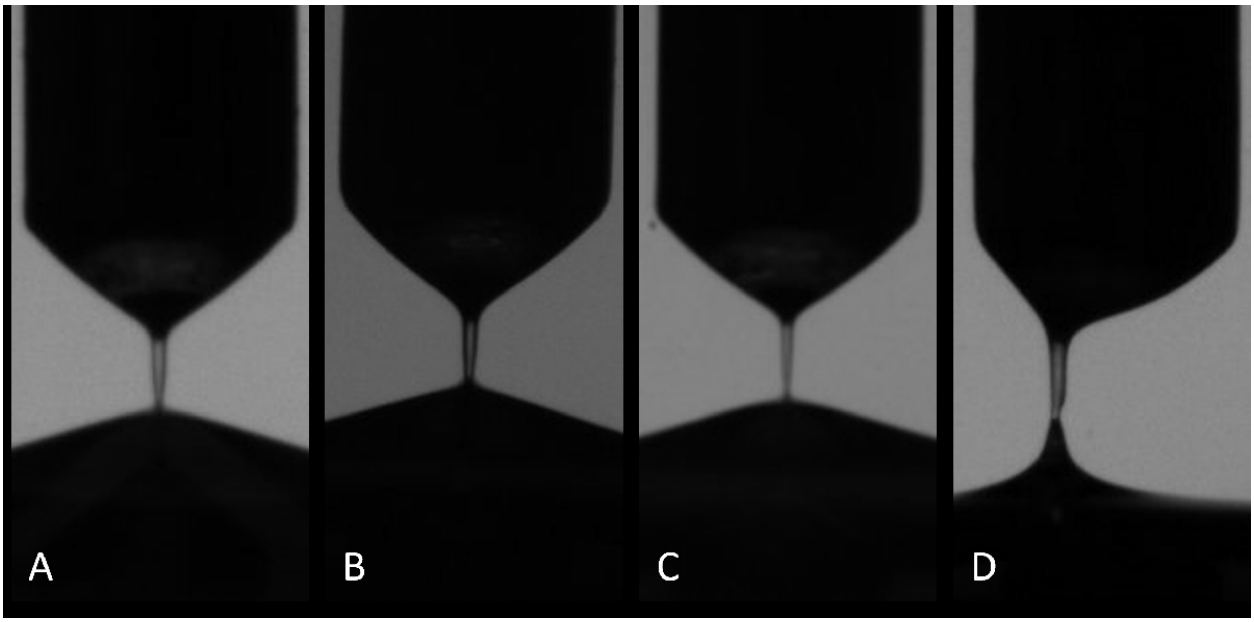

Figure 5-6: Examples of elasto-capillary bridge observed in all samples. Samples pictured in A-D represent increasing cellular and protein content as well as increasing extensional relaxation time. Sample pictured in D is a statistical outlier, and exhibited an average relaxation time approximately three times longer than the others.

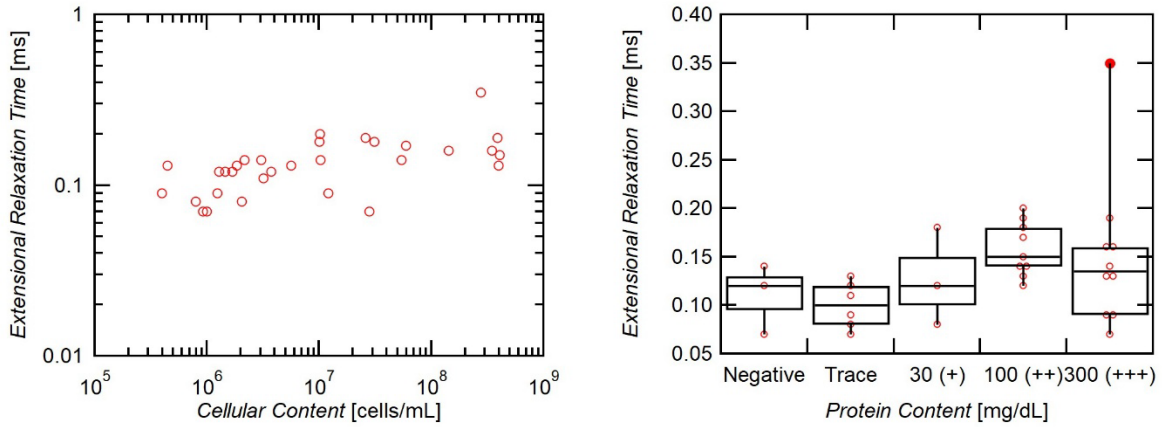

Figure 5-7: Effect of cellular and protein content on extensional relaxation time. Cellular content has a positive correlation to extensional relaxation time (slope = $1.7x10^{-10}$). Samples with elevated protein (>30 mg/dL) also exhibited significantly higher extensional relaxation times ($p = 0.005$).

All samples exhibited weak, but non-zero non-Newtonian extensional behavior (Figure 5-6). The average extensional relaxation time for all samples tested was 0.14 ms with a slight positive correlation to both cellular and protein concentration (Figure 5-7). While all samples showed a clear liquid bridge characteristic of proteinaceous solutions, in many samples, this structure only lasted a few frames, or about 100-300 µs. One sample whose content approached that of whole blood, however, exhibited clear beads-on-a-string phenomena (Figure 5-8), indicative of high flow-induced protein entanglement[122].

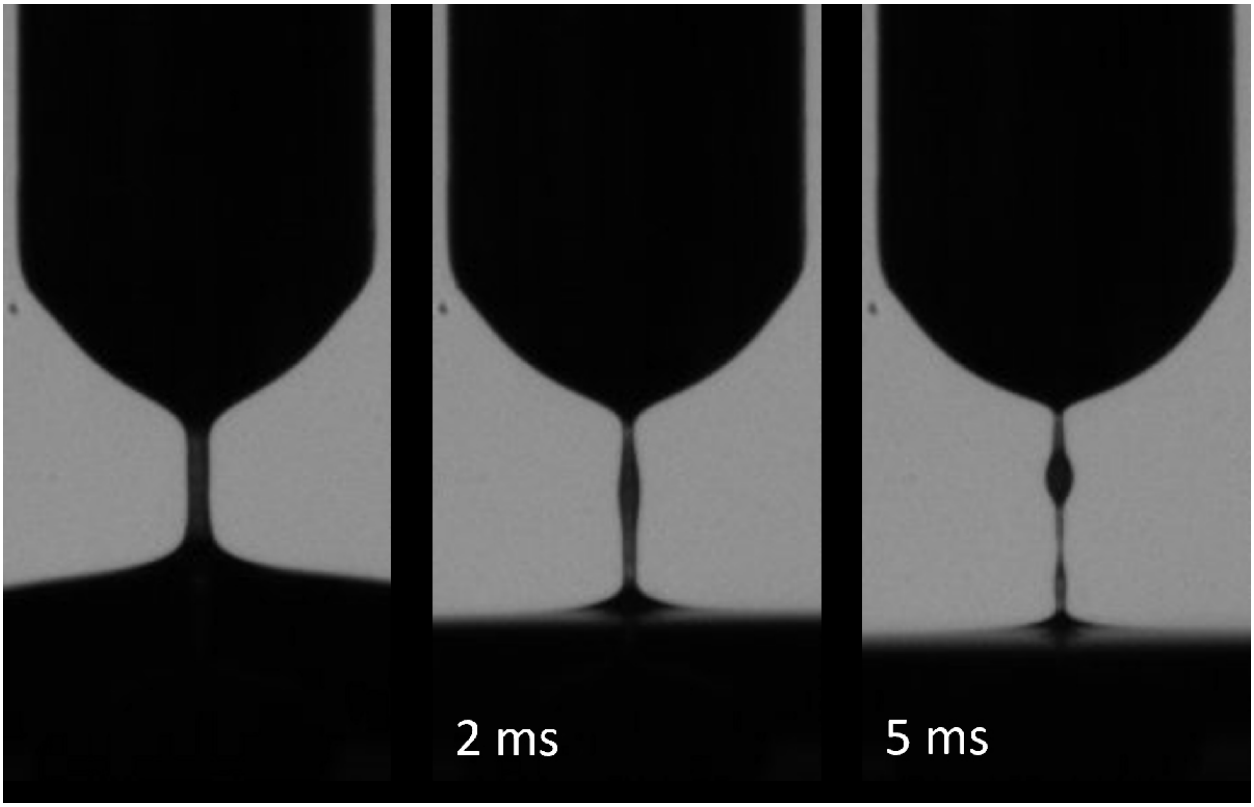

Figure 5-8: Outlier CSF sample with cellular content approaching blood (3x10^9 cells/mL). Elasto-capillary bridge persisted for longer than all other samples and exhibited beads-on-a-string morphology indicating high protein interactions. Sample is unique but represents an extreme hemorrhage.

5.5 Discussion

These results empirically demonstrate non-Newtonian behavior of CSF, especially in the presence of elevated cellular or protein concentration. One glaring weakness in the existing literature on CSF rheology are that prior studies have centrifuged CSF to characterize the underlying fluid behavior. We opted instead to characterize the extracted CSF sample as a whole, to better reflect the in vivo condition. We sought a variety of clinical conditions, and quantified the proportion of the cellular and protein constituents of the samples, to understand their relative impact on CSF rheology. With higher cellular and protein concentrations and lower shear rates, significant shear thinning behavior was observed, especially at shear rates below 10 s^{-1}. Although

the results and conclusions from these data are limited, they have broad applicability to clinical situations when normal CSF conditions cannot necessarily be assumed.

Another important weakness in the existing literature on CSF rheology is that shear rates studied have largely been relatively high and have neglected lower shear rates that may be relevant to clinical applications such as shunts or the glymphatic system. In our studies, at higher shear rates, CSF indeed exhibited Newtonian behavior with a viscosity close to that of distilled water. Furthermore, when cellular and protein concentrations were relatively low, the CSF samples also exhibited behavior closer to Newtonian, even at low shear rates. These results confirm that bulk flow of healthy CSF can generally be considered Newtonian, and to approximate its viscosity to water may be appropriate. However, at lower shear rates, as in stagnation flow or creeping flow, the non-Newtonian behavior of CSF must be considered, especially in instances where cellular or protein concentration may be abnormally or locally elevated.

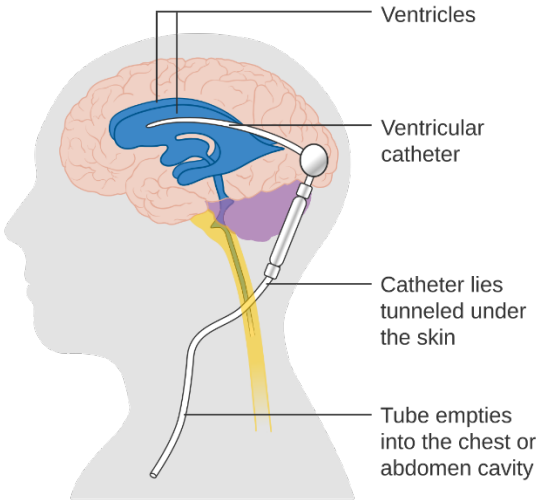

Figure 5-9: Diagram showing a brain shunt[134]

For example, flow through CSF shunts implanted to relieve hydrocephalus (Figure 5-9) can be very slow, with shear rates on the order of 1 s^{-1}. In addition, the presence of the indwelling hardware is known to increase the cellular and protein content of the CSF in these patients[135]. Therefore, the analysis of shunt function would benefit from the consideration of non-Newtonian behavior at low shear rates. Another example is where CSF interacts with other brain constituents[136]—in the interstitial spaces of brain parenchyma, the perivascular spaces, the arachnoid granulations adjacent to the venous sinuses, and the hypothesized glymphatic system, which pulses CSF through interstitial space to clear waste resulting from normal neuronal function. This transported waste may change the local composition of CSF such that it exhibits more significant non-Newtonian behavior. Furthermore, the proposed glymphatic pathway is characterized by low velocity flow of CSF[137], which therefore may exhibit significant non-Newtonian behavior. As more work is done to characterize the glymphatic pathway, it is imperative that non-Newtonian behavior of the transport media be considered. Finally, CSF reabsorption is hypothesized to occur with contributions from both pressure and osmotic gradients, again at very low velocity flow[138,139].

In extensional flow, the behavior of CSF is not greatly influenced by its constituents, except in extreme cases. While all samples exhibited measurable non-Newtonian behavior, characterized by a short-duration elasto-capillary bridge, only two had significantly elevated extensional relaxation times. In one of these samples, the cellular and protein concentration approached that of whole blood, and should be considered an extreme case. In the majority of samples tested, the extensional relaxation time was relatively short, approximately 0.14 ms. To benchmark this relaxation time, it is higher than a tau solution tested by Hosseini, et. al., and 10 mg/mL 35 kDa PEO (0.03 ms)[120]. It is lower, however, than hypersonically extracted vitreous solution (0.37 ms)[140] and 10 mg/mL 100 kDa PEO solution (0.67 ms)[120]. Non-Newtonian extensional behavior is significant when the

duration of the extensional phenomenon is similar to the relaxation time. Therefore, extensional non-Newtonian behavior should be considered in short duration extensional processes, on the order of 0.1 ms.

The shear rate data presented in the flow sweep section of this report are limited in scope, and knowledge of this function will be enhanced by further measuring the low shear rate non-Newtonian behavior of CSF. Below 1 s-1, the shear thinning behavior appeared to continue, though the data approaches the limit of our instrument's capabilities. More accurate descriptions of CSF non-Newtonian behavior could therefore be achieved with more sensitive instrumentation, including lower shear rate and yield stress behavior. Similarly, above 100 s-1, secondary flow effects were significant, and data collected above this range are unreliable. Therefore, we were unable to achieve a continuous shear rate ramp to higher shear rates in the same sample without changing the instrumentation part way through testing. Having this continuous data would further confirm the Newtonian behavior of CSF at higher shear rates, as well as improve the quantification of the shear thinning behavior at lower shear rates.

5.6 Summary

In summary, we have demonstrated for the first time that CSF with elevated cellular or protein concentration behaves as a non-Newtonian fluid, especially at low shear rates. At high shear rates, it is confirmed that CSF behaves as a Newtonian fluid regardless of constituent concentration, with a viscosity similar to distilled water. In extensional flow, CSF exhibits measurable non-Newtonian behavior, but the effect is relatively weak and is independent of the cellular and protein concentration of the sample, except in extreme circumstances. These findings have broad

implications for the characterization of CSF and CSF-related processes, and its non-Newtonian behavior should be considered when analyzing the fluid dynamics of CSF in a wide variety of physiologic and pathologic conditions.

The results of these rheological tests reveal characteristics of CSF and the interactions of its constituents. In studying neurodegenerative protein aggregation, it is critical to understand the mechanical properties of the environment in which the aggregation may occur. In this chapter, it has been shown that there are instances in which extreme elevation of protein and blood content causes CSF to exhibit significantly higher non-Newtonian behavior, especially in extensional flow. This suggests that the physiological changes following traumatic injury may also influence the flow of CSF through the brain, potentially contributing to protein aggregation.

Chapter 6 : Extensionally Induced Protein Aggregation

6.1 Introduction

As discussed in chapters 1 and 3, protein aggregation is a highly complex and dynamic process that often begins with a misfolded monomer. These misfolds drive the formation of small oligomers, which may then nucleate into larger, more ordered assemblies such as amyloid fibrils[141]. In the context of disease, these aggregates can aggregate into neurofibrillary tangles (NFTs) and disrupt cellular homeostasis, interfere with normal protein function, and induce inflammatory responses or cytotoxicity. Notably, protein aggregation underlies a wide range of neurodegenerative disorders, including Alzheimer's disease, Parkinson's disease, Huntington's disease, and prion diseases, where the accumulation of misfolded protein species is a hallmark of their pathology[57]. Despite its significance to many diseases, however, the *mechanical* mechanisms that could contribute to protein aggregation remain poorly understood.

In this chapter, novel work done to explore the mechanical contributors of protein aggregation is presented. Following the methods introduced in Chapter 3, experimental results are presented, analyzed, and discussed. These results reveal aggregation behavior of BSA in extensional flow fields as well as offer new research questions to explore in later chapters. The work presented in this chapter leads directly to the analysis and experimental framework introduced in Chapter 7.

6.2 Motivation

Specifically in CTE, a neurological disease generated by repeated traumatic hits to the brain, protein aggregation is a key pathological marker[7,8]. The mechanisms that drive tau aggregation are

therefore understandably the subject of immense research effort as CTE gains prominence in the medical field as well as in the public eye[142,143]. However, the difficulty in studying this aggregation is two-fold. One, because CTE can only be diagnosed post-mortem, the exact time-based progression of the pathological aggregation cannot be captured. Second, the brain is a mechanically dynamic environment, where biological, chemical, and physiological forces are all acting and interacting constantly within, throughout, and between tissue. This creates a complex mechanical environment that is still poorly understood.

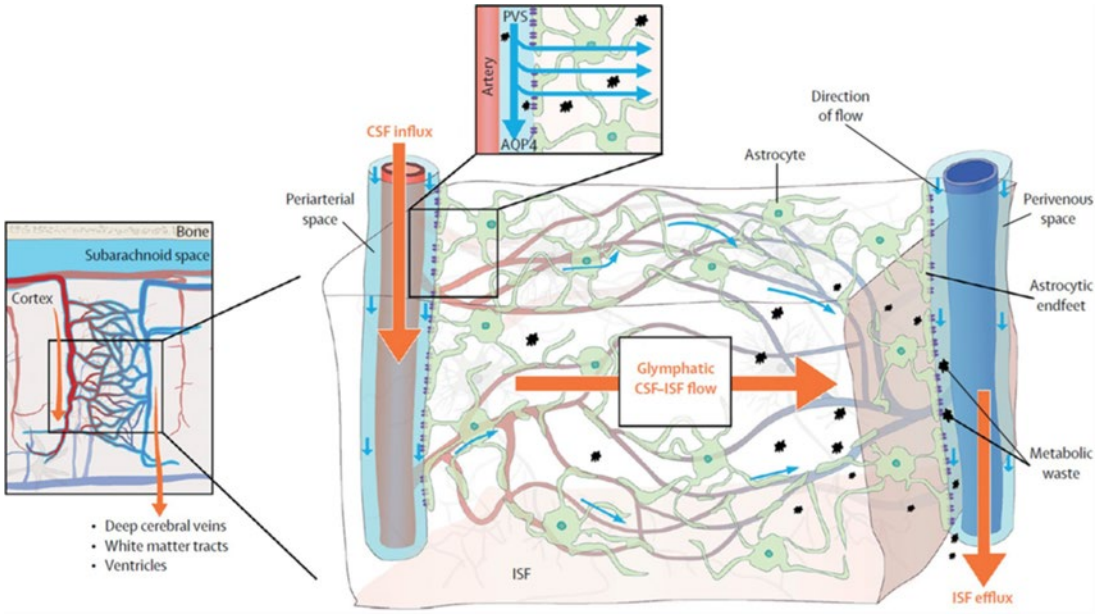

Figure 6-1: Complex and tortuous fluid flow environment of the brain perivascular space and parenchyma in which protein aggregation has been observed[33]

Specifically, the fluid environment of the brain is complex, and the stresses and strains of the various fluids are not well understood (Figure 6-1). Not only would we expect these environments to change dramatically following injury or disease, but we would also expect that regular changes throughout a normal process of maintaining homeostasis would also cause significant and critical changes to the fluid and mechanical environment of the brain[36].

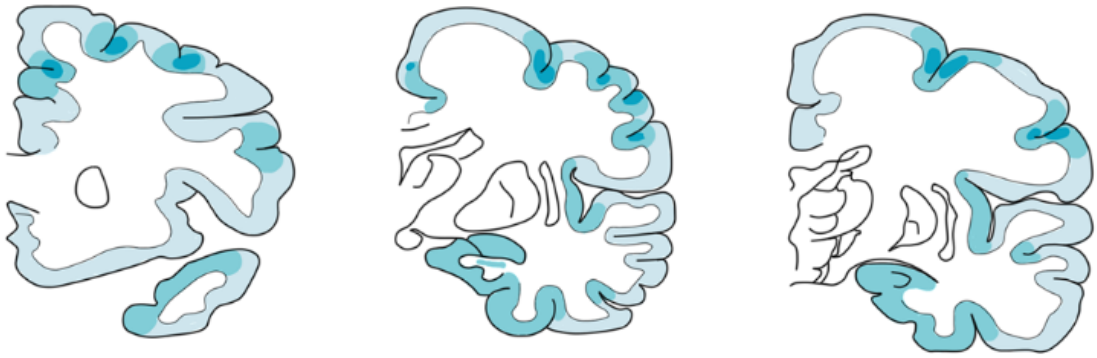

Figure 6-2: Tau pathology progression in a CTE brain over time[4]. Aggregation is initially observed in sulchal folds (dark blue), but propagates through the tissue and can be observed throughout cerebral cortex (light blue) over time.

With respect to protein aggregation, we know that its initiation can be linked to an acute injury, but we also know that it persists and propagates over time after the acute injury (Figure 6-2)[4]. Therefore, a new framework is desired, where the mechanical behavior of protein aggregation coupled with the mechanical behavior of the biological environment of the brain can be analyzed. Thus, the mechanisms that could contribute to pathological protein aggregation can be characterized, potentially leading to advancements in diagnosis, treatment, prediction, and ultimately prevention of injury and disease.

6.3 Methods and Materials

BSA is a readily available protein that has many biological and biochemical uses. Importantly, it does not self-aggregate and is relatively stable[78], making it an ideal analog to pathologically relevant proteins like tau, which also does not self-aggregate[80]. We received BSA Fraction V from (Roche Diagnostics GmbH, Mannheim Germany) which is delivered in lyophilized (freeze-dried)

powder. We created a 10mg/mL solution by allowing the BSA to dissolve in 100mM NaCl solution. The homogenization of the BSA solution was done at room temperature, with minimal mixing. Instead, the BSA powder was dispensed onto the surface of the saline and allowed to mix by diffusion and gravity for an hour or more, or until the mixture was homogenous and no bubbles or remnants on the surface were observed. Immediately prior to testing, each sample was passed through a 450nm PVDF syringe filter (Basix, Pittsburgh PA).

This "raw" solution was tested on the DLS and was found to have an effective diameter between 7-8nm. When mixed using a magnetic mixer, however, the mixture homogenized faster, but the turbulence induced by the mixer caused apparent aggregation. With DLS, the magnetically mixed raw solution exhibited an effective hydrodynamic diameter of 50-100nm. It is suspected that the turbulence caused by the magnetic mixer induced interfacial phenomena that enhances BSA's hydrophobic-hydrophilic conformational changes, potentially causing unwanted aggregation before testing[78].

6.3.1 Syringe Drive

The syringe drive mechanism presented in chapter 3 was used in three phases in this experiment. Prior to treatment, the syringes used in the reciprocal extensor were rinsed and sterilized. Approximately 1.2 mL of protein solution was extracted into the syringe and gently agitated to remove any vestigial bubbles that may have been aspirated during the process. The syringe drive was set to three input plunger speeds, 0.75, 1.5, and 3.0 mm/s corresponding to extensional rates of 1440, 2880, and 5505 s^{-1}, respectively. At each input speed, the samples were treated to 50, 100, 250, 500, 1000, 1500, and 2000 passes through the reciprocal extensor.

After treatment, the reciprocal extensor was disassembled and the syringes were inspected for signs of precipitated protein aggregates. The syringes were gently agitated to release any particulate from the syringe walls, and the sample was dispensed into a clean and sterilized microcuvette.

6.3.2 Dynamic Light Scattering and Nanoparticle Tracking Analysis

After treatment, each sample was allowed to rest for approximately 10 minutes before testing using DLS [Brookhaven Instruments, Nashua, New Hampshire, USA]. The cuvette was gently tapped to dislodge any small bubbles and was wiped down to remove any residue from the visibility window. The DLS was set to run five two-minute tests. The DLS recorded the effective hydrodynamic diameter of the suspended particles, using auto-slope analysis and a dust filter, to account for anomalously large particles. Therefore, the resulting effective diameter is to be interpreted as representing bulk suspended particles and not the largest particles nor the precipitated particles that may have yet to settle at time of testing. The reported “combined” effective diameter represents the calculation based on the entirety of the collected data over the five tests, whereas the “average” is the average calculated effective diameter for each of the five tests.

Samples were also tested using NTA [Viewsizer 3000, Horiba Instruments Inc., USA]. The samples were tested by dispensing 400uL from the middle of the sample, to avoid any precipitated particles that would have settled to the bottom. The cuvette was gently and repeatedly tapped to remove any bubbles that may have been caught during the dispensation. After the NTA optical window was calibrated and adjusted, the test was started. The test included 16 measurements identifying the number and size of the particles within the visual window. Between each test, the sample was gently mixed using a magnetic stirrer to count the particles in a different location. The

measurements were collected and displayed as a size distribution chart. A sample of filtered DI water was also measured to establish a baseline of suspended particles. This baseline was subtracted from the protein analysis to identify only the aggregated particles that resulted from the extensional flow treatment.

6.3.3 Thioflavin T (ThT) and Fluorescent Microscopy

After testing in DLS and NTA, 10uL of 800uM ThT [EMD Millipore Corp, Burlington MA, USA] was added to the sample. The samples were allowed to rest overnight to allow for adequate time for the dye to penetrate any potential protein aggregates. In the aliquot, any aggregated precipitation sank to the bottom while resting. 10uL of this pellet was extracted and placed on a clean microscope slide for visualization.

Images were captured using a highspeed camera at 2x, 10x, and 20x magnification in both brightfield illumination and under fluorescence using a Nikon eCFP filter cube [Nikon Instruments Inc., Melville, NY, USA]. If any particles were visible, they would be confirmed to be protein aggregates by the presence of the ThT fluorescence. If fluorescence was low, the exposure time of the image capture was adjusted in order to obtain clear images.

6.3.4 Increased Concentration Tests

Our hypothesis is that the flow fields combined with crowding effects of the protein molecules create a favorable environment in which aggregation can be induced or enhanced. Therefore, we also subjected a variety of BSA concentrations to the reciprocal extensor to study how the aggregation behavior is affected. We increased the concentration of the BSA solution to 40mg/mL and 100mg/mL and tested at 1.5mm/s input velocity for 50, 100, 250, 500, 1000, 1500, and 2000

runs through the reciprocal extensor. Samples were again tested using the DLS to compare the aggregation behavior.

6.4 Results

This test was conducted in three phases, with input plunger velocities of 0.75, 1.5, and 3.0 mm/s. In each phase, a pattern emerged, consistent with the findings of Dobson et al, but including precipitation of visible particulate that has heretofore been unseen. In each phase, using DLS and NTA, distinct regimes could be identified depending on how many treatment runs to which the samples were subjected. Over relatively few runs, little to no aggregation was detected. At intermediate runs, particle size began to grow, but only after high runs would precipitate be visible to the naked eye. Notably, the number of runs at which the regimes transition were the same for each input velocity (Figure 6-3).

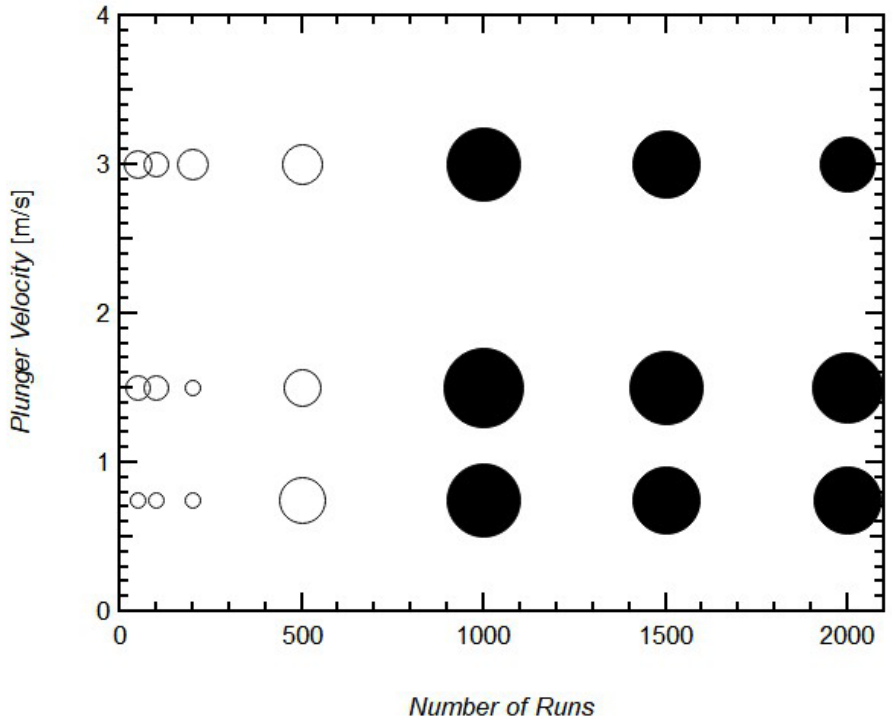

Figure 6-3: Results of experiments displayed as plunger velocity vs number of runs. The hollow circles are tests where no precipitated particulate was observed, while the solid circles are tests in which precipitation was observed. The size of the circles represents the relative size of the effective hydrodynamic diameter, compared to the raw particle size of 8nm (see Figure 6-5 for more details).

6.4.1 Dynamic Light Scattering and Nanoparticle Tracking Analysis

The extensional field created by the reciprocal extensor once again was shown to cause BSA proteins in solution to aggregate. When untreated, the 10mg/mL BSA solution consistently exhibited suspended particles with an effective hydrodynamic diameter between 7-9nm. To compare and analyze the effect of the extensional mechanism itself, a sham test was conducted to determine appropriate normalization of the DLS and NTA results. In this sham test, a sample was placed within the reciprocal extensor as if a normal test were to be conducted. However, instead of treating the sample to multiple extensional field runs, the apparatus was disassembled and the sample was tested in DLS and NTA. Compared to the raw test, the effective diameter of the sham

test was unchanged from the raw, untreated sample. Generally, however, the more treatment a sample was subjected to, the larger the effective diameter of the suspended particles (Table 6-1).

Table 6-1: Averaged DLS results from 10mg/mL BSA tests

	0.75 mm/s		**1.5 mm/s**		**3.0 mm/s**	
Runs	Diam. (nm)	Polydispersity	Diam. (nm)	Polydispersity	Diam. (nm)	Polydispersity
50	17.633	0.090	49.533	0.177	59.300	0.147
100	18.200	0.105	44.367	0.117	44.933	0.138
250	15.233	0.098	18.100	0.114	68.833	0.152
500	159.700	0.193	99.433	0.199	120.067	0.106
1000	**429.200**	**0.371**	**467.133**	**0.428**	**424.367**	**0.243**
1500	**346.367**	**0.315**	**403.800**	**0.283**	**337.533**	**0.197**
2000	**345.133**	**0.322**	**363.200**	**0.296**	**243.033**	**0.189**

*Data in **bold** indicate visible precipitation was observed in these experiments.

Polydispersity, an approximation of the homogeneity of the solution, also increases with increased extensional treatment of the solution. Both the hydrodynamic diameter and polydispersity together indicate that more frequent and larger particles are being measured via DLS with increasing treatment of the solution in the reciprocal extensor.

These results were also consistently supported by NTA, which showed both increasing average particle size as well as increased number of particles (Figure 6-4).

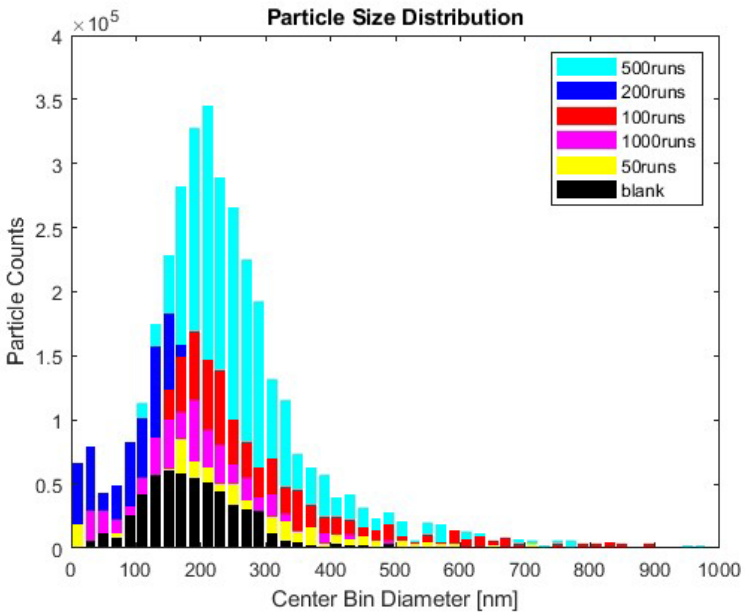

Figure 6-4: NTA particle distribution of 10 mg/mL BSA solution after 50-1000 runs at 1.5mm/s.

Both DLS and NTA, however, have the same limitation, that as particle size grows beyond a certain point, these light scattering techniques are no longer appropriate for counting or sizing the particles. This can be seen in both measurements that as the number of runs to which each sample is treated increases past a point, the apparent size and number of particles decreases (Figure 6-5). Not to be confused with the aggregation suddenly reversing, this phenomenon also coincides with an increase in visible particulate precipitating out of the solution.

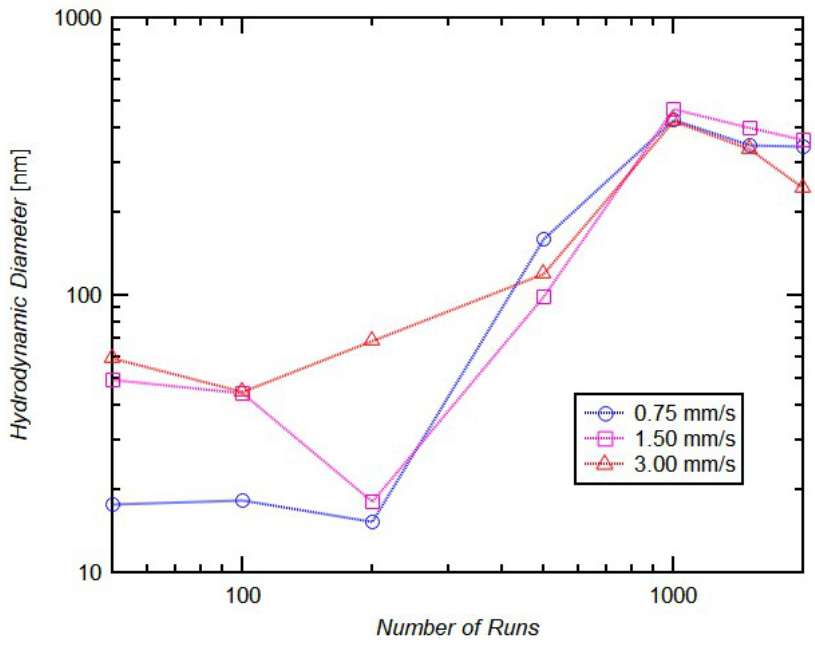

Figure 6-5: Hydrodynamic diameter of particles measured in DLS. As number of runs increases, hydrodynamic diameter also increases until 1000 runs. Afterward, the apparent hydrodynamic diameter begins to decrease, corresponding with precipitation becoming visible in the sample.

6.4.2 Visible Particulate Analysis

After a relatively high number of extensional treatment runs, particulate becomes visible to the naked eye, resting at the bottom of the extensor syringes. As the extensional treatment continues, this sediment became increasingly apparent. These particles would not be detected in DLS or NTA because their increased size would cause them to sediment and move outside of the measurement view. Furthermore, at this scale, particle motion is no longer dominated by Brownian motion, on which DLS and NTA rely, and instead is driven by gravity. Thus, a different measurement technique was necessary to analyze these particles.

We can estimate the size of particles precipitating out of the solution by analyzing the sedimentation velocity of protein particles of a particular size. If we assume the roughly globular particles to have a spherical shape, a sedimentation velocity can be estimated using Eq. 6.1, where

ρ_s is the protein density, ρ_f is fluid density, and μ is viscosity of the solvent. This relationship can be rearranged to determine an expression for particle size, d, as a function of time-to-settle, t.

$$v = \frac{d^2 g(\rho_s - \rho_f)}{18\mu}$$

$$d = \sqrt{\frac{18h\mu}{tg(\rho_s - \rho_f)}} \tag{6.1}$$

In the reciprocal extensor, the fluid exiting the capillary forms a jet. This jet may contribute to secondary flow effects that mix the solution and cause large particles to remain in suspension. For a particle to escape this jet and precipitate, it must traverse the jet in the allotted amount of time. Thus, a conservative estimate for velocity can be determined, indicating the minimum size that an aggregate must achieve in order to precipitate as observed. If the jet diameter is approximately 300um, and each test duration is roughly 30s, then the minimum particle size can be estimated.

$$d = \sqrt{\frac{18h\mu}{tg(\rho_s - \rho_f)}} = \sqrt{\frac{18(1.5e-4)m\ (0.001)Pas}{30s\ g\ 350\ kg/m^3}} = 5um \tag{6.1.1}$$

Therefore, for particles to precipitate and visibly collect within the syringe, they must exceed 5um in diameter. In a more aggressive estimation, one can assume the sedimentation distance must be the diameter of the syringe, 2.3mm. In this estimation, the particle size would need to be much larger, approximately 20um. The smallest particle visible to the naked human eye is between 20-50um. Thus, while this estimate is much more aggressive, it may be reasonable, given the observed visible particles that amass during this test.

6.4.3 Microscopy

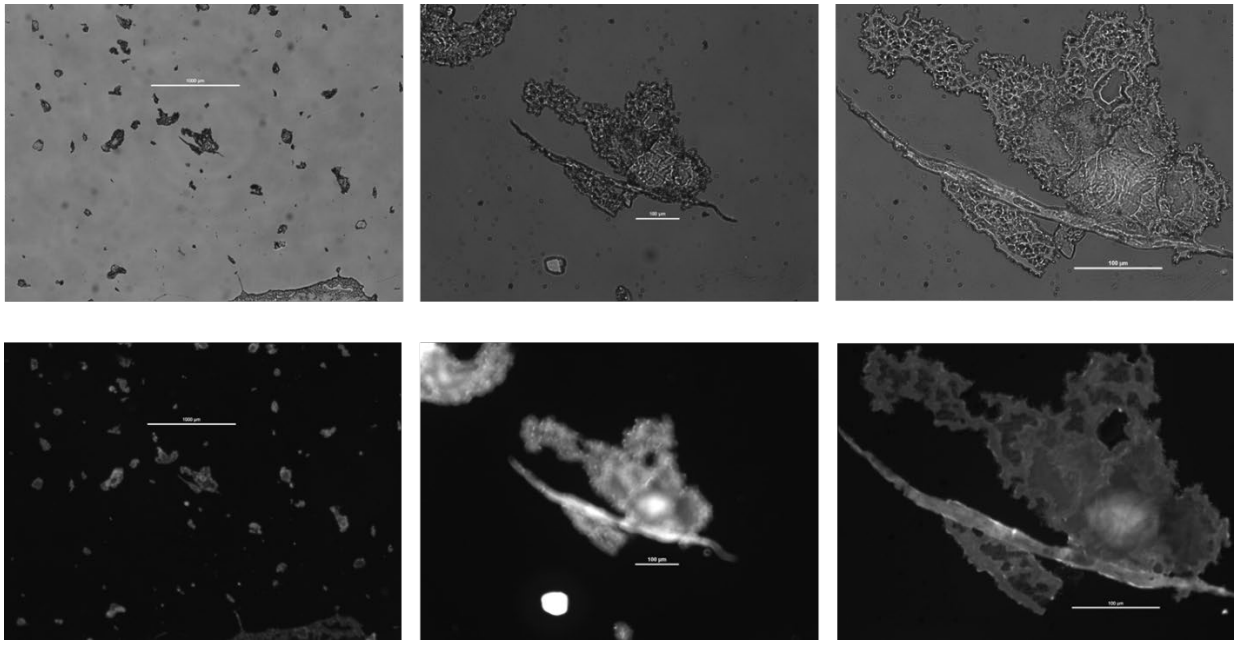

Figure 6-6: Resultant aggregation precipitates. From left to right, 2x (scale bar: 1000 um), 10x (scale bar: 100um), 20x (scale bar: 100 um). Top row images were captured using bright field illumination. Bottom row images were captured using fluorescence illumination and ECFP filter cube.

At the end of each run, the samples were transferred to aliquots and mixed with 10uL of 800uM ThT. After sufficient resting and allowing any aggregated particles to settle, 10uL of the pellet within each aliquot were extracted and observed under microscopy (Figure 6-6). When viewed using the Nikon ECFP filter, the fluorescence of the ThT could be observed (Figure 6-6 bottom row, Figure 6-7 right). The intensity of the fluorescence indicates the presence of amyloid structures within the apparent protein aggregates. Thus, it is confirmed that not only do BSA protein molecules aggregate in response to the extensional flow, but they do so in such a way that may have clinical relevance, being similar to amyloid pathologies.

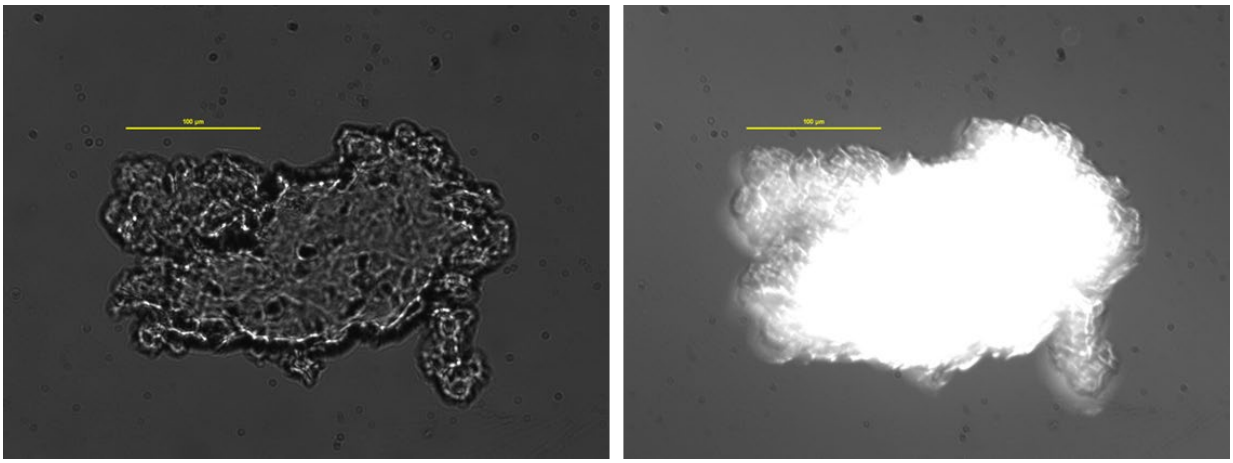

Figure 6-7: Example of BSA fluorescence after tagging with ThT. Left Brightfield illumination of protein particle at 20x magnification (scale bar 100um). Right: Fluorescent illumination of protein particle at 20x magnification (scale bar 100um).

Qualitatively, the observed precipitated particles were larger and more plentiful after long exposures to the extensional flow treatment when compared to short duration tests. The shape of the precipitated aggregates were mostly globular, though secondary structures could be observed that suggested the presence of fibrillary sub-structures (Figure 6-8). Furthermore, the size of the resulting aggregates were on the order of 100 um and larger. Together with the fluorescence, not only do the protein molecules appear to aggregate in pathologically relevant ways, but they do so producing particles that are on the order of size of pathologically observed tau aggregates in brains such as those suffering from Alzheimer's and CTE.

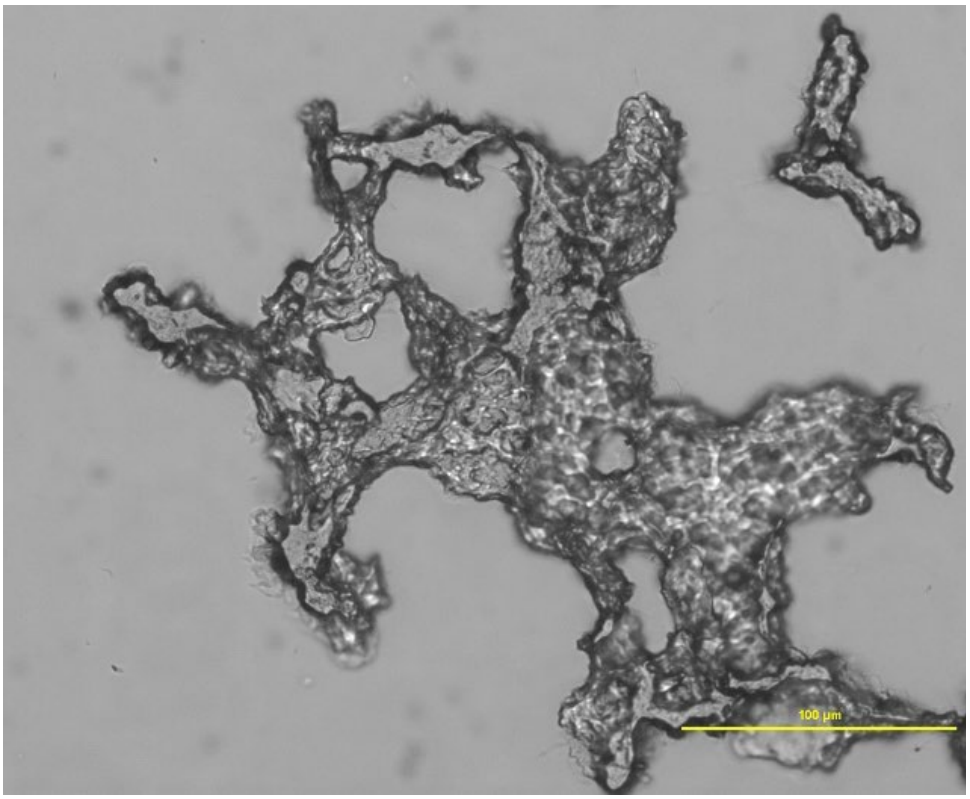

Figure 6-8: Protein aggregate under brightfield illumination at 20x magnification. Particle shows tangled fibrillar substructure within the branches of the globular structure.

6.4.4 Higher concentration tests

At higher concentrations, the aggregation behavior was further enhanced (Figure 6-9). Fewer runs were necessary to observe similar aggregation behavior and precipitation was observed earlier as well (Table 6-2). Furthermore, where aggregation began to plateau in the 10mg/mL testing after about 1000 runs, no such plateau was observed with the higher concentration solutions. This indicates that a limit to the precipitation volume may exist for each concentration, although further testing would be required to confirm this.

Table 6-2: Averaged results from increased concentration BSA experiments

	10 mg/mL		40 mg/mL		100 mg/mL	
Runs	Diam. (nm)	Polydispersity	Diam. (nm)	Polydispersity	Diam. (nm)	Polydispersity
Raw	7.800	0.098	6.400	0.134	5.600	0.170
50	49.533	0.177	20.533	0.095	17.000	0.098
100	44.367	0.117	10.800	0.090	20.267	0.097
250	18.100	0.114	21.300	0.111	**185.700**	**0.206**
500	99.433	0.199	**88.767**	**0.148**	**72.133**	**0.150**
1000	**467.133**	**0.428**	**114.200**	**0.154**	**111.467**	**0.150**
1500	**403.800**	**0.283**	**160.167**	**0.202**	**212.733**	**0.178**
2000	**363.200**	**0.296**	**280.167**	**0.251**	**792.5**	**0.280**

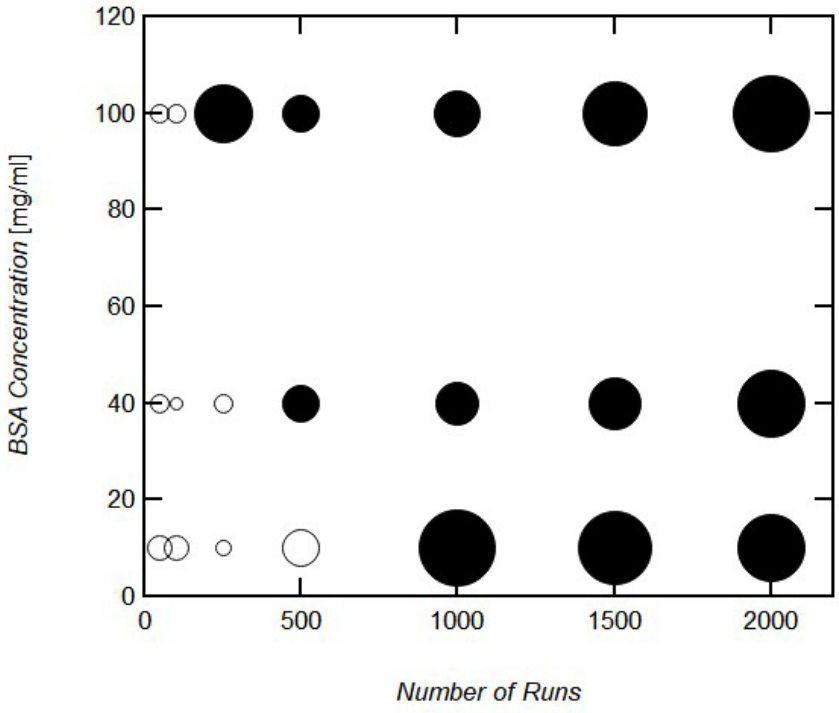

Figure 6-9: Concentration vs Number of Runs. DLS results from testing different concentrations of BSA.

6.5 Discussion

The results presented here confirm the capability of this reciprocal extensor mechanism to induce protein aggregation in protein solutions. The experiments produced robust, visible, and precipitated particles that are similar in size to physiologically relevant protein aggregation plaques, which has before now never been observed. Furthermore, when stained with ThT, the presence of amyloid folds was also confirmed, which has significant implications for the applicability of this method to pathologically relevant proteins.

We had hypothesized that the increase of flow field intensity as represented by the input plunger velocity, as well as the increased concentration of BSA in the test solutions, would show an enhanced aggregation behavior, as had been observed previously[20]. While increasing the concentration of the protein solutions did indeed correspond to an enhanced aggregation behavior, it is notable that the increased plunger velocity did not obviously have an impact on the aggregation behavior with respect to the number of runs. As will be seen in the next chapter, a deeper analysis into this phenomenon can potentially reveal critical physics associated with the material properties of the protein as well as the flow field that is induced by the reciprocal extensor.

A future consideration for this work is that the number of trials was limited by the time required per run. At the lower velocities, a full suite of experiments could take up to a week or more, and the number of runs for each experiment was chosen to efficiently characterize the aggregation behavior of the BSA solutions. However, with more testing, a higher resolution of the aggregation behavior could be achieved, and the dynamics of aggregation and precipitation could be more fully characterized. For example, this discrete testing clearly shows that a threshold exists beyond which aggregation begins to significantly increase and precipitates are observed. By developing a method to more continuously characterize the aggregation based on extensional intensity and duration, the

exact threshold could be determined, and a model that could predict aggregation could be developed. This research would significantly enhance our understanding of protein aggregation and would move us closer to fully bridging the gap between mechanical stimulus and industrial, physiological, or even pathological protein aggregation.

6.6 Summary

In this chapter, the results of testing BSA in a reciprocal extensor were presented, confirming that extensional flow fields are capable of inducing and enhancing protein aggregation. Not only were the results of Dobson[20] confirmed, precipitated particulate that resulted from these tests were analyzed and the presence of amyloid structures within the aggregated particles were also confirmed. Furthermore, the particles that resulted from this work were found to be on the order of size of physiological and pathologically relevant particles found in proteinopathies such as CTE and Alzheimer's disease.

Chapter 7 : A Non-Dimensional Phase Diagram

7.1 Introduction

A counterintuitive result is observed in Chapter 6 Figure 6-3 and Table 6-1, that as the intensity of the extensional field is increased by increasing velocity, the number of runs required to achieve aggregation remains the same. One may expect that increased intensity would result in increased aggregation, but this is not observed in these experiments. Instead, the duration of the exposure to the extensional field appears to be a more critical parameter to predict aggregation behavior of a particular protein. While the extensional field is more intense at higher velocities, the period in which the protein solution dwells within the extensional field is shorter in each pass. Therefore, at higher velocities, similar aggregation behavior is observed over a shorter period of dwell time (Figure 7-1).

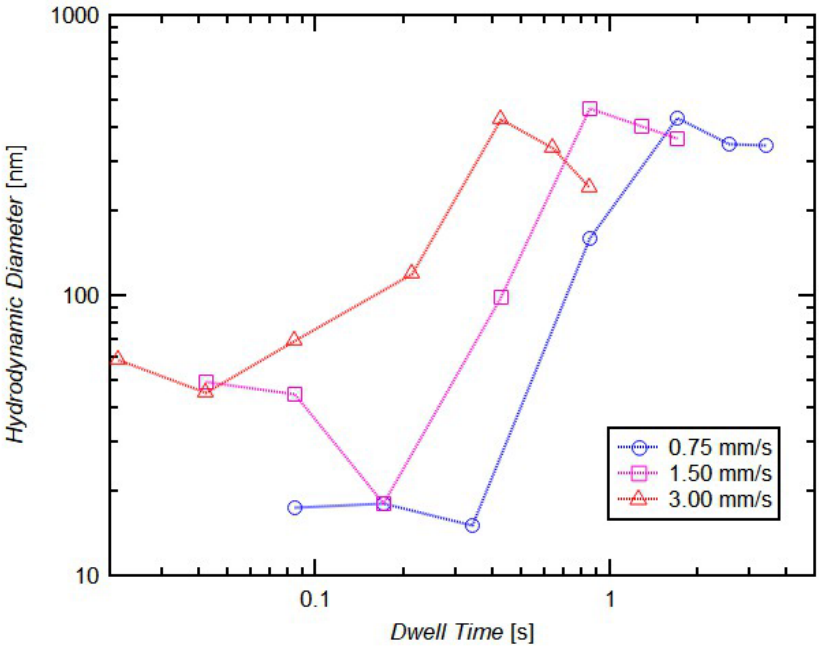

Figure 7-1: Effective hydrodynamic diameter of particles measured in DLS as a function of dwell time (s).

Clearly, by manipulating the important dimensions of measurement, new information can be revealed about the physics of the flow, potentially leading to new insights about the extensional flow field and its contribution to protein aggregation. In the following chapter, the results collected and presented in Chapter 6 are analyzed with respect to critical dimensionless parameters. Through this analysis, a potential framework for predicting protein aggregation in extensional flow fields is presented, though more testing is needed to confirm its validity.

7.2 Motivation

Flow of non-Newtonian fluids such as protein solutions can be described using dimensionless numbers to compare the relative flow of the solvent to the elasticity of the proteins. Dimensionless numbers are ratios that capture the relative influence of different physical properties of a flow. One of the most well-known dimensionless numbers is the Mach number (*Ma*), which is the ratio between flow velocity and the speed of sound.

$$Ma = \frac{V}{a} \tag{7.1}$$

At $Ma = 1$, the velocity of the flow matches the speed of sound. While this dimensionless number may be familiar to the general public, it tells us more than just how fast a jet is moving through the air. The speed of sound is dependent on the conditions of the fluid through which the sound is travelling. Therefore, the speed of sound at sea level will be different than the speed of sound high in the atmosphere. This means that the velocity required to achieve $Ma = 1$ will be different in these two conditions. However, regardless of the specific velocity of the flow or speed of sound, if a flow achieves $Ma = 1$, the physical phenomena will be similar at sea level and high in the atmosphere. By describing a flow using the dimensionless Mach number, we can make inferences about the underlying physics, do analysis, and make inferences in a general way,

without needing to consider the specific numerical conditions. In other words, Mach 1 at sea level will be the same as Mach 1 high in the atmosphere, even though the specific conditions of each location are very different.

In fact, the speed of sound can also be interpreted as the speed at which positional information is communicated through a fluid. At low velocities, and thus low *Ma*, fluid particles communicate to nearby particles, which will move to get out of the way, thus keeping the density relatively constant. At high *Ma*, the flow is moving so fast that adjacent particles can no longer move to accommodate. Thus, the fluid particles collide into each other and become compressed, rapidly changing the local density of the fluid, among other critical changes. In other words, not only does a high *Ma* tell us that a flow is moving very, very fast, it also gives us fundamental information about how important compressible effects will be to the analysis of the flow, which has significant implications for any engineering analysis or design.

Another famous dimensionless number used in fluid mechanics is the Reynold's number (*Re*). Again, a simple way of interpreting this number is that it is a way to measure how fast a fluid is moving, depending on the size and viscosity of the flow.

$$Re = \frac{\rho V L}{\mu} \tag{7.2}$$

But another way of interpreting the *Re* is the ratio between inertial forces and viscous forces, such that at high *Re* (*Re*>>1), the inertia of the fluid dominates the flow, while at low *Re* (*Re*<<1), the viscous forces are the most critical factors to consider. Because the *Re* is dimensionless, the analysis it facilitates is also generalizable to all similar flow fields, even if they do not intuitively seem similar. For example, the same Re_D, which uses a vessel diameter as its characteristic length, can be used to compare cylindrical fluid vessels like blood capillaries (~5-10 um in diameter) as

well as crude oil pipelines (~1 m in diameter). Using the *Re*, therefore, one can then infer much about the relevant physics of a flow, allowing for critical qualitative analysis leading to scaling and modelling analysis of different fluid flows.

While dimensionless numbers approaching unity (i.e. approaching 1) is generally a critical condition, values approaching unity generally indicate that multiple physical phenomena are significant. For example, in practice, compressible effects begin to be important considerations around $Ma = 0.3$. Similarly, viscous effects begin to dominate flows at $Re < 10$.

Dimensionless numbers are often used to reveal the dominant physics in a particular flow field, which can be a powerful tool for analysis, prediction, and engineering design. Therefore, to analyze and potentially generalize extensional flow fields and their contribution to protein aggregation dynamics, it is desired to develop a dimensionless framework in which the flow conditions and mechanical properties of the working fluids can be tested and evaluated, with the potential that it could lead to a predictive tool of protein aggregation.

7.3 Methods and Materials

7.3.1 Weissenberg Number (*Wi*)

The Weissenberg number (*Wi*) is defined as the ratio of elastic forces and viscous forces in a flow. At *Wi* much less than 1, the flow is dominated by viscous forces and the fluid exhibits Newtonian behavior. As *Wi* approaches unity and beyond, the elastic forces from the proteins become significant, and the fluid exhibits non-Newtonian, viscoelastic flow properties. The *Wi* is defined as the flow deformation rate multiplied by a representative time scale (Eq. 7.3). In this experiment, the extensional rate of the flow field can be chosen as the deformation rate, and the

extensional relaxation time can be used for the time scale. Therefore, as the *Wi* approaches and exceeds unity, it can potentially describe a flow in which the mechanical stretching of proteins leading to aggregation is more likely.

$$Wi = \frac{elastic\ forces}{viscous\ forces} = \dot{\varepsilon}\lambda_{\varepsilon} \tag{7.3}$$

To measure the extensional relaxation time, λ_{ε}, the BSA solutions were tested using the micro-extensional rheology technique described in Chapter 2. Approximately 10-100uL droplets of the raw, untreated sample were dispensed onto hydrophobically treated microscope slides. A platinum probe was used to penetrate the droplet and a high speed camera [NOVA R2, Photron USA INC, San Diego CA, USA] was used to capture the evolution of the liquid bridge that formed between the droplet and the probe. These images were analyzed, and λ_{ε} was recorded. The protein concentration of the solution was increased to 20, 40, and 100 mg/mL to determine the effect concentration has on extensional relaxation time. Each sample was tested 9 times at each concentration.

7.3.2 Dwell Number (*Dw*)

To non-dimensionalize the dwell time of the experiments, a *Dwell* number (*Dw*) can be proposed as the ratio between the time a protein resides in the extensional flow field and some characteristic time scale. In this case, the representative time scale is the time it would take for two individual protein molecules to interact with one another. This is defined by the diffusion coefficient of the protein, *D*, divided by the square of the mean distance between molecules of a particular concentration, L_c.

$$Dw = \frac{dwell\ time}{interaction\ time} = \frac{ND}{\dot{\gamma}{L_c}^2} \tag{7.4}$$

7.3.3 Force Ratio (f)

An intuitive framework to describe protein stretching in fluid flow fields is to calculate a force ratio, f. In this dimensionless number, the extensional force is compared to the retraction force of a molecule. The extensional force can be estimated as the viscous drag on a spherical or rod-shaped particle using Stoke's drag formula. The retraction force can be estimated as the amount of force needed to unfold a protein, which has been measured to be on the order of 100 pN (10^{-8} N). If the extensional force exceeds the retraction force and thus f is greater than unity, the protein is likely to unfold in the flow. If f is less than unity, then the molecule will likely recoil into its native state.

$$f = \frac{extension\ force}{retraction\ force} = \frac{2\pi\mu L^2\dot{\varepsilon}}{f_{unfolding}} \tag{7.5}$$

7.3.4 Péclet Number (*Pe*)

The Péclet number (*Pe*) is defined as the ratio between the advective and diffusive transport rates within a fluid flow. Typically, it is used to describe the motion of particles in a flow field. At high *Pe*, a particle is more likely to move by the flow of the surrounding fluid, whereas at low *Pe*, a particle's motion is more likely to be dominated by diffusion. Here, D is the coefficient of diffusion.

$$Pe = \frac{advection}{diffusion} = \frac{\dot{\varepsilon}L^2}{D} \tag{7.6}$$

Using the Péclet number, a *Concentration* Péclet number, Pe_c, can be defined which describes a particle's likelihood to interact with nearby particles in a flow field. The characteristic length is the distance between adjacent particles, defined by the concentration (Eq. 7.6.1). It is analogous to the inverse Dwell number, so that a high Pe_c indicates that molecules will be advected away from

each other faster than they diffuse near to each other, and a low Pe_c indicates that the particles have time to interact with one another.

$$Pe_c = \frac{\dot{\varepsilon} {L_c}^2}{D} \tag{7.6.1}$$

When applying this ratio to an individual protein molecule (Eq. 7.6.2), it can be used to describe the likelihood of a molecule's *stretch* to be dominated by the flow field or by random diffusive motion. When comparing this analysis to the *Wi*, a new time scale emerges (L^2/D), that may provide information about the flow field threshold that needs to be crossed to achieve aggregation. In essence, then, the *Wi* and Pe_m (molecular Péclet number) may be equivalent, though their interpretations are subtly different.

$$Pe_m = \frac{advective\ stretching}{diffusive\ retraction} = \frac{\dot{\gamma} {L_m}^2}{D} \tag{7.6.2}$$

In this case, the characteristic length is that of the molecule itself. A low Pe_m would represent a flow in which any conformational changes to a protein constituent are dominated by random fluctuations, whereas a high Pe_m would represent a flow in which the molecule is likely to be stretched by the surrounding fluid. Thus, this Pe_m is a representation of the flow field and its influence over a particular molecule and is independent of the fluid's concentration (Figure 7-2).

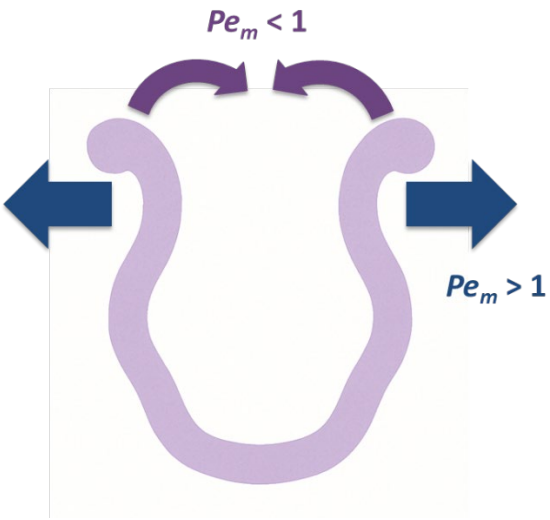

Figure 7-2: Illustration of molecular Péclet number. Pe<1, flow field is not strong enough to cause conformational changes in protein molecule. The protein is either too small, or the flow field is too weak to stretch the molecule. (Right) Pe>1, extensional field stretches protein molecule faster than it is able to recoil back on itself. This behavior may be due to the size of the protein, or the strength of the field.

7.4 Results

7.4.1 Wi vs. Dw

We have hypothesized that protein aggregation can be characterized with respect to the *Wi* and *Dw*, such that the aggregation behavior can be predicted depending on the *Wi* and *Dw* of the process in question. As the *Wi* increases, the magnitude of extensional strainrate ($\dot{\varepsilon}$) or the extensional relaxation time also increases. In other words, a high *Wi* will indicate a higher likelihood of aggregation. As *Dw* increases, the likelihood that two molecules will interact with one another also increases, giving more opportunity for aggregation to occur.

Using this framework, we can non-dimensionalize the experimental parameters used in Chapter 6 into their respective *Wi* and *Dw* numbers (Figure 7-3). The extensional relaxation time, λ_ε, of this BSA solutions was approximately 88 us. The extensional strain rates, $\dot{\varepsilon}$, for the 0.75, 1.5,

and 3.0 mm/s phases were 1440, 2880, and 5505 s^{-1}, respectively. Therefore, the Wi for each phase was 0.126, 0.253, and 0.484.

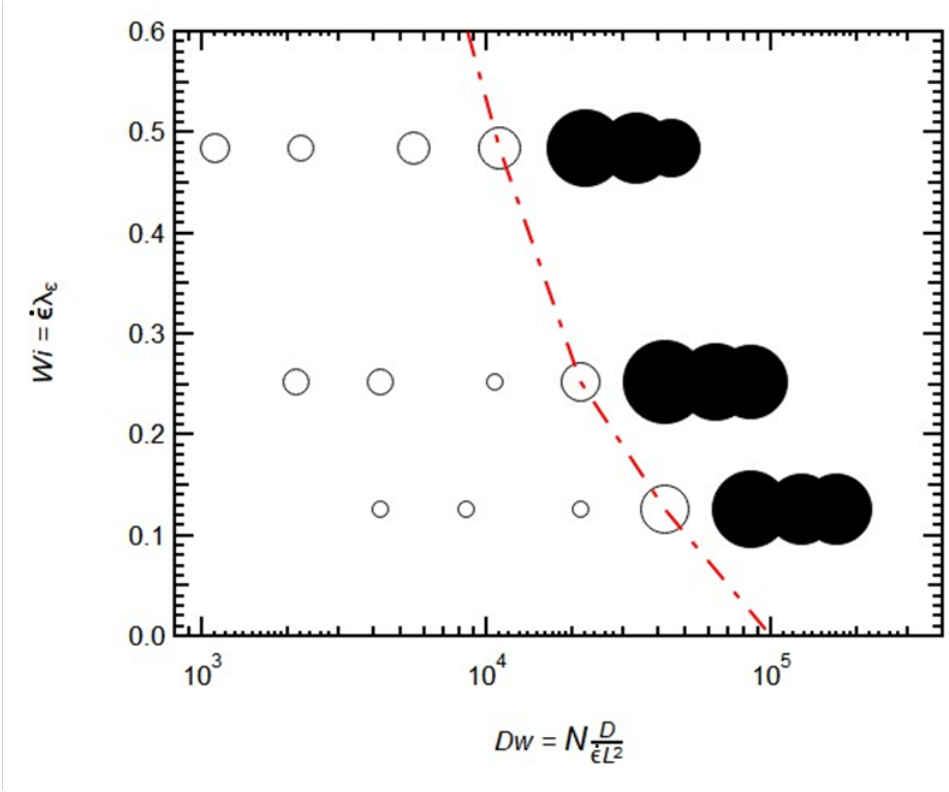

Figure 7-3: Results from Chapter 6, figure 3, non-dimensionalized to the Wi vs. Dw framework.

In Figure 3, distinct aggregation regimes become clear. In regime I to the left of the red dotted line, aggregation begins to be detected and a period of growth is observed, but no precipitation of particles is observed. Regime II, indicated by the dotted line in Figure 3, is a transition region, where suspended particles are quite large, but visible precipitation is inconsistently observed. Finally, in regime III to the right of the dotted line and beyond, precipitation is consistently observed and the effective diameter of the remaining suspended particles begins to shrink as the larger particles are recruited into the precipitating aggregates.

This framework would match intuition, as the intensity of the flow field increases, less time is required to achieve the same aggregation results. Conversely, as the intensity of the flow field decreases, the relative time required to achieve similar aggregation increases. This framework would also suggest that the results can be manipulated by increasing extensional relaxation time to increase the Wi and achieve enhanced aggregation for any particular flow field. This suggestion is explored with the results of the increased concentration tests.

7.4.2 Increased Extensional Relaxation Time

As seen in the Chapter 6, increasing the concentration of the test solutions dramatically reduces the number of runs required to achieve precipitated aggregation. BSA was chosen for this study because, like tau, it is not known to self-aggregate[78,80]. Therefore, with little inter-molecular interaction between the proteins, its extensional rheological behavior challenges the limits of our microextensional rheological technique[19,140]. While a difference in extensional rheology was measurable, the change from 20 to 100mg/ml solution did not yield significant increases in extensional relaxation time as was expected and observed with other proteins and polymers. Originally, testing was performed using a BSA concentration of 10mg/mL (152 uM). This solution exhibited an extensional relaxation time of approximately 88us. When the concentration of BSA was increased to 20mg/mL, 40 mg/mL, and 100 mg/mL the lambda_e increased to 131, 155, and 180 us, respectively (Figure 7-4).

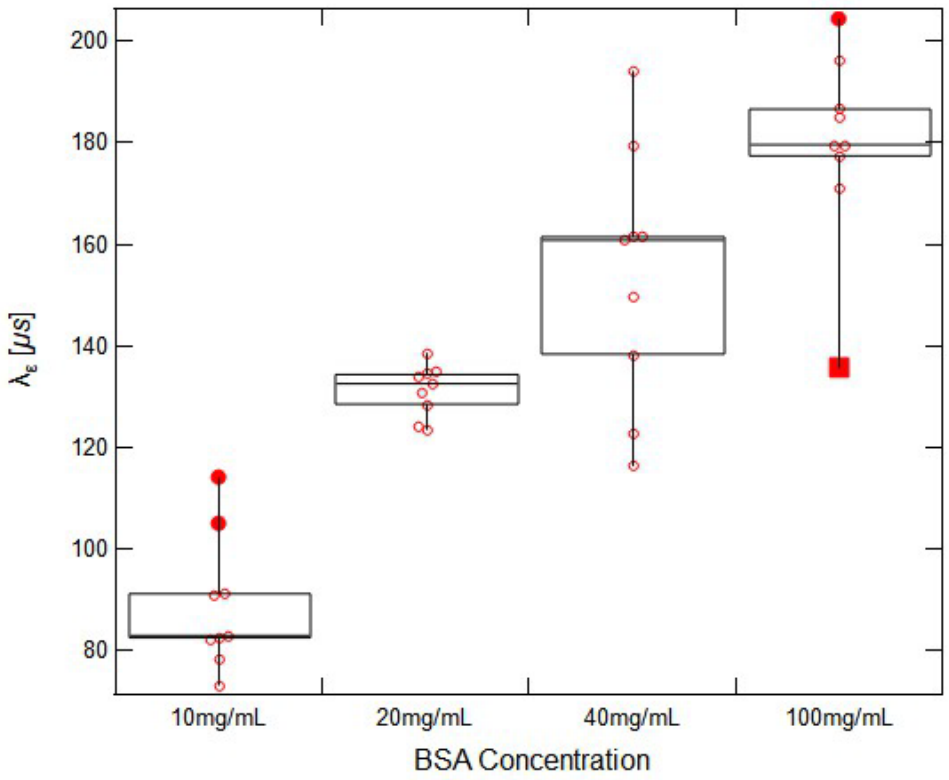

Figure 7-4: Extensional relaxation time, λ_ε, as a function of BSA concentration.

In the previous framework, one would predict that the increased extensional relaxation time would result in an enhanced aggregation behavior of the protein solution. However, when non-dimensionalized in the Wi vs Dw framework (Figure 7-5), a unique behavior is observed in which the aggregation based on dwell time matches well across experimental parameters, but the results are independent of the extensional relaxation time.

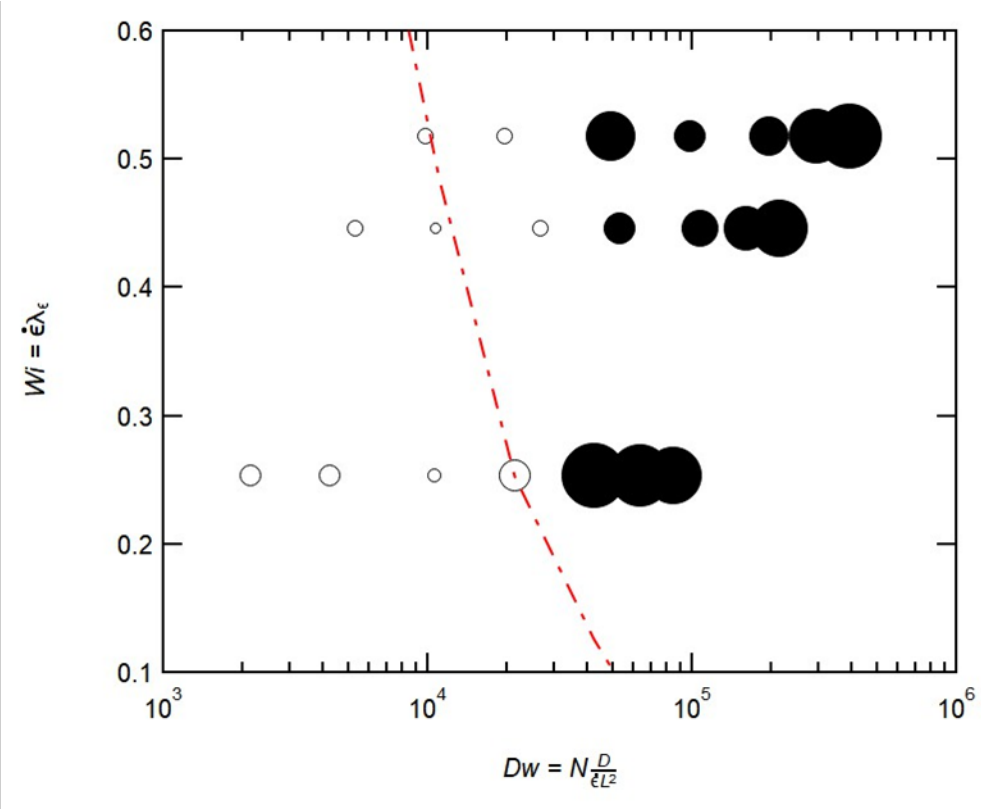

Figure 7-5: Wi vs. Dwell of different concentrations

While this further supports that the dwell time is a critical consideration in being able to predict aggregation behavior, it suggests that the extensional relaxation time of the fluid is not a critical parameter. Therefore, another time scale is desired that may be better suited to explain the behavior of these aggregation experiments.

7.4.3 Pe vs. Dw

For BSA, the characteristic length of the molecule is 8nm, and the diffusion coefficient D_{BSA} is $6x10^{-11}$ m^{-2}/s. When analyzing the experiments presented in Chapter 6, extensional rates of 1440, 2880, and $5505s^{-1}$ produce Pe_m numbers of approximately 1.5e-3, 3e-3, and 6e-3, respectively.

When these values are multiplied by the number of passes through the flow field per experimental run, the Pe_m number begins to approach unity after only 100 passes (Figure 7-6).

$$Pe_m = N\frac{\dot{\gamma}{L_{BSA}}^2}{D_{BSA}} = 100\frac{(2880)(8e-9)^2}{6e-11} = 0.307 \tag{7.6.3}$$

While the effect is still relatively small, this Pe_m value indicates that an extensional flow field of this intensity may have a significant influence over the conformation of the proteins within the fluid. As either the number of runs or the extensional rate of the flow field is increased, the stretching effect the flow has on the molecule becomes more pronounced.

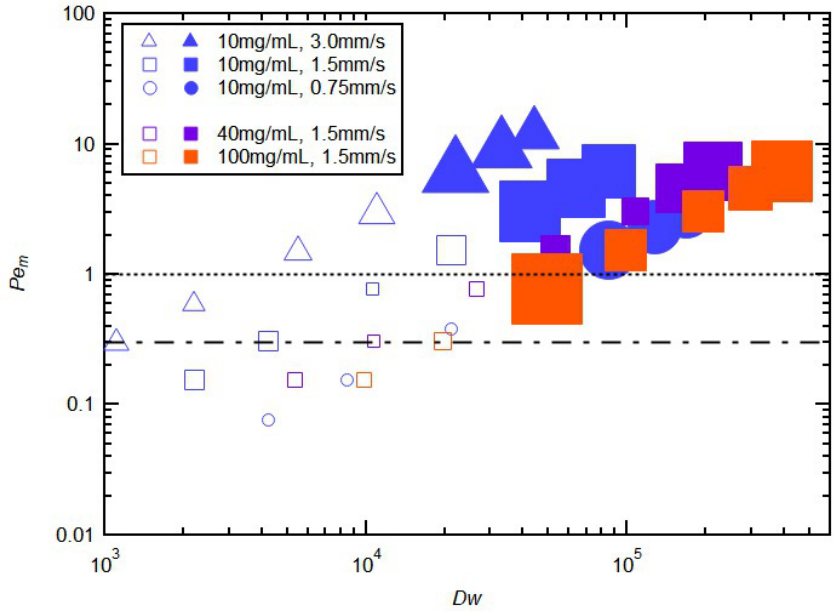

Figure 7-6: Collected data from Chapter 6 displayed as Pe_m vs Dw. An arbitrary threshold was placed at Pe_m=0.3, below which aggregation was relatively low. Above this line, aggregation began to be detectible using DLS. As Pe_m approaches 1, visible precipitation starts to emerge.

7.4.4 Comparison of BSA and Tau

Force Ratio

Comparing the force ratios, *f*, for BSA and tau, one finds that because BSA is a small molecule, the force ratio due to Stoke's drag on the particle is very small. Since *f* scales with the squared length of the molecule, the relatively large tau molecule achieves force ratios orders of magnitude larger than BSA. However, the force ratio in both instances is very small, when compared to an approximate unfolding force of 100 pN. For the conditions induced by the reciprocal extensor apparatus, the f_{BSA} is estimated as $3x10^{-6}$ and f_{tau} is estimated to be $6.5x10^{-4}$. Thus, the viscous drag alone is not likely to dominate the unfolding mechanics of the protein, though it may contribute in a small way with a more accurately defined unfolding force.

Concentration Péclet

The diffusion coefficient of BSA is relatively high, and the effective length is relatively small, which would indicate that BSA is able to resist the flow deformation relatively well in this framework. For molecules with lower diffusion coefficients, the effect may be more pronounced. The diffusion coefficient of BSA is $6x10^{-11}$ m^2/s, while the diffusion coefficient of tau is $3x10^{-13}$ m^2/s. Therefore, for a concentration of 150 uM, the Pe_c for BSA and tau are 0.023 and 4.6, respectively. This would imply that the critical concentration to enhance interaction between molecules would be much higher for tau than for BSA, which is relatively more mobile.

Molecular Péclet

The relative size of the molecules will also be critical in this framework. Tau, for example, has a length of roughly 50 nm, while BSA is relatively small, about 8 nm. Combined with the different diffusion coefficients, with even a small extensional rate, this means that tau's Pe_m approaches unity after relatively few passes through the flow field.

$$\frac{{L_{BSA}}^2}{D_{BSA}} = 10^{-6}s \qquad \frac{{L_{tau}}^2}{D_{tau}} = 0.01s \tag{7.6.4}$$

In other words, for a molecule such as tau, it may be orders of magnitude more likely to aggregate than BSA (Figure 7-7). Therefore, even though the aggregation achieved in the previous chapter was done using an extension rate that was not physiologically relevant, this approach shows promise that flow fields that may contribute to the aggregation of tau may be possible in the human body.

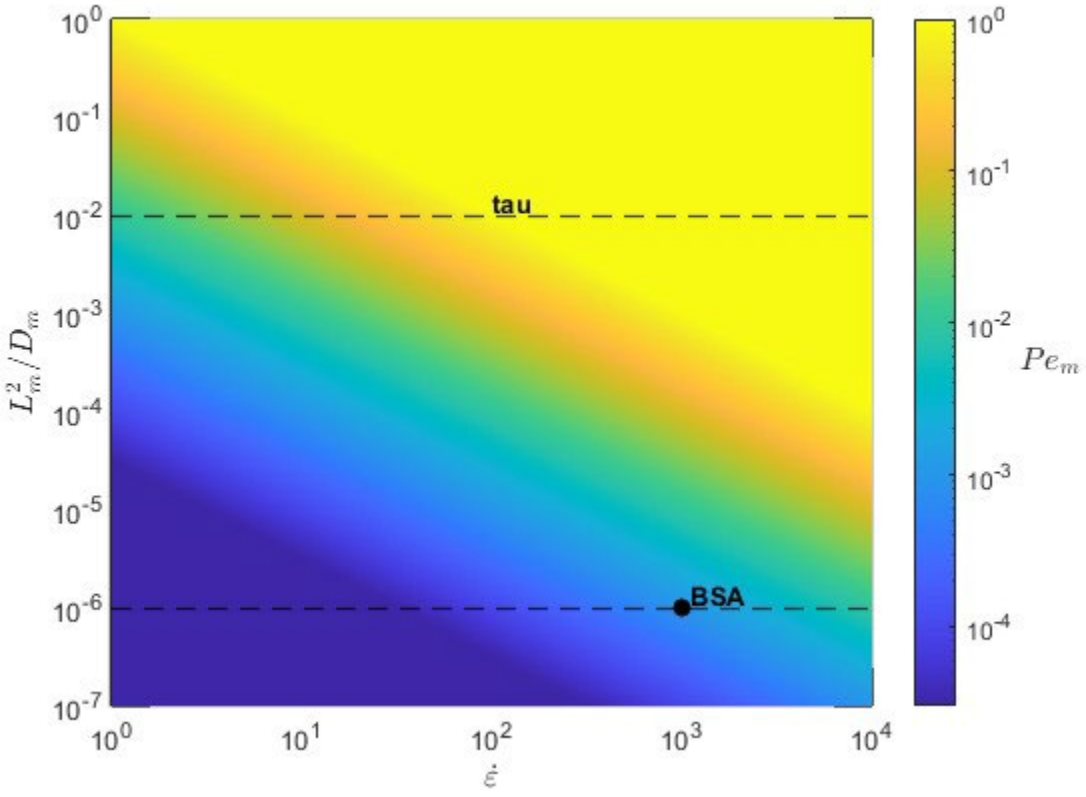

Figure 7-7: Heatmap of Pe_m for any molecule as a function of L^2/D vs $\dot{\varepsilon}$. The experiments performed in chapter 6 are represented approximately as the black dot labeled BSA on the lower dotted line. Any experiments with tau protein would exist somewhere on the upper dotted line.

7.5 Discussion

7.5.1 Molecular Properties and Concentration

It can be interpreted that there are two versions of the *Pe* that are relevant here, the Pe_m, as discussed, and another dependent on the concentration of the fluid, Pe_c. This Pe_c uses the distance between protein molecules as the characteristic length. In this case, if advection dominates the flow, the proteins do not have time enough to interact with one another. If diffusion dominates, then there is ample opportunity for adjacent proteins to interact with one another. In fact, *Dw* presented in Figure 7-5 and Figure 7-6 can be rearranged to be $Dw = N/Pe_c$.

Both Pe_m and Pe_c represent important, though different, flow parameters that could be critical for predicting protein aggregation. In this framework, there are two stages of protein aggregation, the molecular stretch that denatures the protein and initiates aggregation, and the interaction between proteins that facilitate continued aggregation. In this framework, Pe_m would predict the initiation of protein aggregation while Pe_c would predict the aggregation propagation. An interesting observation can be made on Figure 7-6, which shows that as the Pe_m approaches unity ($Pe_m > 0.3$), significant aggregation is observed, indicated by the growing hollow circles. This would indicate that protein denaturation is indeed initiated by the flow field, but time is needed for it to be detectable using these methods.

Both Pe_m and Pe_c are influenced by the intensity of the extensional field, but Pe_m carries more information about the molecular mechanics, while Pe_c conveys information about the crowding conditions caused by the concentration of the fluid. Thus, a high Pe_m may induce a protein to denature, but if the Pe_c is too high, protein aggregation may not propagate. Similarly, a critical

concentration may provide a relatively low Pe_c, but if the flow field is not strong enough to surpass a critical Pe_m, then aggregation will not be enhanced by the flow.

7.5.2 Intrinsically Disordered Proteins

While this analysis shows promise that this framework can be adapted to analyze and predict the aggregation behavior of proteins in general, the exact theory will need to be confirmed. This time scale introduced in the Pe_m is based on the diffusion coefficient of the protein, assuming that this property also quantifies how a protein either stretches or returns to its native state due to random fluctuations. For a tightly bound molecule with a well-defined three-dimensional structure like BSA, diffusion may not be the driving force behind conformational changes. For intrinsically disordered proteins (IDPs) like tau, however, it may be reasonable to assume that conformational changes are significantly influenced by random fluctuations due to Brownian motion.

Similarly, the tightly bound BSA's structure is the result of hydrogen bonding between multiple locations on the protein. Therefore, the unfolding force may be higher for BSA than for an IDP like tau, which has relatively few hydrogen bonding sites. If so, the force ratio resulting from any particular flow field would be higher for tau than for BSA, indicating a higher likelihood to denature and aggregate.

That aggregation was achieved in the BSA experiments of Chapter 6 suggests that one or more of these critical parameters were surpassed by the induced flow fields. Given this analysis, therefore, we would expect the behavior of an IDP like tau to be enhanced under similar conditions, as the critical parameters would be more easily achieved. Therefore, an investigation into the response of IDPs like tau to varying flow fields may reveal critical Pe_m and f parameters that could be used to predict protein aggregation.

7.6 Summary

In this chapter, the data collected and presented in Chapter 6 were analyzed using non-dimensional parameters to attempt to reveal dominant physics of the flow and its contribution to protein aggregation. Though the data does not support the initial hypothesis that the extensional relaxation time will be a critical parameter, this analysis has potentially revealed another time scale that may be more relevant and useful in predicting the initiation and propagation of protein aggregation. Using the f, Pe_c, Pe_m, and Dw, a new framework is revealed that has the potential to explain the physics underlying physiological protein aggregation.

Though incomplete, this framework of characterizing protein aggregation suggests that the aggregation behavior can be manipulated by either the intensity of extensional flow, duration of exposure to extensional flow fields, or by changing the stretching timescale of the protein within the solution. While initial analysis shows promise for this framework, much more testing is needed to confirm its validity in the prediction of protein aggregation.

IDPs are molecules that may be more aggregation prone, given their lack of well-defined three-dimensional structure. In this framework, IDPs like tau would be much more likely to denature and aggregate in a given flow field compared to BSA. That BSA aggregation was achieved and demonstrated in Chapter 6, we would predict that under similar conditions, tau will not only aggregate, but its aggregation behavior would be further enhanced. In the next chapter, experiments performed to investigate this prediction are presented.

Chapter 8 : Tau Aggregation

8.1 Introduction

From the outset of this research, the goal has been to study the protein aggregation dynamics of tau, to better understand the link between mechanical head injury and the progression of the pathological tau aggregation observed in CTE. In this chapter, results of preliminary testing of tau is presented, paving the way for future research that could further enhance our understanding of this important and significant protein and its associated diseases.

8.2 Motivation

Tau is a naturally occurring IDP that helps stabilize microtubules in neuronal axons. Tauopathies are a class of neurological disorders characterized by the misfolding and abnormal aggregation of tau. Because of tau's significant links to neurodegenerative disease like Alzheimer's, Parkinson's, and CTE, much research has been devoted to the clinical and biochemical study of different tauopathies. To date, there are nearly 30 identified distinct tauopathies, differentiated in part by what tau isoform is found within a patient's brains[3].

However, tau aggregation is at least partially a response to mechanical stimuli, but not much is known about what triggers or maintains tau aggregation. While much research has been devoted to the effect of different chemical stressors on tau aggregation[144–146], relatively little has been focused on mechanical stressors of tau aggregation. In fact, most tau aggregation experiments incorporate a mechanical stimulus to initiate tau aggregation, but these mechanical stimuli are not well defined or controlled[147–155]. Recent studies have shown certain proteins can be made to

aggregate under mechanical stresses and strains, including Amyloid Beta, which, like tau, is associated with many neurodegenerative diseases[156]. Understanding the aggregation behavior of tau in response to mechanical stimuli will be critical to the understanding and eventual prediction and diagnosis of different tauopathies.

8.3 Methods and Materials

8.3.1 Tau

Two types of tau were used in this experiment, both received from Dr. Ori-McKenney at UC Davis. Bacterially expressed truncated tau (dGAE) and phosphorylated tau expressed in fruit flies and tagged with superfolder green-fluorescent protein (sf-GFP) were frozen and stored in -80C deep freeze prior to testing. In total, 40uL of 5.6 mM (~54mg/mL) dGAE tau and 20uL of 253 uM (4.6mg/mL) sf-GFP tau were used in this experiment. The concentrations were very high to increase the likelihood of achieving visible and measurable aggregates.

dGAE tau is a particularly significant isoform of tau because of its demonstrated ability to produce fibrils that are identical to pathological fibrils found in diseased brains. dGAE by itself has been shown to produce aggregated fibrils that are identical to fibrils found in Alzheimer's disease, and with the addition of salt, exhibit a characteristic form that is identical to fibrils found in CTE[153,157]. Phosphorylated tau is also associated with pathological aggregation, as the pattern of phosphorylation on the molecule may decrease the binding affinity of tau to the microtubule[158].

The samples were thawed in a 4C refrigerator overnight prior to dilution. Once thawed, the samples were diluted using MilliQ water passed through 220nm syringe filters. dGAE tau was diluted 80x in order to achieve multiple runs while maintaining the minimum volume required to

test in DLS (70uM, ~800uL each). The sf-GFP was diluted 40x to achieve a representative test run through the reciprocal extensor (6.3uM, ~800uL).

8.3.2 DLS

At these concentrations, the untreated samples were very different, with the dGAE being transparent and sf-GFP being turbid and translucent (Figure 8-1). Therefore, while the dGAE could be measured at the concentrations listed above, prior to DLS analysis, the sf-GFP had to be even further diluted 50x to get valid readings.

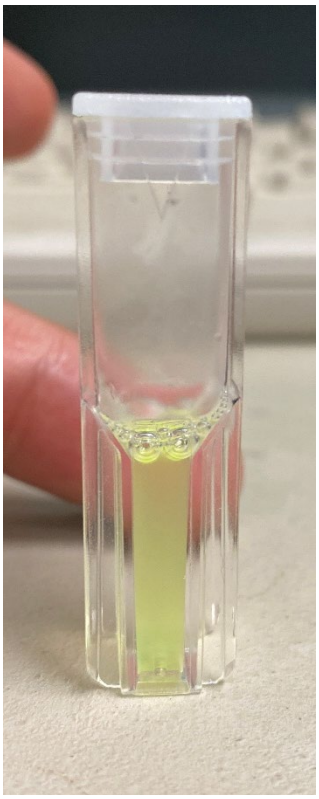

Figure 8-1: Turbidity of sf-GFP tau sample.

8.3.3 Extensor Treatment and Control

Two samples of dGAE were treated in the reciprocal extensor described in Chapter 3. The input plunger velocity was set to 1.5mm/s, for a maximum extensional rate of 2880 s^{-1}. One sample was treated with 1500 passes through the extensor, and the other was treated with 250 passes. In both experiments, an untreated control sample was placed at rest next to the extensor. All experiments were conducted at room temperature.

8.3.4 Microscopy

After treatment on the reciprocal extensor, samples were observed for precipitation of visible aggregates. Samples were dispensed into aliquots and mixed with 800uM ThT and allowed to sit at 4C overnight to allow for penetration of the dye into any aggregates. 10uL of the sample pellet that had settled at the bottom of the aliquot was dispensed onto a microscope slide and viewed using a Nikon eCFP filter cube at 2x, 10x, and 20x magnification.

8.4 Results

8.4.1 dGAE

DLS

dGAE tau at this concentration showed evidence of spontaneous aggregation, even prior to treatment with the reciprocal extensor. Upon measurement on DLS, each successive test showed an increase in effective hydrodynamic diameter, indicating a spontaneous aggregation of the suspended proteins (Figure 8-2).

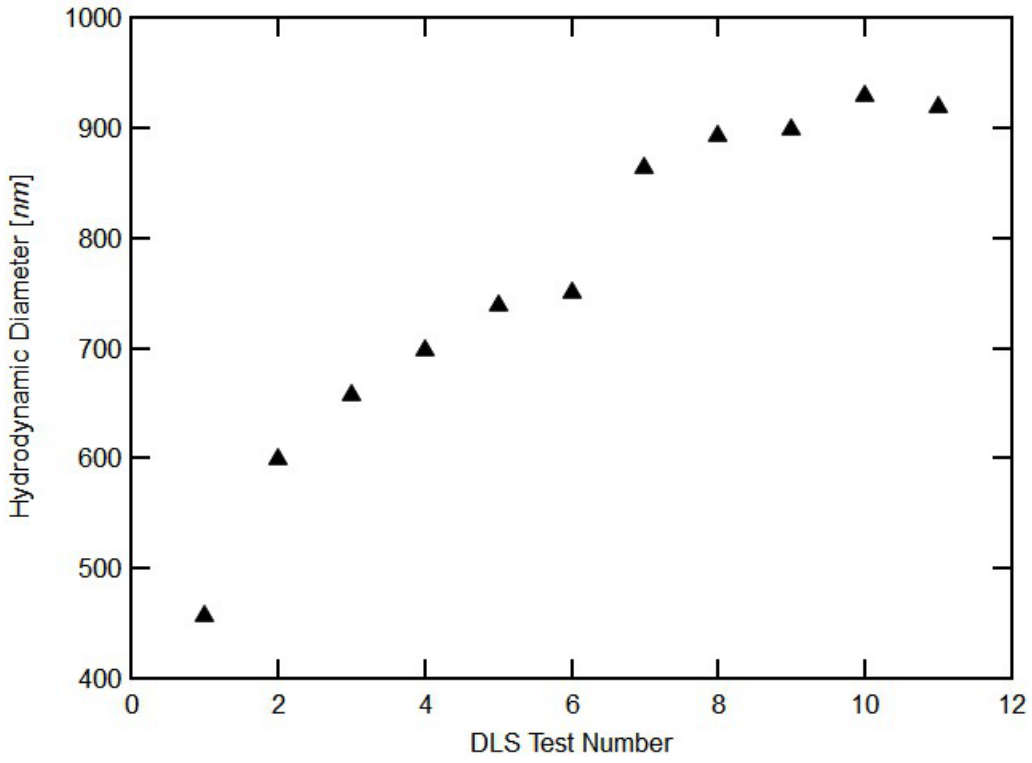

Figure 8-2: DLS results of raw, untreated dGAE tau. Each data point was recorded between two and five minutes after the previous data point.

After treatment of 1500 runs through the reciprocal extensor, visible aggregates were observed, and the DLS effective diameter measurement decreased, consistent with the results of BSA precipitation presented in Chapter 6. However, over the same period, the control sample increased in effective diameter, though no visible particulate was observed (Figure 8-3).

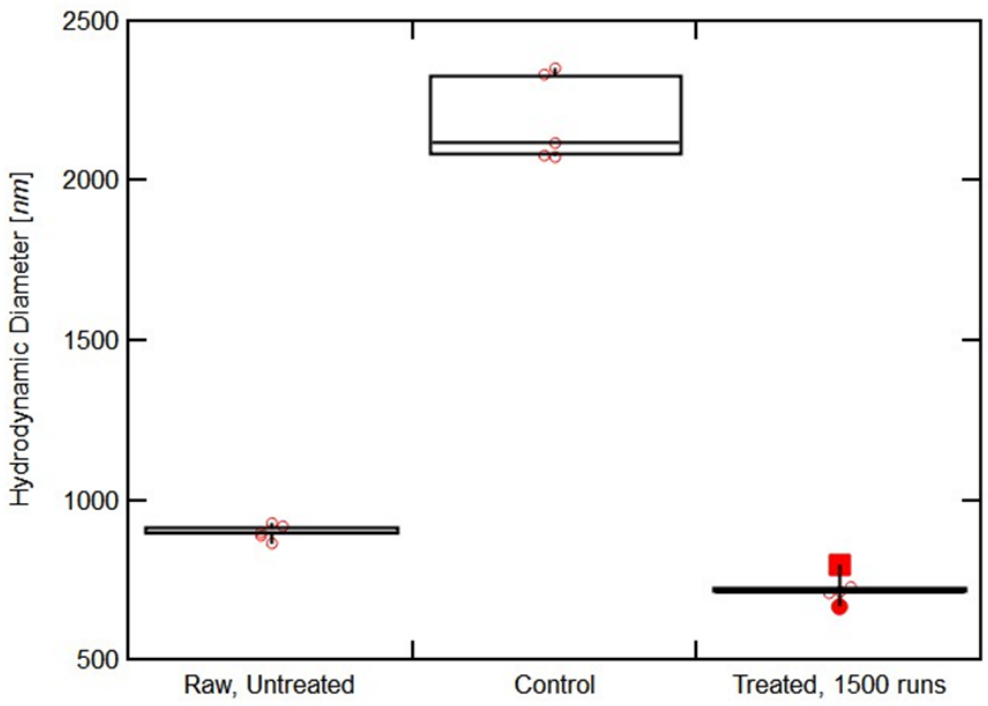

Figure 8-3: DLS results of dGAE tau experiment. Both raw and control samples were not subjected to reciprocal extensor treatment. The treated sample was subjected to 1500 runs through the reciprocal extensor at 1.5mm/s.

In the second experiment, two samples of dGAE were prepared as above, though at the time of treatment, both had been resting in 4°C for more than 48 hours while the tests described above were executed (Figure 8-4). The sample that was treated with 250 runs through the reciprocal extensor again exhibited visible particulate precipitation, coupled with an apparent decrease in effective diameter. In the control, though no particulate was immediately visible, the apparent effective diameter of the suspended particles also decreased when compared to the measurements made prior to treatment.

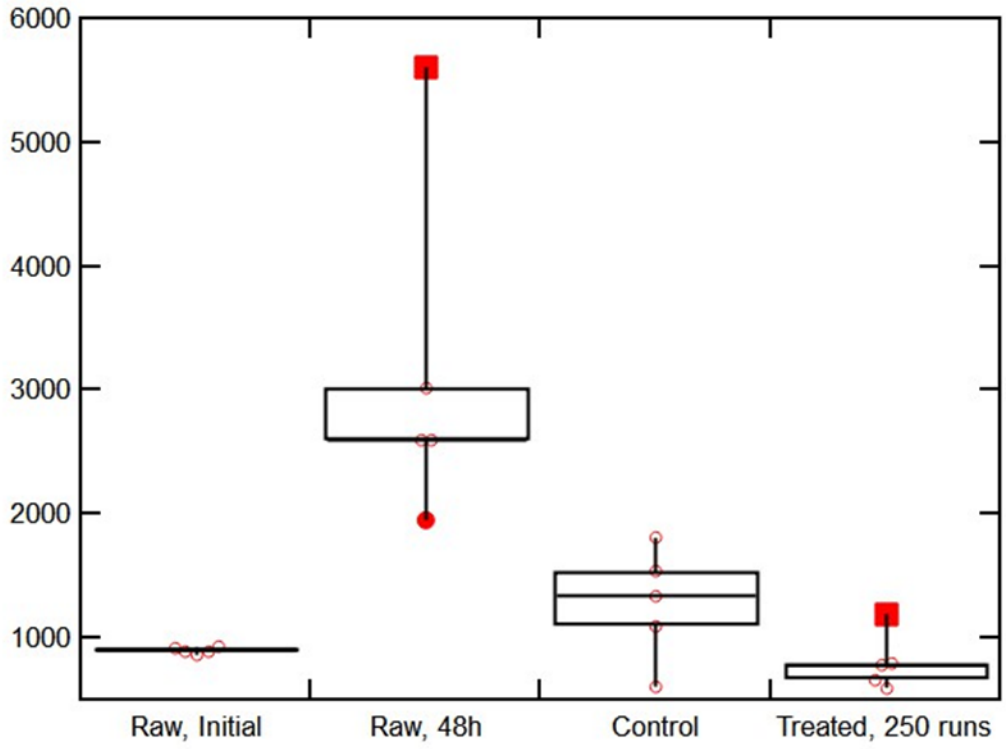

Figure 8-4: DLS results of dGAE tau. Initial raw results from Figure 8-3 are displayed as reference. Both raw and control samples were untreated in the reciprocal extensor. The treated sample was subjected to 250 runs through the reciprocal extensor at 1.5mm/s. Note that samples were thawed and rested at 4℃ for 48 hours while previous testing was performed.

Microscopy

Upon inspection with fluorescent microscopy, significant aggregation was observed within the sample that had precipitated out of solution. These structures fluoresced using the eCFP filter, again confirming that the precipitated aggregates contained amyloid formations, pathologically relevant protein structures (Figure 8-5).

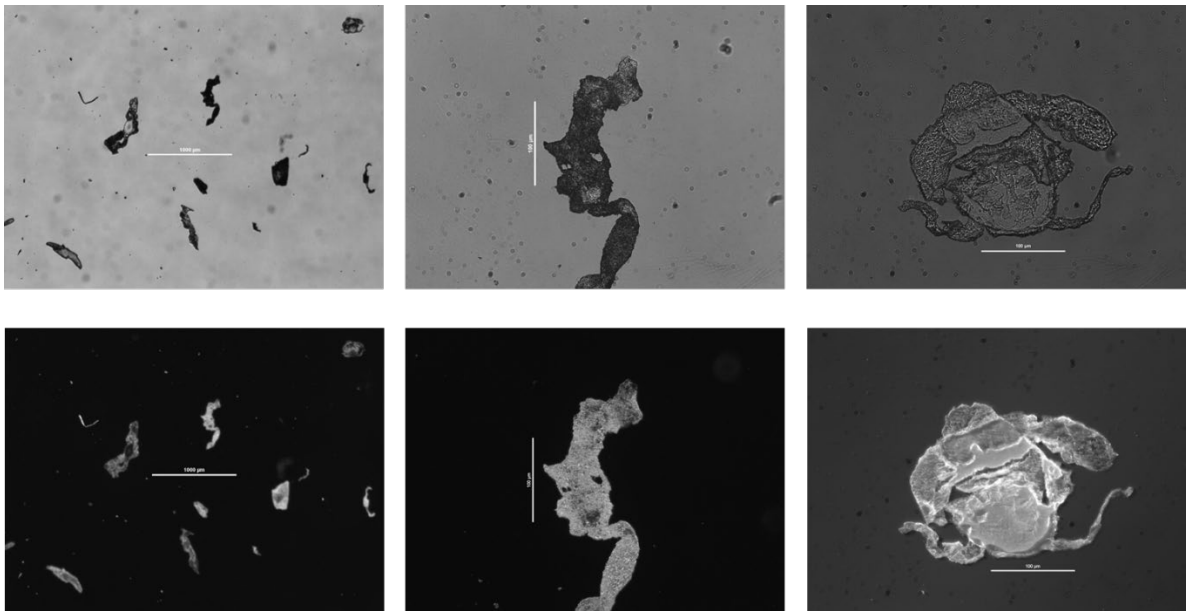

Figure 8-5: Fluorescent aggregates of dGAE tau tagged with ThT resulting from passage through 1500 runs in the reciprocal extensor. Top row is brightfield illumination, bottom row is fluorescent illumination using ECFP Nikon filter cube. (Left) 2x magnification showing representative aggregates of dGAE, scale bar 1000 um. (Middle and right) 20x magnification of representative aggregates, scale bar 100 um.

Additionally, these tests exhibited unique aggregation morphology that was not observed in BSA testing. While much of the aggregation presented as amorphous blobs, some structures exhibited a more ordered structure, resembling fibers or ribbons (Figure 8-6).

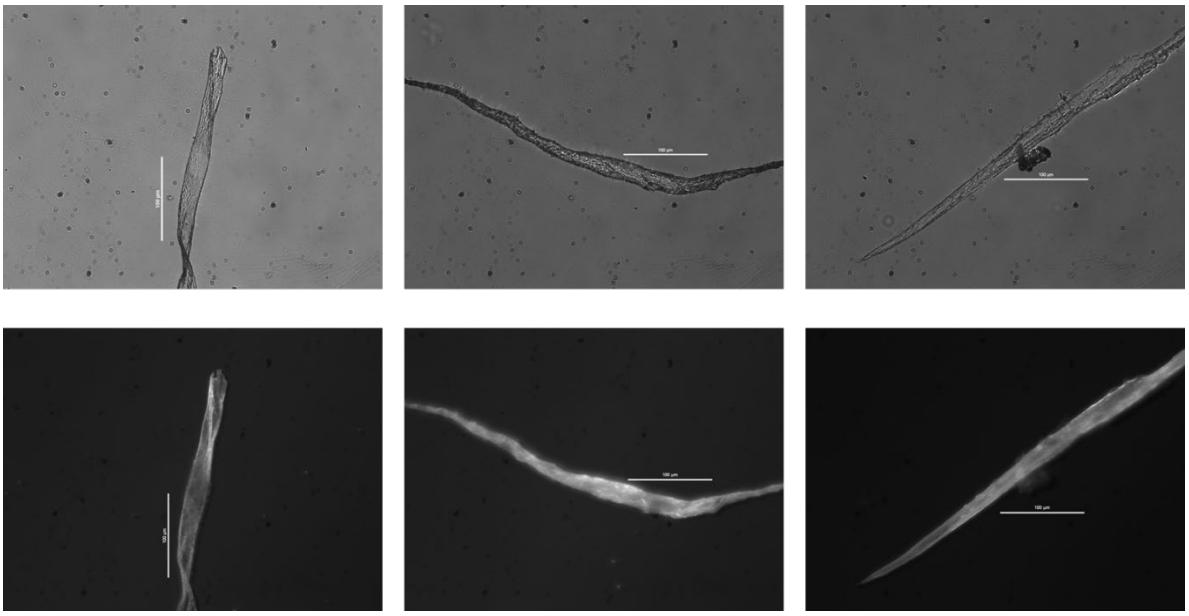

Figure 8-6: Aggregates with unique morphology, scale bar 100 um.

These structures were observed in both treated samples, 1500 and 200 runs (after 48 hours at 4C). Additionally, protein precipitates were also observed in the second control sample, which had rested for 48 hours prior to testing and also exhibited decreased effective diameter in DLS measurement (Figure 8-7).

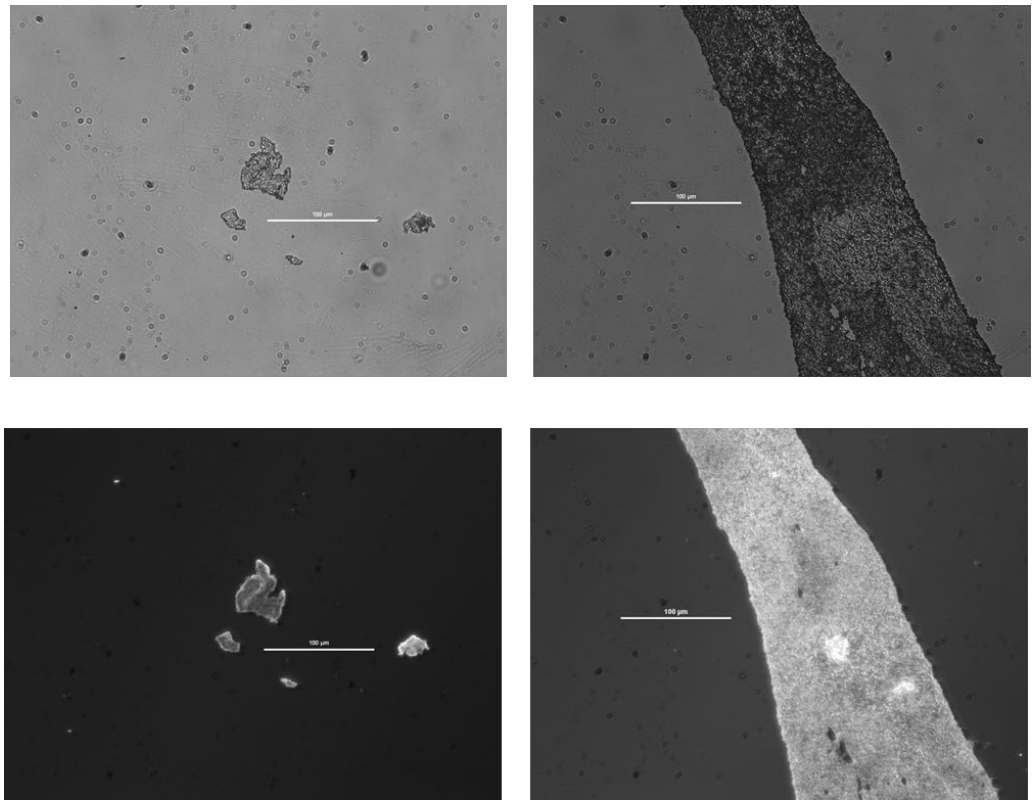

Figure 8-7: (Left) Comparison of control sample, which had been resting for 48 hours. (Right) Treated dGAE aggregates after 200 runs through reciprocal extensor.

8.4.2 sf-GFP

As mentioned above, the untreated sf-GFP was turbid and translucent, different from the BSA or dGAE samples previously tested. Therefore, the sf-GFPs was tested in DLS by extracting a small, 16uL sample and diluting it to 800uL. The undiluted sample was tested in the extensor, as pictured below. After treatment in the reciprocal extensor, the turbidity of the sample was greatly reduced and visible particulate was observed, indicating that the suspended particles precipitated out of solution as a result of the treatment (Figure 8-8).

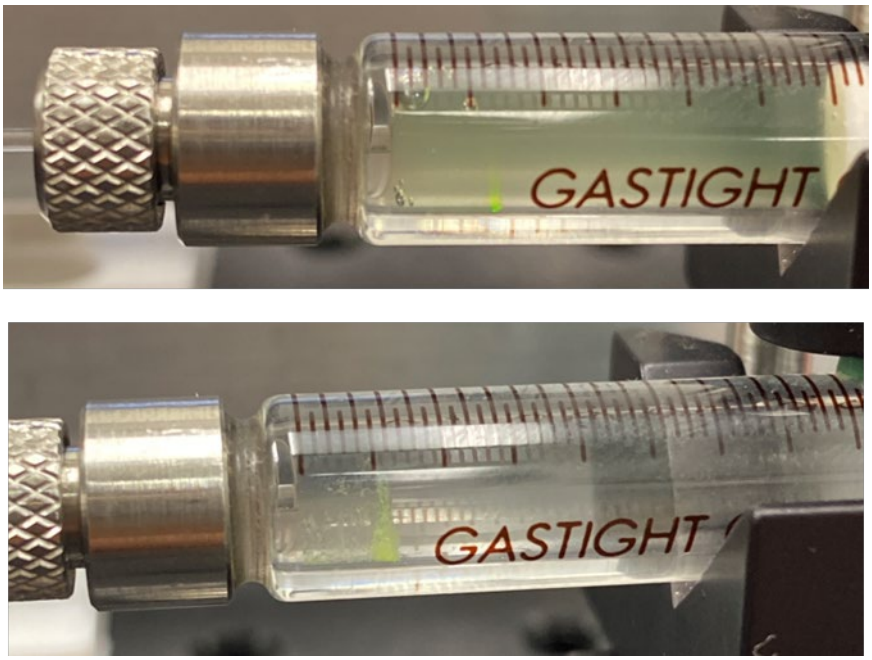

Figure 8-8: Turbidity decrease of sfGFP tau. At beginning of test (top), sfGFP tau solution was turbid and translucent (see Figure 8-1). During the test, precipitation began to be observed. By the end of the test (bottom), solution was clear, with green precipitate observed.

DLS

Prior to treatment, 16uL of sample was diluted 50x to 800uL and tested on the DLS (Figure 8-9). The resulting effective diameter was 295nm. This sample was capped and kept in the microcuvette at rest as a control while the rest of the sf-GFP tau was being treated in the reciprocal extensor. After treatment, another 16uL of the treated sf-GFP was sampled and diluted to 800uL. While the effective diameter was relatively unchanged, 370 nm, the control effective diameter grew to ~1000nm. While this growth is not as rapid as was observed with the dGAE, it is not unexpected given that phosphorylated tau such as this is known to self-aggregate more readily than non-phosphorylated tau.

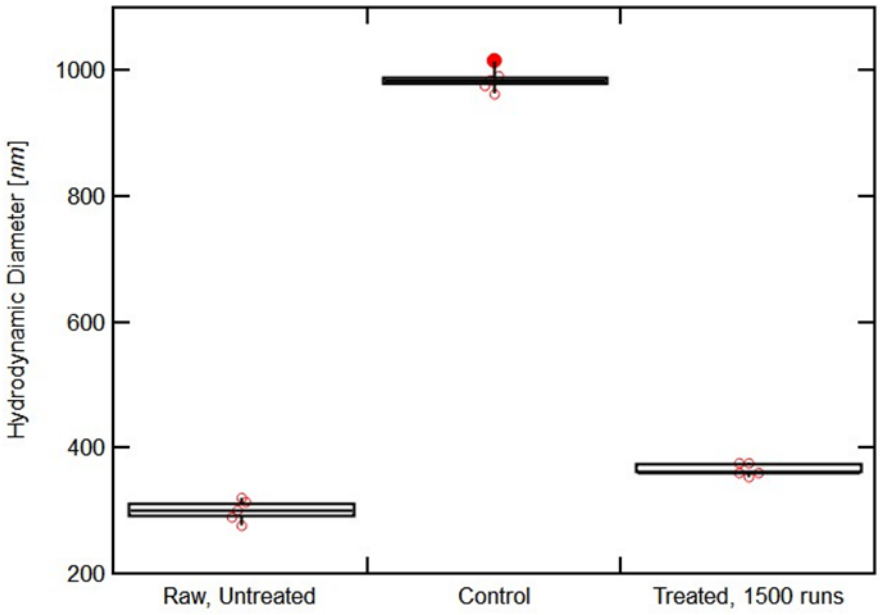

Figure 8-9: sfGFP tau DLS results. The control sample showed a dramatic increase in hydrodynamic diameter, consistent with other self-aggregating protein behavior (Figure 8-3). When treated, diameter increased a smaller amount, coupled with observed precipitation.

Microscopy

Under fluorescent microscopy, structures of aggregation were observed that were again unique to this protein and different from both the BSA and dGAE tested previously (Figure 8-10). Significantly, fibrillar structures were observed in many of the aggregates (Figure 8-11).

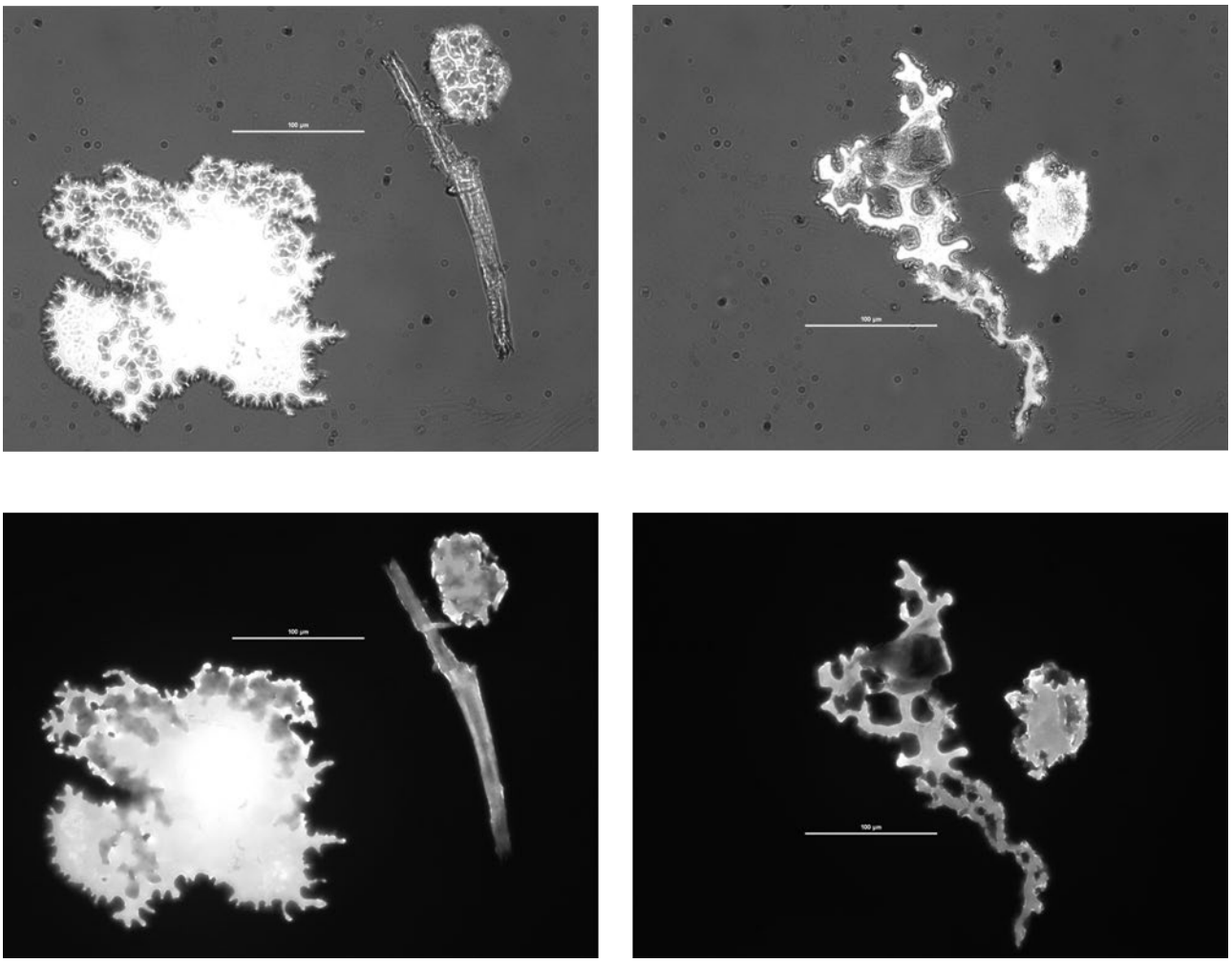

Figure 8-10: sfGFP aggregates. Top row: brightfield; Bottom row: eCFP filter. Scale bars 100 um.

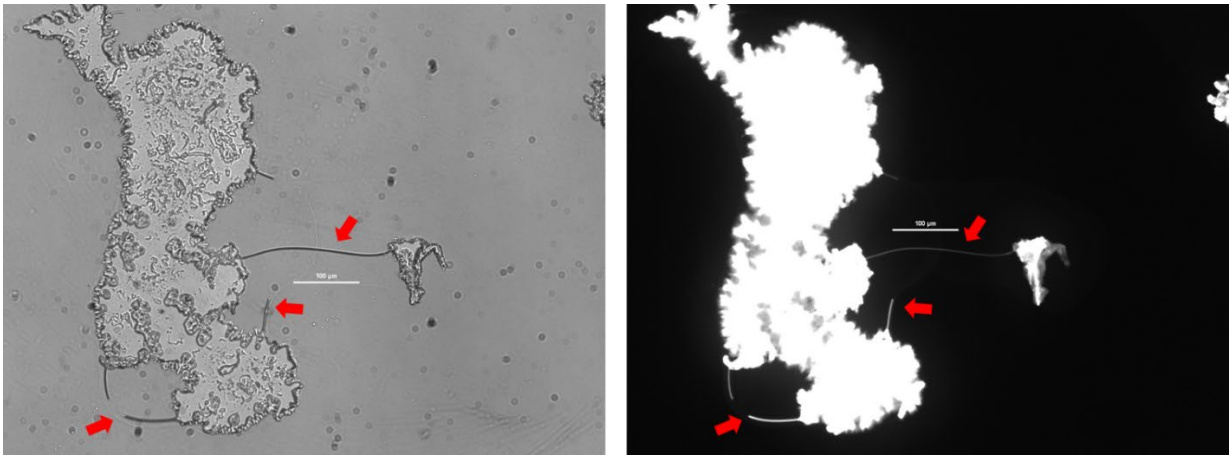

Figure 8-11: Fluorescent fibrillar structures observed in sfGFP tau (red arrows). Scale bars 100 um.

The sf-GFP fluorescence overlapped with the ThT fluorescence, so the fluorescent intensities are far greater than in the other protein structures, but this fluorescence again confirms that the aggregated particles are indeed the proteins that were previously suspended in the test solutions. If analyzed closely, structures can be observed that fluoresce with ThT and not the sf-GFP (Figure 8-12).

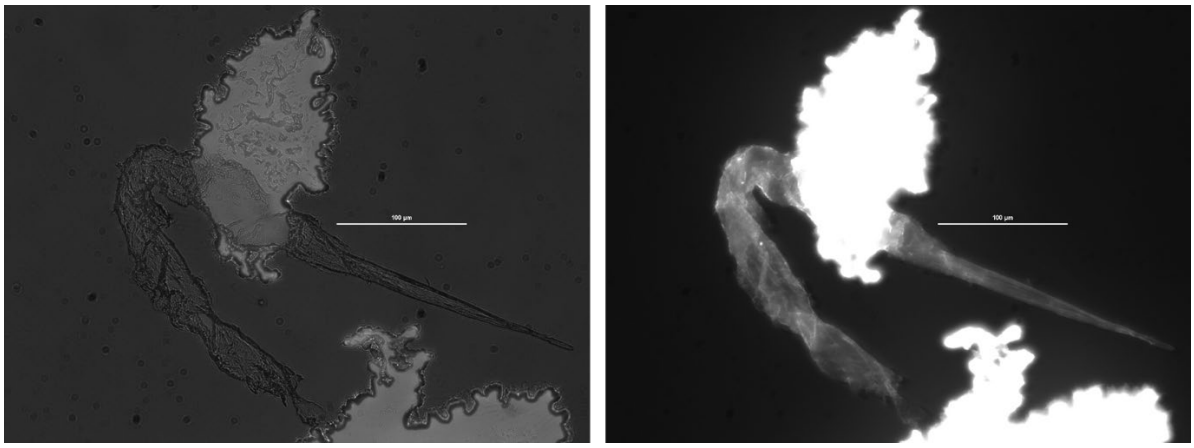

Figure 8-12: Depiction of different fluorescent regimes between sfGFP and ThT. Right: brightfield illumination. Left: fluorescent illumination showing bright illumination of sfGFP dominant structures and less intense illumination of ThT-stained structures. Scale bars 100 um.

8.5 Discussion

These results show that tau the aggregation behavior of these two tau isoforms can be enhanced by treatment in the reciprocal extensor device. While both dGAE and sf-GFP tau isoforms exhibited measurable self-aggregation behavior, both treatment groups aggregated at a greater rate, and both produced visible aggregates that precipitated out of solution. This implies an interplay between the chemical environment and conformation of the proteins coupled with the extensional flow field induced by the reciprocal extensor device on the aggregation behavior of tau. While the exact isoform of the protein studied is important, it is clear from these results that the mechanical environment in which the protein is found plays an important role in its aggregation.

Furthermore, the fluorescence of the ThT dye exhibited by the precipitated particles confirms the presence of amyloid structures within the resultant aggregates. For the first time, to our knowledge, amyloid fibrils have been observed and confirmed using simply extensional fluid flow, without the use of chemical induction. This implies that not only can the flow field enhance tau aggregation, it can also potentially lead to aggregation that is physiologically relevant to injury and diseases such as CTE and Alzheimer's disease.

Finally, the existence of the large complex fibrillary structures observed in both dGAE and sf-GFP tau further illustrates the potential this method has to mimic the aggregation behavior seen in clinically diagnosed brains. Coupled with concentration, extensional flow field intensity, and duration, we were successful in inducing and enhancing tau protein aggregation. Analyzing this behavior further could reveal important information about how tau aggregation is induced or enhanced in-vivo.

8.6 Future paths

These preliminary results show that the reciprocal extensor is capable of producing potentially pathologically significant tau aggregates. It also offers promise that a similar framework presented in Chapter 7 can be achieved for tau protein, thus revealing a method to characterize and predict tau aggregation. To do so, more testing is required to fully characterize the aggregation behavior of different tau isoforms and how they are influenced by flow field intensity and protein concentration. With this new characterization, these results may have significant implications for filling a gap in knowledge of the generation and propagation of tau aggregation.

One peculiar result of this experiment that begs for greater characterization is the fact that these two tau isoforms qualitatively aggregate differently, forming aggregated precipitates that look distinctly different. This indicates that the isoform, whether truncated or phosphorylated, plays an important role in the aggregation behavior of the protein. This much is known already, as past research has shown qualitative differences in the aggregates formed by different tau isoforms[153,157]. However, as discussed in Chapter 7, the relative size of the protein may also play an important role mechanically in its aggregation, as larger molecules are more likely to be stretched by any extensional flow field.

The work presented in this chapter as well as Chapters 6 and 7 suggests that much can be discovered by applying this methodology to full-length non-phosphorylated tau. BSA is not a self-aggregating molecule, yet aggregation was achieved using this methodology. This indicates a potential that the aggregation of full-length tau, which is also known to be not self-aggregating, may also be influenced by subjecting it to a controlled extensional field. In addition to aggregation behavior, this may also reveal information about how full length tau becomes phosphorylated or truncated leading to the aggregations that are observed in diseased brains[159,160].

8.7 Summary

The results presented here preliminarily show that tau aggregation can be successfully enhanced by the application of repeated, high magnitude extensional strains. To our knowledge, this is the first time that tau aggregates of this type and formation have been observed being initiated solely by the application of extensional, mechanical strain. These results show promise for a new avenue of tau aggregation research, investigating the role mechanical strain has on its

initiation and propagation following injury or disease. In addition to providing a path for the study of tau aggregation directly, the results here also show promise that future research into the mechanical contribution to other pathological processes may also yield significant and impactful results. While many questions remain about the exact mechanical characteristics of tau aggregation, these preliminary results show that an entirely novel branch of research can be utilized to more fully characterize tau aggregation and its associated diseases and pathologies.

Chapter 9 : Conclusion

This dissertation aimed to narrow a significant gap in understanding of biological fluid flow processes by applying principles of extensional flow to study the behavior of biological fluids and proteins under physiologically relevant mechanical strains. First, through the development and application of novel rheological methods, we characterized the properties of biological fluids like vitreous humor and cerebrospinal fluid (CSF), revealing that surgical methods and disease states significantly influence and are influenced by their mechanical behaviors.

Then, building upon these insights, we designed and implemented an extensional flow device to induce aggregation in protein solutions. Using this system, we demonstrated that extensional flow can trigger aggregation of bovine serum albumin and, notably, two tau protein variants, dGAE and phosphorylated sf-GFP tau, resulting in structures consistent with pathological aggregates observed in neurodegenerative diseases. This is the first study to have produced these aggregations in BSA while confirming the presence of amyloid formations indicated by ThT fluorescence. Furthermore, this is the first work of its kind to produce tau aggregates using only mechanical fluidic strain. With these results, further in-vitro characterization of physiologically relevant tau aggregation becomes a realistic possibility, potentially further narrowing the gap between mechanical traumatic brain injury, and pathological tau aggregation,

Perhaps most significantly, we proposed a non-dimensional framework for analyzing and predicting protein aggregation under extensional flow. This model lays the groundwork for a more mechanistic and quantitative understanding of aggregation processes, offering potential applications in both diagnostics and therapeutic development. As currently constituted, the calculated Pe_m and f values for tau, in addition to the experimental results collected in Chapter 8,

suggest that it is much more susceptible to aggregation than BSA. With more testing and analysis, this framework could be validated and extended to other aggregating protein species of physiological and pathological interest.

Together, these findings illustrate the powerful role that mechanical forces—particularly extensional flow—can play in biological contexts. They highlight the necessity of integrating mechanical and biochemical paradigms to fully understand the onset and progression of protein aggregation diseases. By leveraging these mechanical, extensional, fluidic tools to explore a fundamentally biological problem, this work opens new pathways for interdisciplinary research and sets the stage for future advances in both neurobiology and biomedical engineering.

REFERENCES

1. Walker, L. C. & LeVine, H. The cerebral proteopathies. *Neurobiol. Aging* **21**, 559–561 (2000).
2. Flavin, W. P. *et al.* Traumatic brain injury and the pathways to cerebral tau accumulation. *Front. Neurol.* **14**, 1239653 (2023).
3. Sexton, C. *et al.* Current directions in tau research: Highlights from Tau 2020. *Alzheimers Dement.* **18**, 988–1007 (2022).
4. Zhang, Y., Wu, K.-M., Yang, L., Dong, Q. & Yu, J.-T. Tauopathies: new perspectives and challenges. *Mol. Neurodegener.* **17**, 28 (2022).
5. Katsumoto, A., Takeuchi, H. & Tanaka, F. Tau Pathology in Chronic Traumatic Encephalopathy and Alzheimer's Disease: Similarities and Differences. *Front. Neurol.* **10**, (2019).
6. Marklund, N. *et al.* Tau aggregation and increased neuroinflammation in athletes after sports-related concussions and in traumatic brain injury patients – A PET/MR study. *NeuroImage Clin.* **30**, 102665 (2021).
7. McKee, A. C., Stein, T. D., Kiernan, P. T. & Alvarez, V. E. The Neuropathology of Chronic Traumatic Encephalopathy. *Brain Pathol.* **25**, 350–364 (2015).
8. McKee, A. C. *et al.* The spectrum of disease in chronic traumatic encephalopathy. *Brain* **136**, 43–64 (2013).
9. Mez, J. *et al.* Clinicopathological Evaluation of Chronic Traumatic Encephalopathy in Players of American Football. *JAMA* **318**, 360–370 (2017).
10. Bieniek, K. F. *et al.* Association between contact sports participation and chronic traumatic encephalopathy: a retrospective cohort study. *Brain Pathol.* **30**, 63–74 (2020).

11. Toma, M., Chan-Akeley, R., Lipari, C. & Kuo, S.-H. Mechanism of Coup and Contrecoup Injuries Induced by a Knock-Out Punch. *Math. Comput. Appl.* **25**, 22 (2020).

12. Lim, S., Haque, Md. M., Kim, D., Kim, D. J. & Kim, Y. K. Cell-based Models To Investigate Tau Aggregation. *Comput. Struct. Biotechnol. J.* **12**, 7–13 (2014).

13. Hong, E., Yeneneh, A. M., Sen, T. K., Ang, H. M. & Kayaalp, A. A comprehensive review on rheological studies of sludge from various sections of municipal wastewater treatment plants for enhancement of process performance. *Adv. Colloid Interface Sci.* **257**, 19–30 (2018).

14. Trumbore, C. N. Chapter Seven - Shear-induced amyloid formation of IDPs in the brain. in *Progress in Molecular Biology and Translational Science* (ed. Uversky, V. N.) vol. 166 225–309 (Academic Press, 2019).

15. Paten, J. A. *et al.* Flow-Induced Crystallization of Collagen: A Potentially Critical Mechanism in Early Tissue Formation. *ACS Nano* **10**, 5027–5040 (2016).

16. Susilo, M. E., Paten, J. A., Sander, E. A., Nguyen, T. D. & Ruberti, J. W. Collagen network strengthening following cyclic tensile loading. *Interface Focus* **6**, 20150088 (2016).

17. Cherry, E. M. & Eaton, J. K. Shear thinning effects on blood flow in straight and curved tubes. *Phys. Fluids* **25**, 073104 (2013).

18. Calabrese, V., Haward, S. J. & Shen, A. Q. Effects of Shearing and Extensional Flows on the Alignment of Colloidal Rods. *Macromolecules* **54**, 4176–4185 (2021).

19. Hosseini, H. *et al.* Probing Flow-Induced Biomolecular Interactions With Micro-Extensional Rheology: Tau Protein Aggregation. *J. Biomech. Eng.* **142**, (2020).

20. Dobson, J. *et al.* Inducing protein aggregation by extensional flow. *Proc. Natl. Acad. Sci.* **114**, 4673–4678 (2017).

21. Willis, L. F. *et al.* The uniqueness of flow in probing the aggregation behavior of clinically relevant antibodies. *Eng. Rep.* **2**, e12147 (2020).

22. Willis, L. F. *et al.* Using extensional flow to reveal diverse aggregation landscapes for three IgG1 molecules. *Biotechnol. Bioeng.* **115**, 1216–1225 (2018).

23. Miller, E., Clasen, C. & Rothstein, J. The effect of step-stretch parameters on Capillary Breakup Extensional Rheology (CaBER) measurements. *Rheol. Acta* **48**, 625–639 (2008).

24. College, O. *English: Illustration from Anatomy & Physiology, Connexions Web Site. Http://Cnx.Org/Content/Col11496/1.6/, Jun 19, 2013.* (2013).

25. Photography, D. F. *Drool*. (2015).

26. Telano, L. N. & Baker, S. Physiology, Cerebral Spinal Fluid. in *StatPearls* (StatPearls Publishing, Treasure Island (FL), 2021).

27. Kelley, D. H. & Thomas, J. H. Cerebrospinal Fluid Flow. *Annu. Rev. Fluid Mech.* **55**, null (2023).

28. Iliff, J. J. *et al.* Cerebral Arterial Pulsation Drives Paravascular CSF–Interstitial Fluid Exchange in the Murine Brain. *J. Neurosci.* **33**, 18190–18199 (2013).

29. Bergsneider, M., Alwan, A. A., Falkson, L. & Rubinstein, E. H. The relationship of pulsatile cerebrospinal fluid flow to cerebral blood flow and intracranial pressure: a new theoretical model. *Acta Neurochir. Suppl.* **71**, 266–268 (1998).

30. OpenStax. *Version 8.25 from the Textbook*. (2016).

31. Sakka, L., Coll, G. & Chazal, J. Anatomy and physiology of cerebrospinal fluid. *Eur. Ann. Otorhinolaryngol. Head Neck Dis.* **128**, 309–316 (2011).

32. Brinker, T., Stopa, E., Morrison, J. & Klinge, P. A new look at cerebrospinal fluid circulation. *Fluids Barriers CNS* **11**, 10 (2014).

33. Bohr, T. *et al.* The glymphatic system: Current understanding and modeling. *iScience* **25**, 104987 (2022).

34. Iliff, J. J. *et al.* A Paravascular Pathway Facilitates CSF Flow Through the Brain Parenchyma and the Clearance of Interstitial Solutes, Including Amyloid β. *Sci. Transl. Med.* **4**, 147ra111 (2012).

35. Iliff, J. J. *et al.* Brain-wide pathway for waste clearance captured by contrast-enhanced MRI. *J. Clin. Invest.* **123**, 1299–1309 (2013).

36. Lohela, T. J., Lilius, T. O. & Nedergaard, M. The glymphatic system: implications for drugs for central nervous system diseases. *Nat. Rev. Drug Discov.* **21**, 763–779 (2022).

37. Limeri, L. Chapter 21: Protein Structure and Function.

38. Granzier, H., Kellermayer, M., Helmes, M. & Trombitás, K. Titin elasticity and mechanism of passive force development in rat cardiac myocytes probed by thin-filament extraction. *Biophys. J.* **73**, 2043–2053 (1997).

39. Xu, B., Li, H. & Zhang, Y. Understanding the viscoelastic behavior of collagen matrices through relaxation time distribution spectrum. *Biomatter* **3**, e24651 (2013).

40. Damry, A. M., Mayer, M. M., Broom, A., Goto, N. K. & Chica, R. A. Origin of conformational dynamics in a globular protein. *Commun. Biol.* **2**, 433 (2019).

41. Dunker, A. K. *et al.* What's in a name? Why these proteins are intrinsically disordered. *Intrinsically Disord. Proteins* **1**, e24157 (2013).

42. Kim, D.-H. & Han, K.-H. Chapter Six - Target-binding behavior of IDPs via pre-structured motifs. in *Progress in Molecular Biology and Translational Science* (ed. Uversky, V. N.) vol. 183 187–247 (Academic Press, 2021).

43. Trumbore, C. N. Shear-Induced Amyloid Formation in the Brain: III. The Roles of Shear Energy and Seeding in a Proposed Shear Model. *J. Alzheimers Dis.* **65**, 47–70 (2018).

44. *Complex Fluids in Biological Systems: Experiment, Theory, and Computation*. (Springer, New York, NY, 2015). doi:10.1007/978-1-4939-2065-5.

45. Ashton, L., Dusting, J., Imomoh, E., Balabani, S. & Blanch, E. W. Susceptibility of Different Proteins to Flow-Induced Conformational Changes Monitored with Raman Spectroscopy. *Biophys. J.* **98**, 707–714 (2010).

46. Ewoldt, R. H., Johnston, M. T. & Caretta, L. M. Experimental Challenges of Shear Rheology: How to Avoid Bad Data. in *Complex Fluids in Biological Systems: Experiment, Theory, and Computation* (ed. Spagnolie, S. E.) 207–241 (Springer, New York, NY, 2015). doi:10.1007/978-1-4939-2065-5_6.

47. Cromwell, M. E. M., Hilario, E. & Jacobson, F. Protein aggregation and bioprocessing. *AAPS J.* **8**, E572–E579 (2006).

48. Trumbore, C. N. Shear-Induced Amyloid Formation in the Brain: I. Potential Vascular and Parenchymal Processes. *J. Alzheimers Dis.* **54**, 457–470 (2016).

49. Hakala, T. A. *et al.* Accelerating Reaction Rates of Biomolecules by Using Shear Stress in Artificial Capillary Systems. *J. Am. Chem. Soc.* **143**, 16401–16410 (2021).

50. Trumbore, C. N. Shear-Induced Amyloid Formation in the Brain: II. An Experimental System for Monitoring Amyloid Shear Processes and Investigating Potential Spinal Tap Problems. *J. Alzheimers Dis.* **59**, 543–557 (2017).

51. Smock, R. G. & Gierasch, L. M. Sending signals dynamically. *Science* **324**, 198–203 (2009).

52. Dunstan, D. E., Hamilton-Brown, P., Asimakis, P., Ducker, W. & Bertolini, J. Shear flow promotes amyloid-β fibrilization. *Protein Eng. Des. Sel.* **22**, 741–746 (2009).

53. Jucker, M. & Walker, L. C. Self-propagation of pathogenic protein aggregates in neurodegenerative diseases. *Nature* **501**, 45–51 (2013).

54. Trumbore, C. N. Shear-Induced Amyloid Aggregation in the Brain: V. Are Alzheimer's and Other Amyloid Diseases Initiated in the Lower Brain and Brainstem by Cerebrospinal Fluid Flow Stresses? *J. Alzheimers Dis.* **79**, 979–1002 (2021).

55. Duerkop, M., Berger, E., Dürauer, A. & Jungbauer, A. Impact of Cavitation, High Shear Stress and Air/Liquid Interfaces on Protein Aggregation. *Biotechnol. J.* **13**, 1800062 (2018).

56. Castellani, R. J. The Significance of Tau Aggregates in the Human Brain. *Brain Sci.* **10**, 972 (2020).

57. Bayer, T. A. Proteinopathies, a core concept for understanding and ultimately treating degenerative disorders? *Eur. Neuropsychopharmacol.* **25**, 713–724 (2015).

58. Billings, J. THE QUEST - leading to the discovery of the Billings Ovulation Method. *Bull. Ovul. Method Res. Ref. Cent. Austrailia* **29**, 18–28 (2002).

59. Reus, R. What is the cervical mucus like during ovulation and on fertile days? *inviTRA* https://www.invitra.com/en/cervical-mucus-as-a-fertility-indicator/ (2022).

60. Panalytical, M. Rheology 101 – Learning the Basics. *AZoM* https://www.azom.com/article.aspx?ArticleID=16985 (2018).

61. Zhao, X. *et al.* Air-Permeable Textile Bioelectronics for Wearable Energy Harvesting and Active Sensing. *Adv. Mater. Technol.* **8**, 2201703 (2023).

62. Zhao, X. *et al.* A self-filtering liquid acoustic sensor for voice recognition. *Nat. Electron.* 1–9 (2024) doi:10.1038/s41928-024-01196-y.

63. Jafari, S., Hollister, J., Kavehpour, P. & Demer, J. L. Shear viscoelastic properties of human orbital fat. *J. Biomech.* **177**, 112416 (2024).

64. Dinic, J. & Sharma, V. Macromolecular relaxation, strain, and extensibility determine elastocapillary thinning and extensional viscosity of polymer solutions. *Proc. Natl. Acad. Sci.* **116**, 8766–8774 (2019).

65. Moitra, P., Gonnermann, H. M., Houghton, B. F. & Tiwary, C. S. Fragmentation and Plinian eruption of crystallizing basaltic magma. *Earth Planet. Sci. Lett.* **500**, 97–104 (2018).

66. Dinic, J., Zhang, Y., Jimenez, L. N. & Sharma, V. Extensional Relaxation Times of Dilute, Aqueous Polymer Solutions. *ACS Macro Lett.* **4**, 804–808 (2015).

67. Dinic, J., Jimenez, L. N. & Sharma, V. Pinch-off dynamics and dripping-onto-substrate (DoS) rheometry of complex fluids. *Lab Chip* **17**, 460–473 (2017).

68. Chan, S. T. *et al.* Torsional fracture of viscoelastic liquid bridges. *Proc. Natl. Acad. Sci.* **118**, e2104790118 (2021).

69. Entov, V. M. & Hinch, E. J. Effect of a spectrum of relaxation times on the capillary thinning of a filament of elastic liquid. *J. Non-Newton. Fluid Mech.* **72**, 31–53 (1997).

70. Cipriani, G., Dolciotti, C., Picchi, L. & Bonuccelli, U. Alzheimer and his disease: a brief history. *Neurol. Sci.* **32**, 275–279 (2011).

71. Baum, J. & Raleigh, D. Protein Aggregation. *Protein Sci.* **27**, 1149–1150 (2018).

72. Astbury, W. T. & Woods, H. J. The Molecular Weights of Proteins. *Nature* **127**, 663–665 (1931).

73. Huggins, M. L. The Structure of Fibrous Proteins. *Chem. Rev.* **32**, 195–218 (1943).

74. Neurath, H. Intramolecular Folding of Polypeptide Chains in Relation to Protein Structure. *J. Phys. Chem.* **44**, 296–305 (1940).

75. Prusiner, S. B. Novel proteinaceous infectious particles cause scrapie. *Science* **216**, 136–144 (1982).

76. Fiala, J. C. Mechanisms of amyloid plaque pathogenesis. *Acta Neuropathol. (Berl.)* **114**, 551–571 (2007).

77. Koundal, S. *et al.* Molecular interaction study of L-Ornithine with bovine serum albumin using spectroscopic and molecular docking methods. *Sci. Rep.* **15**, 11997 (2025).

78. Borzova, V. A. *et al.* Kinetics of Thermal Denaturation and Aggregation of Bovine Serum Albumin. *PLoS ONE* **11**, e0153495 (2016).

79. Majorek, K. A. *et al.* Structural and immunologic characterization of bovine, horse, and rabbit serum albumins. *Mol. Immunol.* **52**, 174–182 (2012).

80. Zheng, H., Sun, H., Cai, Q. & Tai, H.-C. The Enigma of Tau Protein Aggregation: Mechanistic Insights and Future Challenges. *Int. J. Mol. Sci.* **25**, 4969 (2024).

81. Billingsley, M. L. & Kincaid, R. L. Regulated phosphorylation and dephosphorylation of tau protein: effects on microtubule interaction, intracellular trafficking and neurodegeneration. *Biochem. J.* **323**, 577–591 (1997).

82. Sharma, L. G. & Pandey, L. M. Thermomechanical process induces unfolding and fibrillation of bovine serum albumin. *Food Hydrocoll.* **112**, 106294 (2021).

83. Kaltbeitzel, J. & Wich, P. R. Protein-basierte Nanopartikel: Von Wirkstofftransport zu Bildgebung, Nanokatalyse und Proteintherapie. *Angew. Chem.* **135**, e202216097 (2023).

84. Chu, B. Laser Light Scattering. *Annu. Rev. Phys. Chem.* **21**, 145–174 (1970).

85. Goodman, J. W. Some fundamental properties of speckle*. *JOSA* **66**, 1145–1150 (1976).

86. Jones, M. *English: An Example of Dynamic Light Scattering.Čeština: Princip DLS.* (2010).

87. Auld, D. S., Inglese, J. & Dahlin, J. L. Assay Interference by Aggregation. in *Assay Guidance Manual* (eds. Markossian, S. et al.) (Eli Lilly & Company and the National Center for Advancing Translational Sciences, Bethesda (MD), 2004).

88. Kashkanova, A. D., Blessing, M., Gemeinhardt, A., Soulat, D. & Sandoghdar, V. Precision size and refractive index analysis of weakly scattering nanoparticles in polydispersions. *Nat. Methods* **19**, 586–593 (2022).

89. Panalytical, M. Using Nanoparticle Tracking Analysis (NTA) to Assess Nanoparticle Toxicity in Waste Water. *AZoNano* https://www.azonano.com/article.aspx?ArticleID=4067 (2015).

90. Filipe, V., Hawe, A. & Jiskoot, W. Critical Evaluation of Nanoparticle Tracking Analysis (NTA) by NanoSight for the Measurement of Nanoparticles and Protein Aggregates. *Pharm. Res.* **27**, 796–810 (2010).

91. Sunde, M. *et al.* Common core structure of amyloid fibrils by synchrotron X-ray diffraction1. *J. Mol. Biol.* **273**, 729–739 (1997).

92. Chiti, F. & Dobson, C. M. Protein Misfolding, Amyloid Formation, and Human Disease: A Summary of Progress Over the Last Decade. *Annu. Rev. Biochem.* **86**, 27–68 (2017).

93. Davidson, D. S., Brown, A. M. & Lemkul, J. A. Insights into Stabilizing Forces in Amyloid Fibrils of Differing Sizes from Polarizable Molecular Dynamics Simulations. *J. Mol. Biol.* **430**, 3819–3834 (2018).

94. Xue, C., Lin, T. Y., Chang, D. & Guo, Z. Thioflavin T as an amyloid dye: fibril quantification, optimal concentration and effect on aggregation. *R. Soc. Open Sci.* **4**, 160696 (2017).

95. Gade Malmos, K. *et al.* ThT 101: a primer on the use of thioflavin T to investigate amyloid formation. *Amyloid* **24**, 1–16 (2017).

96. Lambert, T. ECFP at FPbase. *FPbase* https://www.fpbase.org/protein/ecfp/.

97. Vitreous humor: Location, function, structure, and more. https://www.medicalnewstoday.com/articles/vitreous-humor (2022).

98. Bishop, P. N. Structural macromolecules and supramolecular organisation of the vitreous gel. *Prog. Retin. Eye Res.* **19**, 323–344 (2000).

99. Sebag, J. & Balazs, E. A. Morphology and ultrastructure of human vitreous fibers. *Invest. Ophthalmol. Vis. Sci.* **30**, 1867–1871 (1989).

100. Foulds, W. S. Is your vitreous really necessary? *Eye* **1**, 641–664 (1987).

101. Rossi, T. *et al.* FLUID DYNAMICS OF VITRECTOMY PROBES. *RETINA* **34**, 558–567 (2014).

102. Abulon, D. J. K. Vitreous flow rates through dual pneumatic cutters: effects of duty cycle and cut rate. *Clin. Ophthalmol. Auckl. NZ* **9**, 253–261 (2015).

103. Leitgeb, N., Schuy, S. & Zirm, M. Ultrasonic vitrectomy — an alternative technique to presently used mechanical procedures. *Albrecht Von Graefes Arch. Für Klin. Exp. Ophthalmol.* **209**, 263–268 (1979).

104. Stanga, P. E., Pastor-Idoate, S., Zambrano, I., Carlin, P. & McLeod, D. Performance analysis of a new hypersonic vitrector system. *PloS One* **12**, e0178462 (2017).

105. Ch'ng, S. W. *et al.* Live porcine thirty days delayed recovery surgery: Qualitative findings with the hypersonic vitrectomy. *PloS One* **13**, e0197038 (2018).

106. Sharif-Kashani, P., Hubschman, J.-P., Sassoon, D. & Kavehpour, H. P. Rheology of the vitreous gel: effects of macromolecule organization on the viscoelastic properties. *J. Biomech.* **44**, 419–423 (2011).

107. Stocchino, A. *et al.* Fluid Dynamic Assessment of Hypersonic and Guillotine Vitrectomy Probes in Viscoelastic Vitreous Substitutes. *Transl. Vis. Sci. Technol.* **9**, 9 (2020).

108. Lee, B., Litt, M. & Buchsbaum, G. Rheology of the vitreous body. Part I: Viscoelasticity of human vitreous. *Biorheology* **29**, 521–533 (1992).

109. Lee, B., Litt, M. & Buchsbaum, G. Rheology of the vitreous body: Part 2. Viscoelasticity of bovine and porcine vitreous. *Biorheology* **31**, 327–338 (1994).

110. Lee, B., Litt, M. & Buchsbaum, G. Rheology of the vitreous body: part 3. Concentration of electrolytes, collagen and hyaluronic acid. *Biorheology* **31**, 339–351 (1994).

111. McKinley, G. H. & Sridhar, T. Filament-Stretching Rheometry of Complex Fluids. *Annu. Rev. Fluid Mech.* **34**, 375–415 (2002).

112. Haward, S. J., Odell, J. A., Berry, M. & Hall, T. Extensional rheology of human saliva. *Rheol. Acta* **50**, 869–879 (2011).

113. Rubin, B. K. Mucus structure and properties in cystic fibrosis. *Paediatr. Respir. Rev.* **8**, 4–7 (2007).

114. Stokes, J. R. & Davies, G. A. Viscoelasticity of human whole saliva collected after acid and mechanical stimulation. *Biorheology* **44**, 141–160 (2007).

115. Gupta, S., Wang, W. S. & Vanapalli, S. A. Microfluidic viscometers for shear rheology of complex fluids and biofluids. *Biomicrofluidics* **10**, 043402 (2016).

116. McKinley, G. H. Visco-Elasto-Capillary Thinning and Break-Up of Complex Fluids. (2005).

117. Anna, S. L. & McKinley, G. H. Elasto-capillary thinning and breakup of model elastic liquids. *J. Rheol.* **45**, 115–138 (2001).

118. Pastor-Idoate, S. *et al.* Ultrastructural and histopathologic findings after pars plana vitrectomy with a new hypersonic vitrector system. Qualitative preliminary assessment. *PloS One* **12**, e0173883 (2017).

119. Malinowski, S. M. The Vitreous Trap: A Simple, Surgeon-Controlled Technique for Obtaining Undiluted Vitreous and Subretinal Specimens During Pars Plana Vitrectomy. *RETINA* **30**, 828–829 (2010).

120. Hosseini, H. *et al.* Probing Flow-Induced Biomolecular Interactions With Micro-Extensional Rheology: Tau Protein Aggregation. *J. Biomech. Eng.-Trans. Asme* **142**, 034501 (2020).

121. Clasen, C. *et al.* How dilute are dilute solutions in extensional flows? *J. Rheol.* **50**, 849–881 (2006).

122. Clasen, C., Eggers, J., Fontelos, M. A., Li, J. & McKINLEY, G. H. The beads-on-string structure of viscoelastic threads. *J. Fluid Mech.* **556**, 283–308 (2006).

123. Kaur, J. *et al.* Waste Clearance in the Brain. *Front. Neuroanat.* **15**, (2021).

124. Bloomfield, I. G., Johnston, I. H. & Bilston, L. E. Effects of Proteins, Blood Cells and Glucose on the Viscosity of Cerebrospinal Fluid. *Pediatr. Neurosurg.* **28**, 246–251 (1998).

125. Spector, R., Robert Snodgrass, S. & Johanson, C. E. A balanced view of the cerebrospinal fluid composition and functions: Focus on adult humans. *Exp. Neurol.* **273**, 57–68 (2015).

126. Wang, C. Correlation of the Friction Factor for Turbulent Pipe Flow of Dilute Polymer Solutions. *Ind. Eng. Chem. Fundam.* **11**, 546–551 (1972).

127. Seehusen, D. A., Reeves, M. M. & Fomin, D. A. Cerebrospinal Fluid Analysis. *Am. Fam. Physician* **68**, 1103–1109 (2003).

128. BRYDON, H. L., HAYWARD, R., HARKNESS, W. & BAYSTON, R. Does the cerebrospinal fluid protein concentration increase the risk of shunt complications? *Br. J. Neurosurg.* **10**, 267–274 (1996).

129. Eide, P. K., Valnes, L. M., Lindstrøm, E. K., Mardal, K.-A. & Ringstad, G. Direction and magnitude of cerebrospinal fluid flow vary substantially across central nervous system diseases. *Fluids Barriers CNS* **18**, 16 (2021).

130. Nader, E. *et al.* Blood Rheology: Key Parameters, Impact on Blood Flow, Role in Sickle Cell Disease and Effects of Exercise. *Front. Physiol.* **10**, (2019).

131. Kadowaki, C., Hara, M., Numoto, M., Takeuchi, K. & Saito, I. CSF shunt physics: factors influencing inshunt CSF flow. *Childs Nerv. Syst.* **11**, 203–206 (1995).

132. Siyahhan, B. *et al.* Flow induced by ependymal cilia dominates near-wall cerebrospinal fluid dynamics in the lateral ventricles. *J. R. Soc. Interface* **11**, 20131189 (2014).

133. Rasmussen, M. K., Mestre, H. & Nedergaard, M. Fluid transport in the brain. *Physiol. Rev.* **102**, 1025–1151 (2022).

134. UK, C. R. *Diagram Showing a Brain Shunt.* (2014).

135. Wilhelmy, F. *et al.* Cerebrospinal Fluid Protein Concentrations in Hydrocephalus. *Children* **10**, 644 (2023).

136. Thomas, J. H. Fluid dynamics of cerebrospinal fluid flow in perivascular spaces. *J. R. Soc. Interface* **16**, 20190572 (2019).

137. Mestre, H. *et al.* Flow of cerebrospinal fluid is driven by arterial pulsations and is reduced in hypertension. *Nat. Commun.* **9**, 4878 (2018).

138. Krishnamurthy, S. & Li, J. New concepts in the pathogenesis of hydrocephalus. *Transl. Pediatr.* **3**, 185–194 (2014).

139. Atchley, T. J., Vukic, B., Vukic, M. & Walters, B. C. Review of Cerebrospinal Fluid Physiology and Dynamics: A Call for Medical Education Reform. *Neurosurgery* **91**, 1 (2022).

140. Hollister, J. C. P. *et al.* Ultrasonic Vitrectomy Performance Assessment Using Micro-Extensional Rheology. *Transl. Vis. Sci. Technol.* **12**, 24 (2023).

141. Holm, N. K. *et al.* Aggregation and fibrillation of bovine serum albumin. *Biochim. Biophys. Acta BBA - Proteins Proteomics* **1774**, 1128–1138 (2007).

142. Omalu, B. I., Bailes, J., Hammers, J. L. & Fitzsimmons, R. P. Chronic Traumatic Encephalopathy, Suicides and Parasuicides in Professional American Athletes: The Role of the Forensic Pathologist. *Am. J. Forensic Med. Pathol.* **31**, 130 (2010).

143. Omalu, B. *et al.* Emerging Histomorphologic Phenotypes of Chronic Traumatic Encephalopathy in American Athletes. *Neurosurgery* **69**, 173 (2011).

144. Weids, A. J., Ibstedt, S., Tamás, M. J. & Grant, C. M. Distinct stress conditions result in aggregation of proteins with similar properties. *Sci. Rep.* **6**, 24554 (2016).

145. Goedert, M., Spillantini, M. G., Jakes, R., Rutherford, D. & Crowther, R. A. Multiple isoforms of human microtubule-associated protein tau: sequences and localization in neurofibrillary tangles of Alzheimer's disease. *Neuron* **3**, 519–526 (1989).

146. Luo, Y. *et al.* Molecular insights into the reversible formation of tau protein fibrils. *Chem. Commun.* **49**, 3582–3584 (2013).

147. Al-Hilaly, Y. K. *et al.* Tau (297-391) forms filaments that structurally mimic the core of paired helical filaments in Alzheimer's disease brain. *FEBS Lett.* **594**, 944–950 (2020).

148. Al-Hilaly, Y. K. *et al.* Alzheimer's Disease-like Paired Helical Filament Assembly from Truncated Tau Protein Is Independent of Disulfide Crosslinking. *J. Mol. Biol.* **429**, 3650–3665 (2017).

149. Alali, S. *et al.* Cannabidiol Inhibits Tau Aggregation In Vitro. *Cells* **10**, 3521 (2021).

150. Carlomagno, Y. *et al.* The AD tau core spontaneously self-assembles and recruits full-length tau to filaments. *Cell Rep.* **34**, 108843 (2021).

151. Chakraborty, P. *et al.* Co-factor-free aggregation of tau into seeding-competent RNA-sequestering amyloid fibrils. *Nat. Commun.* **12**, 4231 (2021).

152. Li, W. & Lee, V. M.-Y. Characterization of Two VQIXXK Motifs for Tau Fibrillization in Vitro. *Biochemistry* **45**, 15692–15701 (2006).

153. Lövestam, S. *et al.* Assembly of recombinant tau into filaments identical to those of Alzheimer's disease and chronic traumatic encephalopathy. *eLife* **11**, e76494 (2022).

154. Nam, W.-H. & Choi, Y. P. In vitro generation of tau aggregates conformationally distinct from parent tau seeds of Alzheimer's brain. *Prion* **13**, 1–12 (2018).

155. Zhang, W. *et al.* Heparin-induced tau filaments are polymorphic and differ from those in Alzheimer's and Pick's diseases. *eLife* **8**, e43584 (2019).

156. Trumbore, C. N., Paik, J., Fay, D. & Vachet, R. W. Preliminary Capillary Flow Experiments with Amyloid-β, Possible Needle and Capillary Aβ Adsorption, and a Proposal for Drug Evaluation Under Shear Conditions. *J. Alzheimers Dis.* **72**, 751–760 (2019).

157. Lövestam, S. *et al.* Twelve phosphomimetic mutations induce the assembly of recombinant full-length human tau into paired helical filaments. 2024.10.23.619846 Preprint at https://doi.org/10.1101/2024.10.23.619846 (2024).

158. Ori-McKenney, K. M. & McKenney, R. J. Tau oligomerization on microtubules in health and disease. *Cytoskelet. Hoboken NJ* **81**, 35–40 (2024).

159. Chu, D. *et al.* Tau truncation in the pathogenesis of Alzheimer's disease: a narrative review. *Neural Regen. Res.* **19**, 1221 (2024).

160. Fan, X., Okada, K., Lin, H., Ori-McKenney, K. M. & McKenney, R. J. A pathological phosphorylation pattern enhances tau cooperativity on microtubules and facilitates tau filament assembly. 2025.01.29.635117 Preprint at https://doi.org/10.1101/2025.01.29.635117 (2025).